AMBIPOLAR DIFFUSION IN 3D

SIMULATING CRITICAL HYDROMAGNETIC PROCESSES IN STAR FORMATION: AMBIPOLAR DIFFUSION IN 3D

By

DENNIS F. DUFFIN, B.Sc.Hons.

A Thesis
Submitted to the School of Graduate Studies
for the Degree
Master of Science

McMaster University

MASTER OF SCIENCE (2007)
(Astronomy)

McMaster University
Hamilton, Ontario

TITLE: Simulating critical hydromagnetic processes in star formation: ambipolar diffusion in 3D

AUTHOR: Dennis Duffin, B.Sc.Hons. (Universty of Toronto)

SUPERVISOR: Dr. Ralph E. Pudritz

NUMBER OF PAGES: xiii, 134

Abstract

One of the most difficult and interesting aspects of the physics of collapse and outflow formation, as well as the evolution of the protostellar disk, is the role of hydromagnetic forces. However, magnetic fields are only coupled to the charged species present in poorly ionized molecular clouds. Ambipolar diffusion—the process by which magnetic fields "slip" in poorly ionized gas—strongly affects the initial cloud as well as the final observable structure through collisional heating. Also, as the gas becomes opaque to cosmic rays, the ionized structure of the accreting gas may become more complex, leading to a neutral 'dead zone' in a layered accretion disk (vital in determining planet masses in planet formation theories (Matsumura & Pudritz, 2005)). We omit possible effects of ionizing radiation in these early stages of formation.

In this thesis, we perform fully 3D simulations (using the FLASH AMR code) and have implemented ambipolar diffusion in the MHD module of the code in addition to a broad treatment of cooling (Banerjee et al., 2006). This has allowed us to track the ionized gas and magnetic fields properly from the beginning of collapse down to the onset of outflows. We find that high accretion rates persist on the order of 10^{-3} $M_{\odot}$ yr^{-1} (where the core mass has reached about 0.1 $M_{\odot}$) due to efficient extraction of angular momentum through magnetic processes. Magnetic braking is reduced by about 3/4 in the initial collapse relative to an ideal collapse of same initial conditions. This, with a reduction in magnetic pressure in the disk, leads to

an increased rate of fragmentation. One of the major new results of this work is the discovery that outflows from disks still occur even in the presence of ambipolar diffusion. Surprisingly, they are initiated even earlier than outflows from idealized, completely ionized disks. They are generated by a magnetic tower mechanism at central densities of 10^{12} cm^{-3}, as effective ram pressure on the wound up toroidal field is reduced, allowing it to push away from the disk earlier.

We have also shown that the formation of a dead zone in these early stages is dependent on shielding of cosmic rays, in the absence of which a decoupled zone in the disk midplane forms. This region, where the accreting gas is effectively decoupled from the magnetic field, extends 10 AU in radius and (2-3) AU in height from the midplane. The global magnetic field threading such a complex accretion disk shows a dragged out structure, as coupled surface layers of the disk pull in the field. The disk is puffy due to drift heating and the initial stages of the outflow pushing out into the ambient medium. However, overall magnetic field build-up is still efficient, as values of the magnetic field in the disk are only reduced by half.

To Scruffy,

Chasing the Wind

and

The Music

Acknowledgements

This work is due in large part to the expert supervision of Ralph Pudritz, who's courage through a difficult time I admire. His enthusiasm for ideas in all disciplines has encouraged me to see our work in a broader scope, and inspired me to use what I've learned here outside of the physics discipline. I have understood that despite endless lines of code and numerous equations and simulations, it is the physics that is important and which gives us insight into the reality that we wish to understand.

Special thanks to Robi Banerjee who helped me through the endless coding problems, surviving all of my questions while continuing to encourage me. Thanks to fellow graduate students, in particular Colin McNally, who helped me as a green programmer two years ago. The community of McMaster has been the perfect atmosphere in which to learn and do research, and I have appreciated the support of everyone through stressful moments.

My family have given me unquestionable support through the toughest times and through all my endeavors. I would not have gotten far without them.

Finally, the strength and confidence I needed to complete this project came from love in its purest form, without the need for boundaries, and from the insight and experience of the many lives that lie in *mon amour.*

Contents

List of Tables

List of Figures

Preface

Chapter 4 of this thesis was prepared as a paper, and will be submitted for publication in the Astrophysical Journal. Contained in this chapter is a short introduction summarizing the material covered in depth in the earlier chapters. The computational method and numerical tests behind our work in Chapter 4 have yielded interesting new results which we plan to publish as a companion paper to Chapter 4 in the Monthly Notices of the Royal Astronomical Society (MNRAS). The latter is contained in chapter 3 as a numerical review of our methods. These chapters are intended to serve as a complete and detailed explanation of the theoretical and numerical aspects of this research.

Chapter 1

Introduction

My first big astrophysics conference was in French Alps, in a small tourist town called Chamonix. The subject was *Structure Formation in the Universe*, and it gathered the premier theorists, numericists and observers in the fields of galaxy, star and planet formation as well as in cosmology. What amazed me as a young graduate student in this gathering of giants (besides the view!) was the immense interest in this little known physical process called ambipolar diffusion. It seemed to find its way into many talks, particularly in what one would consider to further develop their work. I was presenting a poster on the very subject (on applications to star formation) and I was put on the spot, often without having to badger anyone.

In astrophysics we use all the tools available to us. Complex theories abound, from quantum mechanical effects opening observational windows (e.g. 21 cm radiation) to relativistic monsters offering theoretical mysteries (e.g. black holes). In a sense ambipolar diffusion is simple as it relates to simple physics we all know and love: Ohm's Law. When we have a gas that is as partially ionized such as the interstellar medium (ISM)—where ions have number densities around $n_{\rm ions} \approx 10^{-7}\ n_{\rm H}$—electric currents must pass through a heavy resistor (the neutral gas) to get anywhere. In turn, the ions and electrons will impart, through collisions (which can be modeled as a frictional force), magnetic effects such as the Lorentz force upon the neutral species. A unique quality of this ambipolar circuit is that collisional frequencies between ion and neutral particles are fairly small. Neutral matter can diffuse through field lines, or vice versa, but at the cost of frictional heating. Ion-neutral drifting in this sense is named ambipolar diffusion by astronomers. It was first used to describe the effective diffusion of magnetic flux in magnetically supported clouds, leading to their eventual collapse (Mestel & Spitzer, 1956; Spitzer, 1978). These clouds were theorized to exist at the time, though ideas of turbulence, combined with current observations, has transformed our ideas of star formation (§2.3.1).

To study the gas in astrophysical problems we start from very simple approximations—a hydrodynamic (HD) gas that moves in response to gravity—and evolve to a more complex behaviour involving magnetic fields, which we call magnetohydrodynamics (MHD). Theoretically, MHD equations are difficult equations to get anything out of (as they are highly non-linear), especially when we're talking about the complex movements of gas in a star-forming environment. In such a case, it is common to use numerical techniques to predict the patterns we may observe in nature, or more importantly, to understand the important physical processes at work. Often, we begin with a cloud of particles which is perfectly coupled to the gas: a material with an infinite conductivity. This allows us to probe the effects of magnetic fields and understand interesting areas of research from a "first-approximation" standpoint. In this fashion the magnetorotational instability (MRI) in accretion disks has been discovered (Balbus & Hawley, 1991), the principal source of protoplanetary disk viscosity. This occurs naturally in a differentially rotating, weakly magnetic flow (given certain restrictions). Also, we have found that collapsing clouds can lose large amounts of angular momentum through magnetic effects, and even produce large outflows and jets before the central protostar has turned on (Banerjee & Pudritz, 2006). Magnetic effects are particularly interesting in star-forming environments.

Once we understand the possible physical phenomena of magnetic fields, it is necessary to see if they persist under non-ideal MHD conditions. There are many non-ideal aspects of the physics in addition to ambipolar diffusion, such as Ohmic dissipation and Hall electromotive forces, each with its own role in different stages of a star's evolution.

Ohmic resistivity and Hall electromotive forces occur in non-ideal plasmas when collisional times are short and ions and neutrals are well coupled (this occurs for large densities such as $n > 10^{10}$ cm^{-3} (Nakano et al., 2002; Tassis & Mouschovias, 2007b). This corresponds approximately with the transition from the optically thin regime to the optically thick regime (Bate et al., 1995)). The neutrals act like a stiff resistor which will slow down the electrical currents of ions while dissipating the field. When the ions (positive charges) and the electrons (negative charges) decouple, the Hall terms become important. The corresponding stage in the star's evolution is late Class 0 or Class I, where a Keplerian accretion disk has formed around an early protostar.

The first stages of a star's evolution involve the turbulent formation of an initial molecular core or filament of mass on the order of a few to several hundred $M_{\odot}$. This process occurs on short timescales of 2 Myr, in agreement with observations of star formation timescales (Allen et al., 2007; Mac Low & Klessen, 2004; Elmegreen & Scalo, 2004). Sharply discontinuous shocked structures in a turbulent environment may be smoothed out through ambipolar diffusion if the conditions are right (these are called C-shocks (Wardle, 1991b, §2.3.3, §3.3.2)). Although many cores will proceed to collapse on short timescales of 10^4 yr, any magnetically stable clumps that form will loose their support through ambipolar diffusion (Krasnopolsky & Gammie, 2005), accelerated by the turbulence (Zweibel, 2002). Subsequent features of collapse are a rotationally and magnetically supported non-Keplerian pseudo-disk, along with disk instabilities, magnetically driven bipolar outflows and highly collimated jets. This stage is the pre-Class 0 stage in a star's evolution, just before protostar has formed. During this stage densities range from $n \approx (10^2 - 10^4)$ cm^{-3} to much higher densities of $n \approx (10^{12} - 10^{18})$ cm^{-3}. There are many problems arising from this latter stage which are still not fully understood.

Our goal in this thesis is to study the initial collapse of a star forming molecular cloud using very precise microphysics relevant to the problem, particularly ambipolar diffusion. We establish the theoretical background in Chapter 2. Previously established physics are discussed in §3.2.2 and include realistic cooling, rotation and ideal gravito-magnetohydrodynamics in a 3D environment. For this study our initial conditions are that of a Bonnor-Ebert Sphere (§3.2.1). The principal questions we seek to answer are:

- Do high accretion rates seen in previous collapse simulations persist if we introduce a finite conductivity (§2.3.1)?
- How are important, magnetically driven phenomena affected by this decreased coupling of the gas to the field? This touches on a number of important problems:
  - **Magnetic Braking:** Ideal magnetic braking has a very strong effect in slowing the rotation of molecular clouds (§2.3.2). It is also responsible for aligning the field with the rotation axis (Machida et al., 2006). To what

degree is braking reduced by ambipolar diffusion in the collapse?

  - **Angular Momentum Transport:** In the collapsing, rotating cloud a large toroidal field is quickly established and redistributes angular momentum (Banerjee & Pudritz, 2006). This is responsible for aiding high accretion. If this field is reduced through diffusion, to what degree is the angular momentum distribution affected?

  - **Large Fossil Fields:** We have observed large fossil fields of about 3 G through meteoritic samples of our solar system at 1 AU (Levy & Sonett, 1978). Ideal collapses show this build-up is possible (Banerjee & Pudritz, 2006). Can these large fields still be built up in face of ambipolar diffusion in the disk?

  - **Outflows:** We know that large scale outflows from the disk form early on in an ideal collapse, before the protostar has even formed (Banerjee & Pudritz, 2007; Machida et al., 2007). We observe a large magnetic tower (Lynden-Bell, 2003) pushing material away from the disk in magnetized bubbles. Will these outflows still form early on in a non-ideal collapse?

- Fragmentation is known to be significantly affected by magnetic fields. There are strong effects seen through the addition of ambipolar diffusion (Hosking & Whitworth, 2004a; Price & Bate, 2007) though the principal cause is in contest; is it because magnetic braking is significantly decreased, or is it due to the lack of magnetic pressure in the disk?

- Finally, does a sort of proto-dead zone form early in the collapse where MRI turbulence is severely damped (§2.3.4)? Or perhaps more of a *decoupled zone* where magnetic fields are only dragged in through actively coupled layers?

This thesis addresses these questions and describes our progress and results in the following chapters. In §2.3 we review current and relevant work involving ambipolar diffusion. We introduce the theory along with customized caveats important to our particular analysis and implementation in §2.1 and §2.2. In Chapter 3 we will outline our numerical methods. This chapter features new and interesting numerical aspects and results pertaining to ambipolar diffusion which we will later submit to the Monthly Notices of the Royal Astronomical Society (MNRAS) for publication. A paper (to be submitted in the Astrophysical Journal) is presented in Chapter 4, and features our new results. We ignore chemical and other non-ideal MHD effects which could be important. This is discussed in Chapter 5 along with future work that can be undertaken now that these first steps have been established.

Chapter 2

Non-Ideal Magnetohydrodynamic (MHD) Theory in Star Formation

In this chapter, we review the important theoretical aspects in the realistic collapse of a molecular cloud. We outline the important physical equations relevant to a very general treatment of ambipolar diffusion in §2.1. We briefly discuss the consequences of chemistry in §2.1.1. Approximations that arise from this are developed in §2.2, focusing on the single-fluid approximation in §2.2.1. We discuss the role of ambipolar diffusion as a true diffusion, and solve the corresponding timestep in §2.2.2. Section 2.3 reviews the current state of simulations—emphasizing modern developments—for a variety of physical situations applicable to a collapsing molecular cloud. This includes collapse (§2.3.1), fragmentation and magnetic braking (§2.3.2), C-shocks (§2.3.3) and finally the development of early dead zones during pre-Class 0 collapse (§2.3.4).

2.1 Theory of Ambipolar Diffusion

Consider a gas composed of both ions (subscript i) and neutrals (subscript n). The magnetohydrodynamic (MHD) equations for this two-component system, in which only the ions couple to the field, are[1],

$$\frac{\partial \rho_n}{\partial t} + \nabla \cdot (\rho_n \boldsymbol{u}_n) = 0 \tag{2.1}$$

$$\frac{\partial \rho_i}{\partial t} + \nabla \cdot (\rho_i \boldsymbol{u}_i) = 0 \tag{2.2}$$

$$\frac{\partial (\rho_n \boldsymbol{u}_n)}{\partial t} + \nabla \cdot (\rho_n \boldsymbol{u}_n \boldsymbol{u}_n + P_n) = -\rho_n \boldsymbol{g} - \boldsymbol{f}_f \tag{2.3}$$

$$\frac{\partial (\rho_i \boldsymbol{u}_i)}{\partial t} + \nabla \cdot \left(\rho_i \boldsymbol{u}_i \boldsymbol{u}_i + P_i + \frac{B^2}{2\mu_0} - \frac{1}{\mu_0}\boldsymbol{B}\boldsymbol{B}\right) = -\rho_i \boldsymbol{g} + \boldsymbol{f}_f - \frac{1}{\mu_0}\boldsymbol{B}(\nabla \cdot \boldsymbol{B}), \tag{2.4}$$

where ρ represents density, $\boldsymbol{u}$ is a velocity, P is a pressure, $\boldsymbol{B}$ is the magnetic field, $\boldsymbol{g}$ is the gravitational acceleration and $\boldsymbol{f}_f$ is the frictional force density from ion-neutral collisions (Spitzer, 1978),

$$\boldsymbol{f}_f \equiv \gamma_{\mathrm{AD}} \rho_i \rho_n (\boldsymbol{u}_n - \boldsymbol{u}_i) = -\frac{1}{\mu_0 \beta_{\mathrm{AD}}} \boldsymbol{u}_d, \tag{2.5}$$

where $\beta_{\mathrm{AD}} = \frac{1.4}{\mu_0 \gamma_{\mathrm{AD}} \rho_i \rho_n}$ and the drift velocity $\boldsymbol{u}_d$ is defined as,

$$\boldsymbol{u}_d \equiv \boldsymbol{u}_i - \boldsymbol{u}_n. \tag{2.6}$$

The constant $\gamma_{\mathrm{AD}} = \frac{<\sigma\omega>_{ni}}{m_i + m_n} = 3.28 \times 10^{13}\ \mathrm{g}^{-1}\ \mathrm{cm}^3\ \mathrm{s}^{-1}$ represents the coupling of the neutrals and ions. Ions are considered to be typically HCO^+ or Na^+ which have similar masses (about 29.0 a.m.u.) and collision rates with H_2 ($< \sigma\nu >_{\mathrm{ni}} = 1.7 \times 10^{-9}\ \mathrm{cm}^{-3}\ \mathrm{s}^{-1}$ (McDaniel & Mason, 1973)). The value of 1.4 in β_{AD} arises from the fact that we

[1]Please note that we have developed these equations such that $\nabla \cdot \boldsymbol{B} \neq 0$ due to the fact that our numerical scheme does not conserve this strict physical law, although keeping values below truncation-level error. Adding these terms will ensure numerical stability for the code. More discussion can be found in §3.1.1.

have about 10% He per H atom in our gas (Hosking & Whitworth, 2004b; Fiedler & Mouschovias, 1993). Helium is heavier than H_2, and thus changes the collisional dynamics of the neutral gas.

Equations (2.1) and (2.2) are the continuity equations of the neutrals and ions respectively, expressing conservation of mass. Equations (2.3) and (2.4) are expressions of conservation of momentum. Note that while the ions undergo direct magnetohydrodynamic (MHD) forces, the neutrals do so only by collisions with the ions through the friction term in the hydrodynamic (HD) momentum equation (2.3).

The induction equation—coupled to the ions—is,

$$\frac{\partial \boldsymbol{B}}{\partial t} = -\boldsymbol{\nabla} \cdot (\boldsymbol{u}_i \boldsymbol{B} - \boldsymbol{B} \boldsymbol{u}_i) - (\boldsymbol{\nabla} \cdot \boldsymbol{B})\, \boldsymbol{u}_i. \tag{2.7}$$

This defines the evolution of the magnetic field.

Expressing conservation of energy we find the rest of our initial equations,

$$\frac{\partial E_n}{\partial t} + \boldsymbol{\nabla} \cdot [\boldsymbol{u}_n (E_n + P_n)] = -\boldsymbol{u}_n \cdot \boldsymbol{f}_f + \rho_n \boldsymbol{g} \cdot \boldsymbol{u}_n \tag{2.8}$$

$$\begin{aligned}\frac{\partial E_i}{\partial t} + \boldsymbol{\nabla} \cdot \left[\boldsymbol{u}_i \left(E_i + P_i + \frac{B^2}{2\mu_0}\right) + \frac{1}{\mu_0} (\boldsymbol{u}_i \cdot \boldsymbol{B})\, \boldsymbol{B}\right] =& \boldsymbol{u}_i \cdot \boldsymbol{f}_f + \rho_i \boldsymbol{g} \cdot \boldsymbol{u}_i \\ &- \frac{1}{\mu_0} (\boldsymbol{u}_i \cdot \boldsymbol{B})\, (\boldsymbol{\nabla} \cdot \boldsymbol{B}),\end{aligned} \tag{2.9}$$

where we see the neutrals are again HD and the ions are MHD. The energy densities are respectively defined as:

$$E_n = \frac{1}{2} \rho_n u_n^2 + \frac{1}{\gamma - 1} P_n \tag{2.10}$$

$$E_i = \frac{1}{2} \rho_i u_i^2 + \frac{1}{\gamma - 1} P_i + \frac{1}{2\mu_0} B^2, \tag{2.11}$$

where γ is the adiabatic index of the gas (we consider equal indexes for both gases).

2.1.1 Ionization Considerations

We can simplify these equations by noting that the ionization fraction in molecular clouds and protoplanetary disks is very low, $\rho_i \ll \rho_n$. This can help eliminate many of the ion equations (see §2.2.1). Although we will always be left with ρ_i in the $\beta_{\rm AD}$ term which determines the strength of the ambipolar diffusion (less ion density means stronger diffusion).

The ion density is often expressed as a function of neutral density. One very simple expression, which is often used (Fiedler & Mouschovias, 1993; Hosking & Whitworth, 2004a) is:

$$n_i = K\left(\frac{n_n}{10^5\ \mathrm{cm}^{-3}}\right)^k + K'\left(\frac{n_n}{10^3\ \mathrm{cm}^{-3}}\right)^{-2}, \tag{2.12}$$

where n is a number density, $K = 3 \times 10^{-3}\ \mathrm{cm}^{-3}$, $k = \frac{1}{2}$ and $K' = 4.64 \times 10^{-4}\ \mathrm{cm}^{-3}$. Doing this will allow one to eliminate entirely the need to track the ion density in the single fluid approximation. The second term dies off quickly in the higher density regime, at which point we're left with the common $n_i \propto n_n^{1/2}$ relation.

This expression arises by approximating the results of ionization equilibrium calculations (Elmegreen, 1979; Nakano, 1979) where the sole form of ionization is through cosmic rays (where the cited authors assume a cosmic ray ionization rate of $\zeta_0 = 6.9 \times 10^{-17}\ \mathrm{s}^{-1}$). Cosmic rays can only penetrate so deep into a molecular cloud. A more realistic ionization rate acts more like $\zeta = \zeta_0 \exp\left[-\Sigma/(96\ \mathrm{g\ cm}^{-2})\right]$ (Umebayashi & Nakano, 1981). Stable molecular clouds have average column densities on the order of 0.01 g cm^{-2}, so they feel a constant ionization rate. However, column densities of 100 g cm^{-2} can quickly evolve in collapsing clouds on the order of a free-fall time (Banerjee et al., 2004), so we expect cosmic ray shielding to be important inside pseudodisks formed in pre-Class 0 objects. Furthermore, the constants in Equation (2.12) are dependent on ζ_0 which is very hard to precisely measure and may even depend on where you are in the galaxy (Dalgarno, 2006). In molecular clouds, the ionization rates are observed by measuring chemical abundances and using physical models with chemical networks. The values found tend to lie in the range of $(1-5) \times 10^{-17}$ s^{-1} (Dalgarno, 2006). These values have high uncertainties due to a wide range of physical and chemical models used. Values of 1×10^{-16} s^{-1} have been predicted close to massive stars due to their strong stellar winds (Dalgarno, 2006). These larger values are also predicted by chemical models that emphasize the importance of dust grains and the large polycyclic aromatic hydrocarbons (PAHs) known to exist in the denser regions molecular cores. We are not considering ionizing radiation, such as x-rays from nearby stars, as the star forming environments we consider are quite young.

The second term in (2.12) is often neglected for basic calculations (Safier et al., 1997; Ciolek & Basu, 2006). This will greatly underestimate the ionization at lower densities, thereby overestimating the effect of ambipolar diffusion in such regions[2]. More importantly, the ion density of molecular ions tends to go constant past $n_n > 10^{10}$ cm^{-3} (see Figure 2.1). To complicate things one step further, positively and negatively charged grains become the most abundant source of ionized particles for $n_n > 10^{10}$ cm^{-3} (Tassis & Mouschovias, 2007b; Desch & Mouschovias, 2001; Nakano et al., 2002). This occurs during the later stages of pre-Class 0 collapse.

The overall application of this ionization formula in a code is relatively simple, but may become more complicated once grains become important. A first reasonable step in dealing with ambipolar diffusion in highly time-dependent and 3D calculations is to take (2.12) as the ionization (Kudoh et al., 2007; Ciolek & Basu, 2006; Hosking & Whitworth, 2004a; Safier et al., 1997; Fiedler & Mouschovias, 1993). Further work on

[2]Though Ciolek & Basu (2006) turn off ambipolar diffusion in the low density limit.

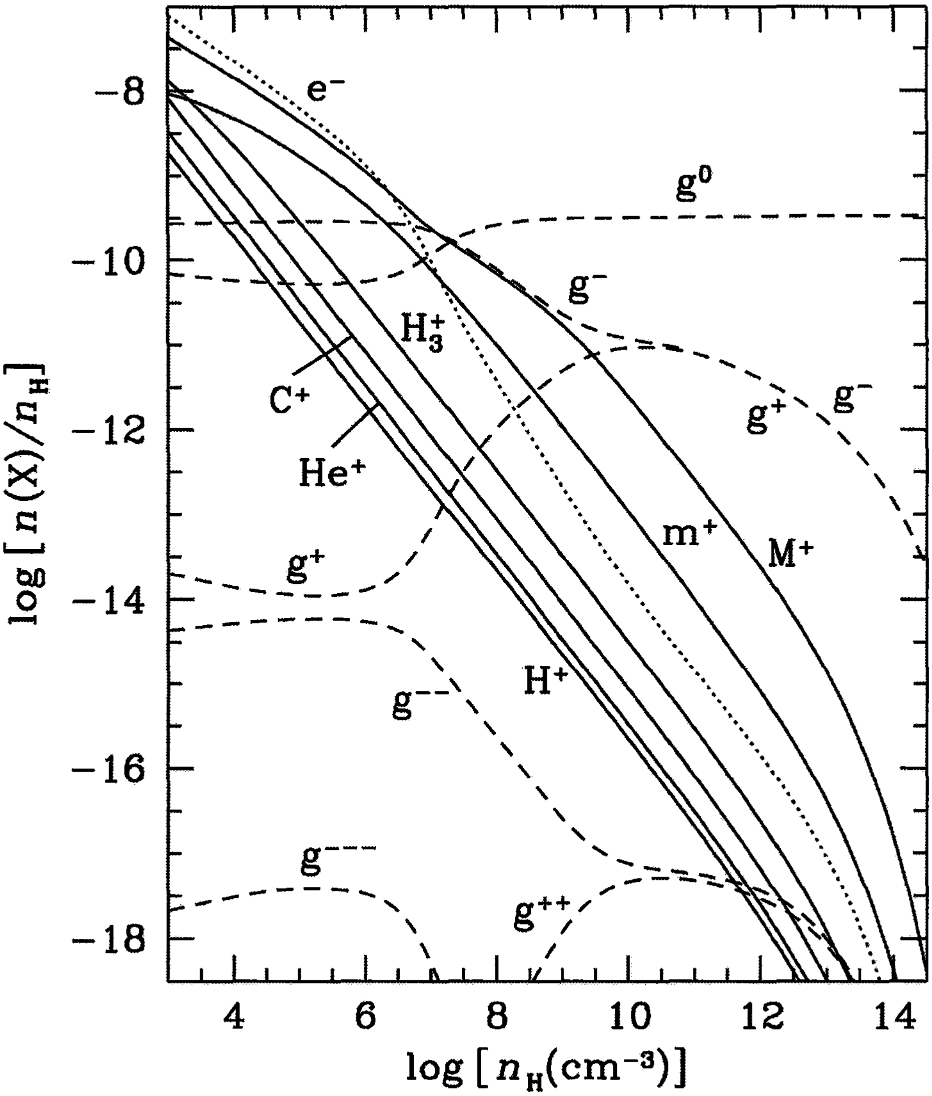

Figure 2.1: The evolution of charged species in the collapse simulation of Nakano et al. (2002). The evolution of grains are the dashed lines and all abundances are relative to n_H. The authors assume $\zeta_0 = 1 \times 10^{-17}$ s^{-1}. We can see the high abundance of ions such as m^+ (charged molecules) and M^+ (charged metals) following a $n_{\rm ions} \propto n_{\rm H}^{1/2}$ distribution up to high densities of about $(10^{12} - 10^{13})$ cm^{-3}. Note the change of charged grain abundance at about $n_H = 10^{10}$ cm^{-3}, where they quickly become the principle charge carrier. A very similar result is found by Tassis & Mouschovias (2007b).

implementing the complications introduced by charged grains can later be developed and readily implemented.

2.2 Approximation Techniques

In this Section we first outline a simple approximation technique applied to the equations of 2.1, and then go on to examine further techniques which are important to develop for later study. We pause in §2.2.2 to discuss the relevance of the label ambipolar *diffusion* and the consequences it implies in terms of computational timesteps. Using two fluids gives one the ability to model more complicated chemistry and there exist methods using multiple fluids that allow the timestep to be increased under certain circumstances; this is discussed in §2.2.3

2.2.1 Carrying Out the Single Fluid Approximation

Our goal in the Section is to make equations (2.1), (2.3), (2.7) and (2.8) look like MHD equations for the neutrals plus some other terms. We note that molecular clouds are dense and poorly ionized. This implies that $\rho_i \ll \rho_n$ which we can use to effectively eliminate the ion equations of motion, saving half the calculations. The ion equations of motion will reduce to give us a relation for the drift velocity which will mediate the intensity of ambipolar diffusion upon the neutrals. This intrinsically assumes a chemistry which does not conserve ion mass explicitly (§2.1.1), but rather the gas density as a whole. Two fluid approaches conserve ion mass, but must introduce chemistry equations with the appropriate mass transfer to properly approximate the ionization (as discussed in §2.1.1)[3]. This would consist of a well chosen list of

[3]There are significant differences between conserved ion mass distributions and ionization dependent distributions. For example, see §3.3.2 for how C-shock equations differ between

equilibrium equations detailing reactions of important ionized species such as Na^+ or charged grains[4].

Reducing the equations, we find that the gravitational and pressure forces for the ions are negligible with respect to the magnetic force $\boldsymbol{f}_m = \boldsymbol{J} \times \boldsymbol{B}$ (where $\boldsymbol{J} = \frac{1}{\mu_0}\boldsymbol{\nabla} \times \boldsymbol{B}$). Also, the momentum of the ions will be negligible in comparison to that of the neutral species. Thus we can neglect (2.2) in comparison to (2.1). Also, (2.4) leaves us the equality:

$$\boldsymbol{f}_f = -\boldsymbol{f}_m = -\boldsymbol{J} \times \boldsymbol{B}, \tag{2.13}$$

from which we can derive:

$$\boldsymbol{u}_d = \beta_{\mathrm{AD}}(\boldsymbol{\nabla} \times \boldsymbol{B}) \times \boldsymbol{B} \tag{2.14}$$

$$\boldsymbol{u}_i = \boldsymbol{u}_n + \beta_{\mathrm{AD}}(\boldsymbol{\nabla} \times \boldsymbol{B}) \times \boldsymbol{B}. \tag{2.15}$$

Substituting (2.15) into (2.7) we can solve to get (simplifying $\boldsymbol{\nabla} \cdot (\boldsymbol{uB} - \boldsymbol{Bu}) = -\boldsymbol{\nabla} \times (\boldsymbol{u} \times \boldsymbol{B})$),

$$\begin{aligned}\frac{\partial \boldsymbol{B}}{\partial t} =& \boldsymbol{\nabla} \times (\boldsymbol{u}_n \times \boldsymbol{B}) - (\boldsymbol{\nabla} \cdot \boldsymbol{B})\, \boldsymbol{u}_n + \boldsymbol{\nabla} \times (\beta_{\mathrm{AD}}\, [(\boldsymbol{\nabla} \times \boldsymbol{B}) \times \boldsymbol{B}] \times \boldsymbol{B}) \\ &- (\boldsymbol{\nabla} \cdot \boldsymbol{B})\, [\beta_{\mathrm{AD}}\, (\boldsymbol{\nabla} \times \boldsymbol{B}) \times \boldsymbol{B}],\end{aligned} \tag{2.16}$$

where the neutrals look to be ideally coupled to the magnetic field save for the two last terms which describe the ambipolar diffusion of the field.

Similarly, in the energy equation of the neutrals (2.8) we substitute into the fric-

different treatments of ion density.

[4]The recombination rate of chemical species is very quick in molecular clouds, so species can be considered in equilibrium with their ambient environment.

tional force (2.13). We recover,

$$\frac{\partial E_n}{\partial t} + \nabla \cdot \left[\boldsymbol{u}_n \left(E_n + P_n + \frac{B^2}{2\mu_0} \right) + \frac{1}{\mu_0} \left(\boldsymbol{u}_n \cdot \boldsymbol{B} \right) \boldsymbol{B} \right] + \nabla \cdot \left[\beta_{\mathrm{AD}} B^2 \left(\boldsymbol{J} \times \boldsymbol{B} \right) \right]$$
$$= \rho_n \boldsymbol{g} \cdot \boldsymbol{u}_n - \frac{1}{\mu_0} \left(\boldsymbol{u}_n \cdot \boldsymbol{B} \right) \left(\nabla \cdot \boldsymbol{B} \right) + \mu_0 \beta_{\mathrm{AD}} \parallel \boldsymbol{J} \times \boldsymbol{B} \|^2$$
$$- \beta_{\mathrm{AD}} \left[\boldsymbol{B} \cdot \left(\boldsymbol{J} \times \boldsymbol{B} \right) \right] \left(\nabla \cdot \boldsymbol{B} \right), \tag{2.17}$$

where the last term on the LHS and the last two terms of the RHS are ambipolar diffusion terms. Heating of the fluid occurs through the dissipation of the field. The rest looks like the MHD energy equation for the neutral species; the total energy of the fluid is changed by the magnetic field as it undergoes motion in the gravitational field.

Let's summarize, making anything with a subscript n unscripted (i.e. representing the gas as a whole). The following is the classic form, where fluxes lie in a divergence on the LHS and sources are placed on the RHS:

$$\frac{\partial \rho}{\partial t} + \nabla \cdot \left(\rho \boldsymbol{u} \right) = 0 \tag{2.18}$$

$$\frac{\partial \left(\rho \boldsymbol{u} \right)}{\partial t} + \nabla \cdot \left(\rho \boldsymbol{u} \boldsymbol{u} + P + \frac{B^2}{2\mu_0} - \frac{1}{\mu_0} \boldsymbol{B} \boldsymbol{B} \right) = -\rho \boldsymbol{g} - \frac{1}{\mu_0} \boldsymbol{B} \left(\nabla \cdot \boldsymbol{B} \right) \tag{2.19}$$

$$\frac{\partial \boldsymbol{B}}{\partial t} + \nabla \cdot \left(\boldsymbol{u} \boldsymbol{B} - \boldsymbol{B} \boldsymbol{u} \right) + \nabla \cdot \left(\mu_0 \beta_{\mathrm{AD}} \left[\left(\boldsymbol{J} \times \boldsymbol{B} \right) \boldsymbol{B} - \boldsymbol{B} \left(\boldsymbol{J} \times \boldsymbol{B} \right) \right] \right)$$
$$= - \left(\nabla \cdot \boldsymbol{B} \right) \boldsymbol{u} - \left(\nabla \cdot \boldsymbol{B} \right) \left[\mu_0 \beta_{\mathrm{AD}} \left(\boldsymbol{J} \times \boldsymbol{B} \right) \right] \tag{2.20}$$

$$\frac{\partial E}{\partial t} + \nabla \cdot \left[\boldsymbol{u} \left(E + P + \frac{B^2}{2\mu_0} \right) + \frac{1}{\mu_0} \left(\boldsymbol{u} \cdot \boldsymbol{B} \right) \boldsymbol{B} \right] + \nabla \cdot \left[\beta_{\mathrm{AD}} B^2 \left(\boldsymbol{J} \times \boldsymbol{B} \right) \right]$$
$$= \rho \boldsymbol{g} \cdot \boldsymbol{u} - \frac{1}{\mu_0} \left(\boldsymbol{u} \cdot \boldsymbol{B} \right) \left(\nabla \cdot \boldsymbol{B} \right) + \mu_0 \beta_{\mathrm{AD}} \parallel \boldsymbol{J} \times \boldsymbol{B} \|^2 \tag{2.21}$$
$$- \beta_{\mathrm{AD}} \left[\boldsymbol{B} \cdot \left(\boldsymbol{J} \times \boldsymbol{B} \right) \right] \left(\nabla \cdot \boldsymbol{B} \right).$$

2.2.2 Diffusion and Ambipolar Diffusion: Typical Timesteps

Note the apparent discrepancy: *ambipolar is not just a diffusion of the field.* Ohmic diffusion, for instance, will add $\nabla \times (\eta \nabla \times \boldsymbol{B})$ to the LHS of the induction equation, where η is the Ohmic diffusivity. The corresponding ambipolar diffusivity is given as (Zweibel, 2002),

$$\eta_{\mathrm{AD}} = \beta_{\mathrm{AD}} B^2, \tag{2.22}$$

where η_{AD} has units of cm^2 s^{-1}. This can be used to re-evaluate the ambipolar diffusion induction term as (Brandenburg & Zweibel, 1994),

$$\nabla \times (\eta_{AD} \nabla \times \boldsymbol{B} - \mu_0 \beta_{\mathrm{AD}} (\boldsymbol{J} \cdot \boldsymbol{B}) \boldsymbol{B}) \tag{2.23}$$

on the LHS. Clearly the second term demonstrates the deviation of ambipolar diffusion from a purely diffusive process.

In fact, it is easy to imagine situations in which $\boldsymbol{J} \cdot \boldsymbol{B} \neq 0$, such as disk accretion in a collapsing core. It would then not be surprising that the extra non-diffusive term becomes important as field lines are strongly oriented against the accretion flow, which caries a charged current. Nonetheless, we use a diffusive method to describe the typical timescale in order to satisfy the Courant condition (Mac Low et al., 1995),

$$\tau_{\mathrm{AD}} = T_0 \frac{(\Delta x)^2}{\eta_{\mathrm{AD}}}, \tag{2.24}$$

where the factor of T_0 is a fudge factor (we use $T_0 = 0.0333$ in our simulations) and Δx is a typical length scale (see §3.2.5). Longer timescales or slower speeds tend to allow sharp gradients in the field to form which lead to instabilities generated by the ambipolar diffusion terms. This creates unphysical states (such as negative densities).

2.2.3 Two Fluids and the Heavy Ion Approximation

Another method to evaluate a partially ionized plasma that is becoming more common is to simply evaluate the equations of the two fluids (eqns (2.1)–(2.9)) separately (Li et al., 2006). In this case the ions will limit the timestep due to their high Alfvén velocities (low densities). In situations where the ionization fraction is small (such as molecular clouds), it is possible to implement a technique which increases the overall timestep 10-100 times while properly tracking the ion density. This *heavy ion approximation* is a current development and involves simply increasing the ion density (and decreasing corresponding factors in β_{AD} keeping it unchanged) thus increasing the timestep. It must be done in very specific conditions, and a series of C-shock tests have shown how well this theoretical variation performs (Li et al., 2006, see corresponding tests of our code in §3.3.2).

One other way that is used to avoid the very short diffusion timesteps described in §2.2.2, is to only run the induction equation through the diffusive step while using an MHD timestep for everything else (O'Sullivan & Downes, 2006, so-called *super time-stepping*). Of course it will take many integrations of the induction equation in order to complete one timestep, and this method will not necessarily reduce the computational time required to evolve the fluid by a significant amount.

2.3 A Review of Developments in Ideal and Non-Ideal Star Formation

2.3.1 Collapse

Star formation is a rather complicated process that includes a zoo of microphysics, as well as having a very wide range of scales. The birth places of stars can be on the order of 10 pc while a stellar radius is on the order of 0.001 AU (a difference of about 9 orders of magnitude in length) with densities ranging from 100 particles per cm^{-3} to average stellar densities of about 1 g cm^{-3} (a difference of about 22 orders of magnitude in density). In addition to significant magnetic fields, we also find complicated cooling mechanisms from the seemingly infinite list of chemical species involved, not to mention non-symmetric turbulent motions. From a theoretical standpoint, the goal is to understand what is happening, but more importantly, what physical process is making it happen. To approach this problem, theorists have made a variety of simplifying assumptions, building up more detailed physical processes along the way.

In the 1950s the picture of star formation was very unclear to say the least; everything was spherical and actual molecular clouds were only to be discovered 20 years later. The main idea was that a very large cloud of gas would condense if dense enough, and as densities became larger, it would fragment due to the Jeans instability (the so-called *gravitational condensation* picture). The corresponding length scale that needed to be reached for fragmentation to occur is called the Jeans length:

$$R_J = \sqrt{\frac{15kT}{4\pi G m \rho}}, \tag{2.25}$$

where T is the temperature, ρ is the density and m is the mass per gas particle. During this process the gas is optically thin to molecular radiation (principally from H_2)

which keeps the gas isothermal; fragmentation presumably stops as the gas becomes optically thick. In this fashion a whole cluster of stars can form. Equation (2.25) will become an important length scale numerical schemes must resolve (see §3.1).

As magnetic fields are introduced into the problem the cloud gains a new support mechanism. Also in the 1950s, large galactic fields were postulated. From this, it was concluded that the magnetic support of a cloud could set an enormous lower limit on the mass a cloud needed in order to condense. Mestel & Spitzer (1956) showed that if clouds are well coupled to a large scale magnetic field of around 1 μG, then only sufficiently massive clouds (around 500 $M_{\odot}$ in their example) can collapse. They noted however that magnetic support would still only be temporary. Coupling between the gas of a core decreases suddenly due to dust grains absorbing most of the charge carriers. Matter will then begin to move somewhat against the field lines in a magnetically supported cloud of gas, allowing it to condense and fragment. This was the first astronomical application of ambipolar diffusion.

The timescale of this process was found to be quite long in static cloud models; simulations by Fiedler & Mouschovias (1993) demonstrate an ambipolar diffusion timescale on the order of 10-20 Myr. Seminal work by Larson (1981) examined the filamentary nature of observed molecular clouds and the role of turbulence. Interstellar turbulence breaks up such quasi-stable clouds on short timescales of about 2 Myr, producing conflicting mechanisms in star formation theory due to contrary timescales of formation. Also, the timescale of ambipolar diffusion regulated star formation is also in conflict with observations of formation timescales for star clusters, such as the ONC where the bulk of star formation is over within 2 Myr (Hillenbrand, 1997).

Because of this, the older astrophysical literature often treats ambipolar diffusion as a star formation mechanism that is counter to turbulent star formation models.

However, more recent work has shown that ambipolar diffusion can also be important in a turbulent medium by spreading out magnetic field structure (Zweibel, 2002). Furthermore, an increased diffusion rate in a turbulent medium allows the quasi-static collapse due to ambipolar diffusion even as turbulent fragmentation takes place (Krasnopolsky & Gammie, 2005).

Prior to the discovery of important turbulent velocities in molecular clouds, work continued on the collapse of isolated cloud cores. Larson (1969) and Penston (1969) did simple non-rotating collapse simulations of uniformly dense spheres. They found increasing flat topped density profiles followed by a $\rho \propto r^{-2}$ decline (Figure 2.3) in addition to mass accretion rates of $(30 - 50)$ $c_{\rm iso}^3/G$ (Hunter, 1977), where $c_{\rm iso}$ is the isothermal sound speed. More recent work using complex 2D and 3D codes reproduces this profile in the isothermal regime (Banerjee et al., 2004), also in the presence of magnetic fields (Machida et al., 2007; Banerjee & Pudritz, 2006) and with a more realistic treatment of the chemistry (Desch & Mouschovias, 2001). When cooling becomes inefficient the profile steepens significantly with respect to r^{-2}, ending the self-similar nature of the collapse (Banerjee et al., 2004).

Much of the modern simulation work starts with either a thin disk approximation (Tassis & Mouschovias, 2007b; Ciolek & Basu, 2006; Nakano et al., 2002; Desch & Mouschovias, 2001; Fiedler & Mouschovias, 1993) studying the quasi-static collapse problem and/or chemical species evolution, or using spheres in pressure equilibrium with an ambient environment, namely a Bonnor-Ebert sphere (Bonnor, 1956; Ebert, 1955)[5]. Work following the latter initial conditions—pioneered by work from Foster & Chevalier (1993)—has investigated many different aspects of the microphysics of collapse, such as cooling (Banerjee et al., 2004), oblique magnetic field braking and

[5]The later citation is often associated with Bonnor-Ebert spheres, though it is in German.

alignment (Machida et al., 2006), angular momentum transport through bars and magnetic fields (Banerjee & Pudritz, 2006), as well as the generation of early outflows and highly collimated jets (Banerjee & Pudritz, 2006; Machida et al., 2007, see Figure 2.2) which act to transport significant amounts of angular momentum and drive high accretion rates of $\dot{M} = (20 - 100)\ c^3/G$.

Ambipolar diffusion is a significant absence from the latter models as it affects processes such as magnetic support, braking, fragmentation, angular momentum transport and outflow generation during the early phases of a star's formation. Currently, authors have included ambipolar diffusion in the study of fragmentation (see §2.3.2), but we are only beginning to look to non-ideal MHD to further solidify our knowledge of the collapse (Machida et al., 2007).

Competing work by Shu (1977), consisting of an isothermal self-similar solution occurring after point-mass formation, argued against the work of Larson (1969) and Penston (1969). It assumed a non-self-similar, but quasi-static collapse to protostar formation (much like the old ambipolar diffusion picture mentioned above). This is followed by an inside-out *expansion wave* collapse that gradually consumes the outer reaches of the gaseous envelope. The outer envelope has a $\rho \propto r^{-2}$ profile while the inner collapsing region behaves more like $\rho \propto r^{-3/2}$ (see Figure 2.4). Mass accretion rates are much smaller, on the order of 0.96 c_{iso}^3/G.

The attraction of an analytic self-similar solution to this complicated problem led to further development, particularly with respect to ambipolar diffusion. Interesting effects of ambipolar diffusion on the self-similar solutions include an outward propagating C-schock (Wardle, 1990, §2.3.3) and *lower* accretion rates around 0.6 c_{iso}^3/G (Krasnopolsky & Königl, 2002; Li, 1999; Safier et al., 1997). Work by by Krasnopolsky & Königl (2002) also incorporated rotation, using a thin disk approximation to

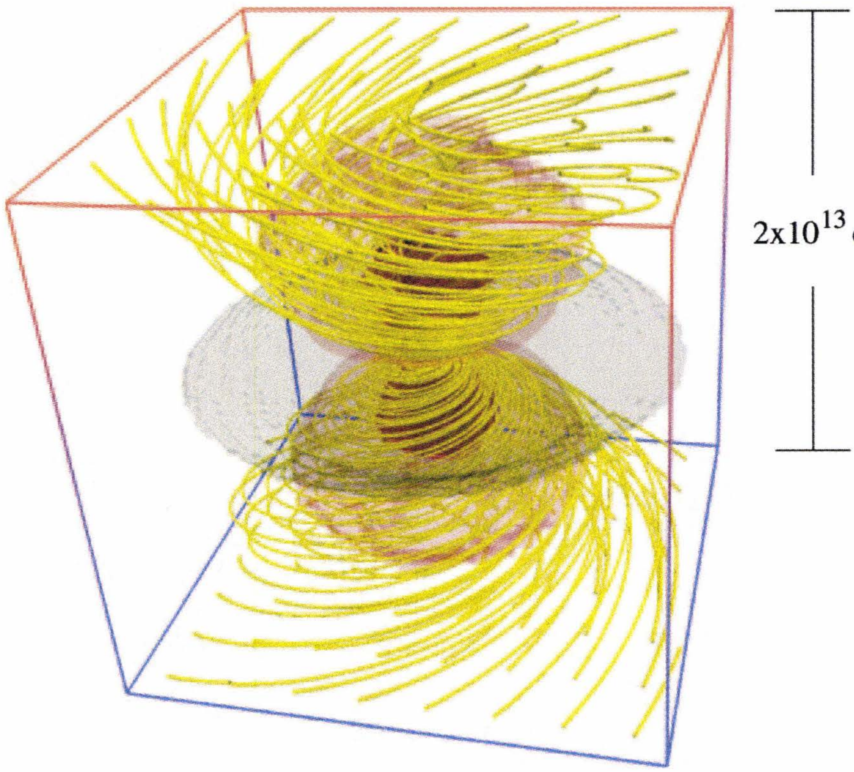

Figure 2.2: Wound up magnetic field lines on the scale of the disk in a Class 0 object, from numerical simulations by Banerjee & Pudritz (2006). This *magnetic tower* (Lynden-Bell, 2003) has initiated a large scale outflow from the disk. In addition, a highly collimated bipolar disk wind is formed, even before the protostar has turned on! Collapse simulations have come a long way since Larson (1969) and Penston (1969). It is now commonplace to use 3D grids with very high refinement, magnetohydrodynamics (MHD), realistic cooling and other complex microphysics. This is leading to concrete predictions and exciting discoveries in star formation.

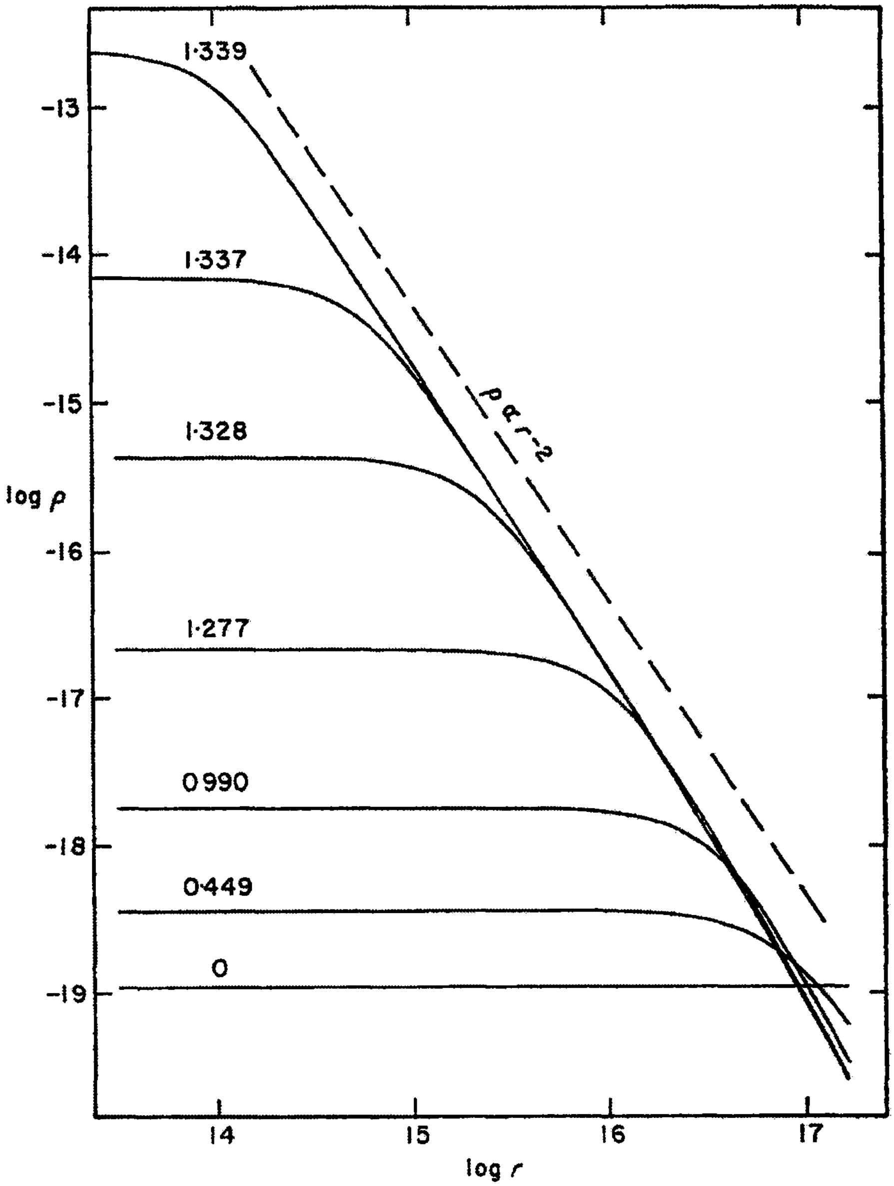

Figure 2.3: The collapse profile of Larson (1969). Time differences are every 10^{13} s, and units are all CGS. Note the flat-topped inner structure followed by the r^{-2} outer profile. The collapse appears self-similar in nature.

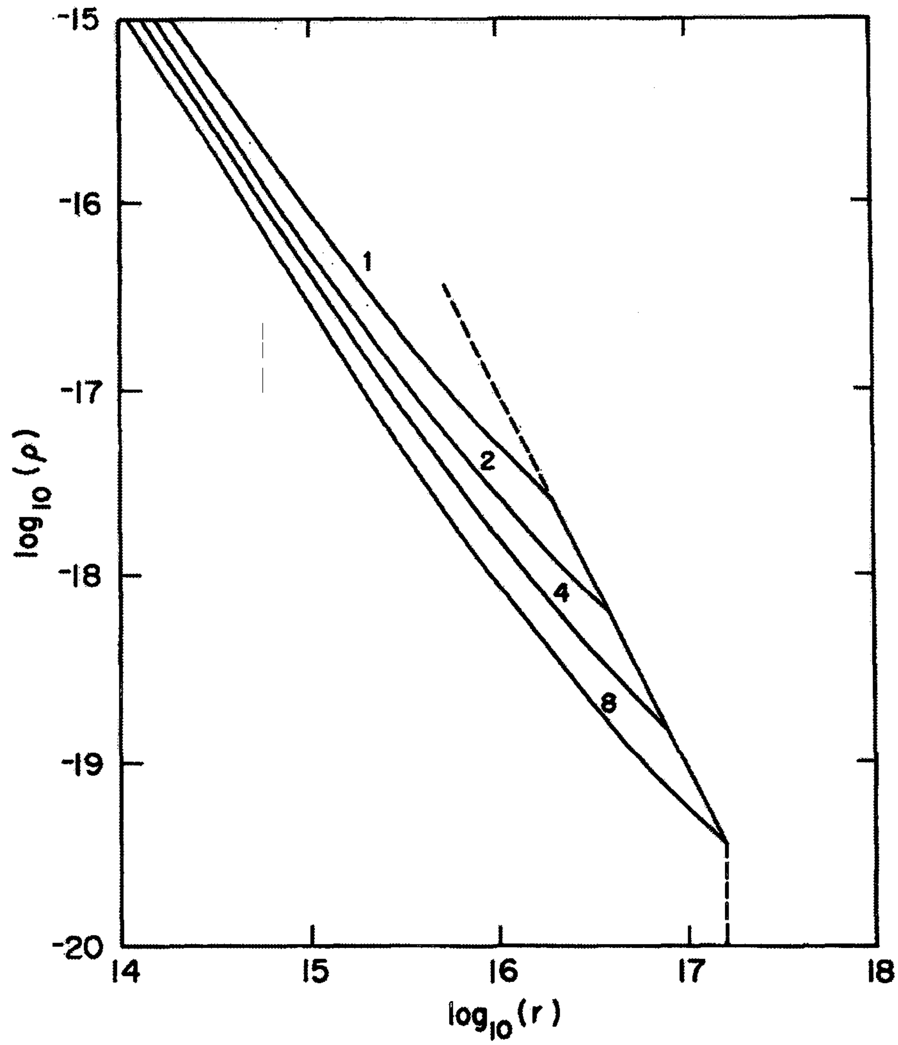

Figure 2.4: The collapse profile of a singular isothermal sphere from Shu (1977). Different curves are marked as occurring at different times defined by the given number multiplied by 10^{12} s (units are all in CGS). Note the inner more flat $r^{-3/2}$ slope and the outer r^{-2} slope and how this contrasts to Figure 2.3. This profile presumes a point mass at $r = 0$.

simplify the dimensionality of the problem.

The clear difference of the accretion rate by 1-2 orders of magnitude between Larson-Penston and Shu models provides a direct observational test. It may be the case that the two processes coexist throughout a star's formation history; an outside-in collapse with high accretion rates followed by an inside-out shock rebounding once the star has formed. Even under turbulent conditions (Banerjee et al., 2006), a Larson-Penston type collapse will still occur, resulting in high accretion rates (that may be able to overcome radiation pressure from a massive protostar) and fragmentation into multiple stars. However, the isothermal sphere of Shu (1977) cannot model such unsymmetric states as posed by turbulence, nor multiple stars as would be caused by fragmentation. It continuously maintains a single star at the center of the cloud and turbulence would destroy the symmetry of the problem that permits a solution.

Going forward, the most important questions during the collapse are: can a partially coupled field reproduce the effects seen in ideally coupled collapses (such as outflows, fragmentation, etc...)? Can we have high enough accretion rates from gravitational collapse in which we can form massive stars, or do we need other larger scale physics (such as mergers)? If ambipolar diffusion carries away magnetic flux, do we still have enough field strength to produce the effects we've seen in previous simulations and through observations; can we build up large fossil fields in stars?

2.3.2 Fragmentation and Magnetic Braking During Collapse

Multi-star systems are prevalent in the Universe. Observations of binaries in our solar neighborhood show that the ratio of stellar systems consisting of multiple stars to the total number of systems is anywhere from 0.3-0.6 (McKee & Ostriker, 2007, and references therein). The hierarchical idea—wherein a core fragments during collapse—

provides a very intuitive model for binary formation. The actual physics involved is still under investigation, but it is readily observed in collapse simulations that instabilities such as bars or rings form due to rotation and often fragment into smaller pieces (Banerjee & Pudritz, 2006; Banerjee et al., 2004; Matsumoto & Hanawa, 2003). This is provided the core is given an adequate initial rotation, such that $\Omega t_{\rm ff} \gtrsim 0.1$. Lesser rotations simply form disks and collapse in this fashion.

In Banerjee & Pudritz (2006) it was observed that magnetic fields stabilized this fragmentation by reducing the rotation of the initial core as well as by stabilizing the disk that eventually forms. Magnetic fields generally provide pressure support during collapse, reducing fragmentation (Price & Bate, 2007). Ambipolar diffusion plays a role in mediating the fragmentation by reducing magnetic braking effects (Hosking & Whitworth, 2004a, Figure 2.5) but it is unclear how magnetic pressure support is affected. Fragmentation using a proper treatment of ambipolar diffusion has only been studied using a smoothed particle hydrodynamics (SPH) code (Hosking & Whitworth, 2004a), which does not handle the $\boldsymbol{\nabla} \cdot \boldsymbol{B}$ very well. A non-SPH code analysis would provide a helpful comparison while providing further insight into the problem.

Magnetic braking was studied analytically and numerically in quasi-static thin disks (Basu & Mouschovias, 1994) and in idealized magnetic rotors (Mouschovias & Paleologou, 1986, 1980). The magnetic rotor is an idealized thin cylinder of a stiff material that rotates with respect to an ambient low density environment, and thus provides us a non-collapsing view of magnetic braking. General results often quoted by this group suggest that magnetic braking effects are only mildly affected "by a few percent" through the introduction of ambipolar diffusion in quasi-static collapse calculations (Basu & Mouschovias, 1994; Mouschovias & Paleologou, 1986).

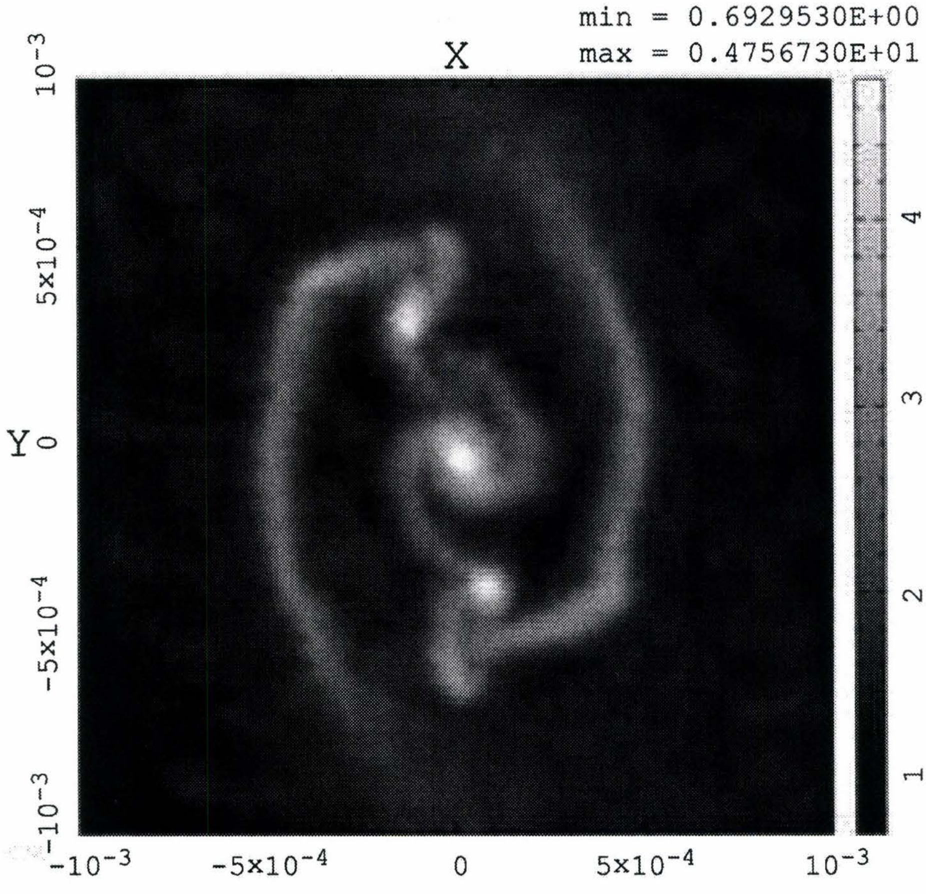

Figure 2.5: Fragmentation of collapsing molecular clouds from Hosking & Whitworth (2004a) in which the infalling material has fragmented into several objects. Hosking & Whitworth (2004a) use an SPH code which utilizes ambipolar diffusion to study fragmentation during collapse of molecular clouds. They claim to be the first such work to have studied fragmentation with a proper treatment of ambipolar diffusion in 3D. Note that the picture has been edited; the numerical values have been redrawn for clarity.

In this manner the role of rotation has been argued to be reduced in thin-disk collapse models.

More recent studies have used a critical Bonnor-Ebert sphere (§3.2.1) for initial conditions. In this fashion, Machida et al. (2006) show the alignment of the magnetic field with the axis of rotation after it is initially mis-aligned. They find magnetic braking of oblique components of the magnetic field significantly stronger than components aligned with the rotation (matching earlier work on magnetic rotors by Mouschovias & Paleologou (1980)). Their results suggest however, that if rotation is strong enough, aligned components will be damped, leaving a purely oblique field generated by MRI (§2.3.4). The criterion for this to happen is $\Omega > \Omega_{\rm crit} = 0.39 B_0 G^{1/2} c_s^{-1}$, where Ω is the rotational frequency, B_0 is the initial field and c_s the isothermal sound speed. For a comparison, parameters used by Banerjee & Pudritz (2007) in their study of the magnetic collapse of a Bonnor-Ebert sphere are borderline to these values. These effects have not been studied with the inclusion of ambipolar diffusion.

The key question is, how strongly does ambipolar diffusion dampen magnetic braking? On one side we see authors studying fragmentation who claim a significant reduction (Hosking & Whitworth, 2004a), while authors studying quasi-static collapse claiming negligible reduction (Basu & Mouschovias, 1994). A more quantitative analysis may prove useful in resolving this issue as magnetic braking is very important in the early stages of collapse.

It is difficult to quantify magnetic braking through the decrease of rotation in a collapse. Gas will spin faster as it is accreted, conserving angular momentum. Also, there exist efficient processes in the collapse which redistribute angular momentum, further changing rotation profiles. In the magnetic rotor, a toroidal magnetic field is wound up by the rotating disk such that:

$$B_\phi(t) = -\sqrt{4\pi\rho r^2}\Omega(t) \tag{2.26}$$

, on the edge of the disk (Mouschovias & Paleologou, 1986), where the toroidal field component is B_ϕ, the cylindrical radial distance is r, the density is ρ and the rotational frequency is Ω. From this, we note that magnetic braking extracts rotational energy ($E_{\mathrm{rot}} \propto r^2\Omega^2$) and transforms it into toroidal magnetic field energy in the envelope ($E_{\mathrm{toroidal}} \propto B_\phi^2$). The efficiency of this process depends on the height from the disk squared. In this way we can relate the Alfvén waves of an outward propagating toroidal field, generated in 3D simulations (Banerjee & Pudritz, 2006), to actual work done on the cloud through magnetic braking. This gives us an effective method to measure braking in a quantitative way during a collapse (§4.3.1).

2.3.3 C-shocks

Shocks are a common occurrence in astrophysics, arising for instance from cloud collisions in a turbulent medium, from supernovae explosions, from collapsing gas that quickly becomes optically thick or from outflows pushing through ambient gas. Analytically, these discontinuous transitions in un-conserved variables (such as velocity or density) are permitted as solutions to the HD or MHD conservation laws. It is important to understand how these structures differ when introducing other physical processes into the mix, such as ambipolar diffusion.

In magnetic flows we can observationally identify shocks as sharp structures in magnetic and hydrodynamic quantities like density, magnetic field, temperature and velocity. However, it is only the charged species in a flow that experience magnetically driven shocks. In a weakly ionized plasma the neutral particles can pass through a shocked ion front and smoothly make the same flow transition in a continuous manner (we call this a C-shock). The criterion for this to occur is that the shock velocity, v_s, be much less than the ion Alfvén speed, v_{A_i} (Draine, 1980). Physically, this means that compression information travels faster along the field lines than in the gas, allowing the field to begin a flow transition sooner than other flow variables (i.e. density). We call this a *magnetic precursor.* The neutral species experience the shock through frictional contact with the ions. We would thus expect to see these smooth shock transitions in low density ($< (10^9 - 10^{10})$ cm^{-3}) environments, such as sites undergoing star formation, but not in the hot ionized medium where ionization is nearly complete and the coupling is strong. Also, shock velocities are expected to be less than about 50 km s^{-1} in order for C-shocks to occur (Draine, 1980).

C-shocks were studied via analytic models by Wardle, (Wardle, 1991a,b, 1990) with a varying field to shock front orientation, using isothermal and non-isothermal models and including radiative cooling and frictional drift heating. The main purpose was to study an interesting instability in C-shock fronts (*Wardle instability*). This instability occurs along C-shocks where there is a strong magnetic pressure gradient and frictional force. The field will buckle under the stress, channeling a flow of gas through the shock. It has been proposed as a method in which fragile H_2 molecules could survive harsh conditions, wherein the mean field strength is strong and shocks are more likely to be unstable (such as Orion-KL; see Figure 2.6). Numerical methods have furthered the study of C-shocks to full 2D, two-fluid MHD models, studying their time-dependent evolution (Smith & Mac Low, 1997) and the Wardle instability in 3D MHD (Mac Low & Smith, 1997, see Figure 2.6). These studies are the first to have ambipolar diffusion in a full 3D MHD code.

Numerical methods have shown that stable C-shocks prove a rather important test for codes implementing ambipolar diffusion as they have analytic solutions (Li et al., 2006; O'Sullivan & Downes, 2006; Mac Low et al., 1995). Test cases are hard to develop for ambipolar diffusion as the equations consist of difficult second order terms. A more qualitative test can be obtained by matching previous computations (such as the quasi-static collapse of Fiedler & Mouschovias (1993); §3.3.1), although it cannot produce percentage error, or perform a convergence test. The physical equations and numerical solutions for C-shocks will be discussed further in §3.3.2.

2.3.4 Dead Zones and Accretion Disks

Accretion disks around young stars are formed in rotating collapses (Machida et al., 2007; Banerjee & Pudritz, 2006; Banerjee et al., 2006; Krasnopolsky & Königl, 2002; Safier et al., 1997). In both Larson-Penston and Shu type models, the disc is often identified by a shock at a distance of about 20-100 AU from the central region. In pre-Class 0 states, the disk is never fully rotationally supported, often kept supported by a combination of magnetic, rotational and thermal pressure gradients. At these densities, ambipolar diffusion in the disk will be significantly strong enough that frictional drift heating (see §2.1) will become important. This is an important point to understand as the disk plays a central role in transporting angular momentum away from the collapsing protostar through disk instabilities (bars, rings) and magnetic effects (mainly magnetic braking, outflows and magnetic torques Banerjee & Pudritz, 2006). The disk is also the birthplace of planets, and its viscous structure is controlled primarily through magnetic turbulence (the magnetorotational instability (MRI)). This viscosity, or the lack of it, is important to a planet's formation and migration (Matsumura et al., 2007).

For MRI to operate in the pre-Class 0 core or disk we require a weak field and

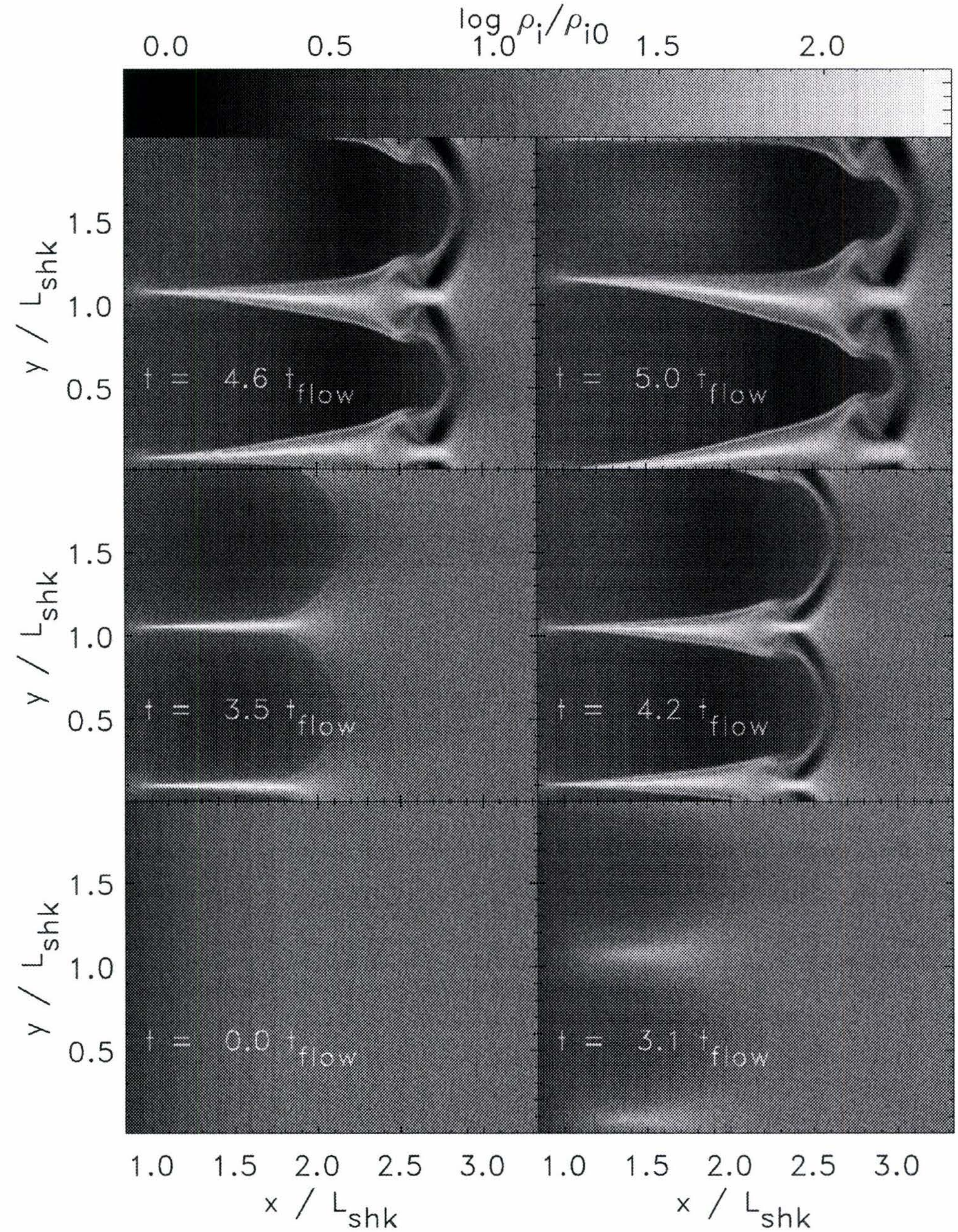

Figure 2.6: Two dimensional images of ion density in an unstable C-shock, demonstrating the evolution of the Wardle instability (Mac Low & Smith, 1997). Ion density is conserved, and this seems to allow the long filaments of gas to break the shock barrier (if ion density is constant, say due to ionizing and other chemical processes, the instability is damped). In this paper the authors also present results of the first 3D MHD simulations involving ambipolar diffusion that we are aware of. They use the ZEUS-MP code with modifications from Mac Low et al. (1995). Initial conditions for the shock are perturbed to allow the instability to form. For definitions of $t_{\rm flow}$ and $L_{\rm shock}$ see §3.3.2.

a rotational frequency that decreases with radius. The latter condition is quantified by requiring $d\Omega/dR < 0$, where R is the cylindrical radius and Ω is the rotational frequency. This will certainly be satisfied in a collapsing, rotating cloud in the pre-Class 0 phase as collapsing material naturally spins up. Studies of local MRI in accretion disks suggest the former condition is satisfied if the magnetic field is *sub-thermal* (Balbus, 2003). We quantify this condition by requiring $c_s > v_{\rm A}$, where $c_s^2 = \gamma_{\rm effective} P/\rho$ is the local sound speed, $\gamma_{\rm effective}$ is the effective adiabatic index of the ideal gas, P is the pressure ρ is the density, $v_{\rm A} = B/(4\pi\rho)^{1/2}$ is the local Alfvèn velocity and B is the magnitude of the magnetic field. This is satisfied at the very early stages of collapse. For example, in reproducing magnetic runs of Banerjee & Pudritz (2007), we find $c_s = (1.55 - 2.55)v_{\rm A}$ (where the uncertainty comes from estimating $\gamma_{\rm effective}$). We expect these values to be larger in a non-ideal run as the field will not build up as efficiently, decreasing B. Rotational frequencies in the disk reach values of $\Omega = 1.0 \times (10^{-12} - 10^{-10})$ s^{-1} over a respective range of distances of $r = (1.0 \times 10^{14} - 1.0 \times 10^{16})$ cm (taken from our simulations performed in §4 of the high mass model). These correspond to rotation times of (30-3000) yr, where collapse times (once dynamic collapse begins) is about 10^4 yr. This then allows enough time for MRI to develop, as it grows on timescales that go as the rotation time. We conclude that MRI could indeed operate in a pre-Class 0 object given these constraints.

The Dead Zone is defined in the literature as being a region in an accretion disk in which the growth rate for the magnetorotational instability (MRI) is much smaller than the rotational time of the disk (Gammie, 1996). The growth rate is damped by resistive MHD effects—Ohmic dissipation, hall electromotive forces, and ambipolar diffusion—such that the overall diffusion speed (diffusivity over some scale L, $v_{\rm diffusion} = \eta/L$; for definition of diffusivity see §2.2.2) is faster than the transport speed of the turbulence v_A (Gammie, 1996). For an accretion disk, the lengthscale L that makes sense is the disk height H (MRI was initially seen as an axial effect in the disk due to simplified field geometries (Kunz & Balbus, 2004)). The choice made by Gammie (1996) for defining a Reynolds number is thus straightforward:

$$\mathrm{Re} = \frac{v_A H}{\eta} \tag{2.27}$$

for Ohmic dissipation, which can be used to quantify dead zones in an accretion disk. When $\mathrm{Re} < 1$, diffusion wins and MRI cannot propagate (though Fleming & Stone (2003) have shown some mixing can occur between active and dead layers). Equation (2.27) has been modified in several more convenient forms through the numerical study of MRI in differentially rotating accretion disks (Fleming et al., 2000). For example,

$$\mathrm{Re}' = \frac{c_s^2}{\eta\Omega}, \tag{2.28}$$

where Ω is the rotational frequency of the disk and c_s is the local sound speed. Numerical simulations have shown that require $\mathrm{Re}' < 10^4$ to break sustained MRI turbulence and allow a dead zone to persist (Fleming & Stone, 2003). Since we are interested more in ambipolar diffusion than Ohmic dissipation as used in the above studies, we naively replace η with η_{AD} to compare effects. When we use the single fluid approximation for η_{AD} we find that $\mathrm{Re}' \propto \rho^{3/2}/B^2 \approx \rho^{1/2}$ (using the relation $B \propto \rho^{0.5}$). From this we'd then expect the largest value of Re' to lie in the densest parts of the disk (the midplane). Using typical values from a collapse (see Chapter 4) the maximum value we find is about 10^2, meaning the whole cloud is "dead" under this analysis. Even though we clearly expect decoupled regions in the disk midplane it is apparently more MRI active than the rest of the cloud!

Recent work by Kunz & Balbus (2004) show that the conditions in which MRI persists in an ambipolar diffusion dominated disk are different than originally discussed by Gammie (1996). These authors demonstrate analytically that the ratio of neutral-ion collisional time ($\tau_{ni} = 1/\gamma_{\rm AD}\rho_i$) to rotational time ($\Omega^{-1}$) is the key parameter to follow. They find that for $\Omega/(\gamma_{AD}\rho_i) > 1$ the growth rate of MRI is severely damped. Analysis of ambipolar diffusion regulated dead zones has never been investigated during collapse (MRI studies alone are rare. Machida et al. (2006) talk of MRI during the pre-Class 0 stage.). Do dead zones gain their initial structure during collapse?

Column densities of a few 100 g cm^{-2} are quickly achieved during numerical runs (Banerjee & Pudritz, 2006). Dead zones with only ambipolar diffusion require $\Omega/\gamma_{\rm AD}\rho_i > 1$, which is automatically obtained if ρ_i exponentially drops to 0. Shielding of cosmic rays (cosmic rays penetrate only to column densities of about 96 g cm^{-2} (Umebayashi & Nakano, 1981, §2.1.1)) may be vital for any final analysis, as the dead zone would certainly be created if there is absolutely no coupling in the disk midplane. In simple chemical models we often see $\rho_i \propto \rho_n^{1/2}$, which makes dead zone creation quite difficult, but not clearly impossible. This will be an interesting avenue for future work to explore, however we can already predict proto-"dead zones" in pre-Class 0 objects starting at column densities of about 100 g cm^{-2}, assuming that the source of ionization is cosmic rays. Do they occur at lower column densities?

Even without a dead zone we still expect layered accretion (where accretion is stronger in disk layers than in the midplane) and dragging in of magnetic field lines by more ionized disk layers (where the field is left behind in the disk midplane). There is a central region of the accretion disk which is not well coupled to the magnetic field, seen to start at about 20 AU (shown in simulations by Desch & Mouschovias (2001)). Note that in such an decoupled region the diffusion speed, $v_{\rm diffusion}$, over the disk is faster than the dragging in of magnetic flux. We quantify this by defining a new "Reynolds number",

$$\mathrm{Re}_{\mathrm{AD}} = \frac{v_{\mathrm{infall}} L}{\eta_{\mathrm{AD}}}, \tag{2.29}$$

which describes the *diffusive* coupling of the field to the gas. This is the Reynold's number for ambipolar diffusion, slightly different from Equation (2.27). The typical length scale L is taken to be the radius of the disk, (e.g. 2.0×10^{14} cm from (Banerjee & Pudritz, 2007)). For $v_{\mathrm{diffusion}} > v_{\mathrm{infall}}$, diffusion is too quick for the gas to drag the field forward, and flux is left behind (at the cost of frictional heating). Field lines would then appear as if they were being dragged in by disk layers, but left behind in the midplane. Note that this does not mean that we have a dead zone as we can still have $v_{\mathrm{A}} > v_{\mathrm{diffusion}} > v_{\mathrm{infall}}$, where the diffusion speed of the field is faster than the infall speed, but not faster than the propagation of MHD turbulence.

As ambipolar diffusion is not purely a diffusion (§2.2.2), we may need to consider a more physical condition in which to declare a decoupled region. We take an idea from C-shock theory,

$$v_{\mathrm{flow}} < \alpha v_{A_i}, \tag{2.30}$$

where α is some parameter we must measure, and $v_{A_i} = B/(4\pi\rho_i)^{1/2}$ is the Alfvén velocity of the ions. It is interesting to compare Equations (2.29) and (2.30). Comparing these two terms will tell us the relative importance of diffusive and non-diffusive effects of ambipolar diffusion. However, the latter condition is sufficient in defining a *decoupled zone* for a purely diffusive, or strongly non-diffusive state. We expect non-diffusive states in an accretion disk, where currents are strongly oriented against field lines and $\boldsymbol{J} \cdot \boldsymbol{B} \neq 0$.

The decoupled zone fits very nicely into the picture we have of layered accretion[6]

[6] The idea originally from Gammie (1996) involved a Keplerian disk; thus the midplane

along coupled layers where (2.29) or (2.30) should be orders of magnitude smaller than in the disk plane. Coupled layers will lose more angular momentum than the midplane through magnetic effects (such as braking and magnetic torque) and this should drive layered accretion in a pre-Class 0 object. This point remains uninvestigated through numerical simulations.

Do we provide the initial conditions of dead zones during the pre-Class 0, initial collapse phase? It is very important to elucidate the initial conditions a dead zone may have, as it has been shown to have important consequences in planet formation models treating migration (Matsumura & Pudritz, 2005), helping to determine final planet masses and stopping planets from entering their parent star. Such a dead zone would be different than is commonly discussed as it is governed by ambipolar diffusion rather than Ohmic dissipation. The former is important at higher densities than considered in pre-Class 0 collapse (Desch & Mouschovias, 2001). We have argued that such an early dead zone is possible for surface densities greater than 100 g cm^{-2}, but dependent entirely on shielding of cosmic rays. Is this a correct statement, or does the chemistry play a strong role at lower surface densities? Also, when the star turns on, what effect will it have on this proto-dead zone? Can it persist?

When the next generation of telescopes are operational (e.g. ALMA), we can expect observations to begin challenging such predictions, and predictions of planet formation.

---

would not accrete at all as it is rotationally supported. Active layers would accrete as they lose angular momentum.

Chapter 3

Numerical Methods

To perform numerical studies of the physical questions raised in Chapter 1 and Chapter 2 we use FLASH2.5 (Fryxell et al., 2000). FLASH provides us the ability to use magnetohydrodynamics in three dimensions while employing adaptive mesh resolution (AMR). Its computational scheme allows very accurate capturing of shocks. We will discuss this further in §3.1. We have performed extensive testing of our code (§3.3), including a new test that we hope will be employed as a standard test for ambipolar diffusion codes which include non-isothermal effects (§3.3.2).

3.1 The FLASH2.5 Code

The FLASH code (Fryxell et al., 2000) employs a wide range of hydrodynamic (HD) and magnetohydrodynamic (MHD) physics. It has been well tested and has become quite popular in the astrophysical community. Its principal advantage is that it can perform AMR, as this saves considerable computational time while maintaining a high level of refinement. A secondary, though important advantage for astrophysicists, is that it does a very good job in capturing shocks.

Adaptive mesh refinement in FLASH looks at a specific set of characteristics of a cell in the computational region and correspondingly marks its parent block for refinement, de-refinement or a stay. A block of cells consists of 8^n cells, where n is the dimensionality of the simulation. If it is marked for refinement, a block is split into a set of new blocks such that the spacing between each original cell is halved. A cell represents the smallest spatial extensions in a simulation and holds hydrodynamic values. Any block has neighbors differing in refinement by at most 1.

In this way AMR allows one to have a large number of highly refined cells around a small scale disk on the order of 10^{13} cm^{-3} and a small number of large cells refining the collapsed cloud on the scale of 10^{19} cm^{-3}. This will save computational time in decreasing the number of total cells while maintaining adequate refinement for the problem.

The refinement criteria for FLASH have been adjusted somewhat in previous work by Banerjee et al. (2004). It was shown by Truelove et al. (1997) that one needs to refine the Jeans length,

$$\lambda_J = \left(\frac{\pi c_s^2}{G\rho}\right), \tag{3.1}$$

by at least four cells in an AMR code, where c_s is the isothermal sound speed, G is Newton's constant and ρ is the local density. If this is not satisfied artificial fragmentation induced by the numerical grid will result. Banerjee et al. (2004) setup the refinement criteria such that a variable fraction of cells will resolve the Jeans length. In our production runs we use 8 - 24 cells per Jeans length, guaranteeing artificial fragmentation will be avoided.

The ideal MHD equations, alongside the optional resistive and viscous terms[1] are

[1]The resistive MHD terms were added by Timur J. Linde and collaborators (private communication), and are as of yet untested. We found a minor yet significant typo in the code while checking it against its theoretical basis. This typo has since been corrected in

implemented in FLASH. These include viscosity, heat conductivity, hyper-resistivity, hall electromotive forces and Ohmic dissipation. We write the MHD equations implemented in FLASH including the latter two effects as they are magnetic processes and served as models of our implementation of ambipolar diffusion. Note the $\nabla \cdot \boldsymbol{B}$ terms and recall similar MHD equations with ambipolar diffusion derived in §2.2.1 (equations (2.18-2.20)):

$$\frac{\partial \rho}{\partial t} + \nabla \cdot (\rho \boldsymbol{v}) = 0 \tag{3.2}$$

$$\frac{\partial \rho \boldsymbol{v}}{\partial t} + \nabla \cdot \left(\rho \boldsymbol{v}\boldsymbol{v} + P + \frac{1}{2}B^2 - \boldsymbol{B}\boldsymbol{B}\right) = \rho \boldsymbol{g} - \boldsymbol{B}\left(\nabla \cdot \boldsymbol{B}\right) \tag{3.3}$$

$$\begin{aligned}\frac{\partial \boldsymbol{B}}{\partial t} + \nabla \cdot (\boldsymbol{v}\boldsymbol{B} - \boldsymbol{B}\boldsymbol{v}) - \nabla \cdot (\eta_{\text{Ohmic}} \nabla \cdot \boldsymbol{B}) = & -\nabla \times (\eta_{\text{Ohmic}} \boldsymbol{J}) - \boldsymbol{v}\left(\nabla \cdot \boldsymbol{B}\right) \\ & - \nabla \cdot \left[\eta_{\text{hall}} \left(\boldsymbol{B}\boldsymbol{J} - \boldsymbol{J}\boldsymbol{B}\right)\right]\end{aligned} \tag{3.4}$$

$$\begin{aligned}\frac{\partial E}{\partial t} + \nabla \cdot \left[\boldsymbol{v}\left(E + P + \frac{1}{2}B^2\right) - \boldsymbol{B}\left(\boldsymbol{v} \cdot \boldsymbol{B}\right)\right] = & \rho \boldsymbol{g} + \nabla \cdot \left[\boldsymbol{B} \times (\eta_{\text{Ohmic}} \boldsymbol{J})\right] \\ & + \nabla \cdot \left(\eta_{\text{hall}} \left[B^2 \boldsymbol{J} - (\boldsymbol{J} \cdot \boldsymbol{B})\,\boldsymbol{B}\right]\right) \\ & - (\boldsymbol{v} \cdot \boldsymbol{B})\left(\nabla \cdot \boldsymbol{B}\right),\end{aligned} \tag{3.5}$$

where ρ is the density, $\boldsymbol{v}$ is the velocity, t is time, $\boldsymbol{B}$ is the magnetic field, $\boldsymbol{J} = \nabla \times \boldsymbol{B}$ is the current density, P is the pressure, $\boldsymbol{g}$ is the gravitational field, E is the energy, η_{Ohmic} is the Ohmic diffusivity (resistivity) and η_{hall} is the hall diffusivity. We use dimensionless units (§3.2.4), so μ_0 is 1. We ignore these non-ideal effects (setting

current distributions of FLASH2.5.

$\eta_{\mathrm{Ohmic}} = \eta_{\mathrm{hall}} = 0$), though we note that they will be of interest in further work (Chapter 5).

In the above equations we call anything that can be put into a divergence a *flux term* as it describes the redistribution rate of the parameter in the time derivative. An example of a flux is the Ohmic dissipation term on the right hand side of equation (3.4); Ohmic dissipation depends on field gradients ($\boldsymbol{J}$ terms) and tends to make the field more uniform. It does not the generate or dissipate $\boldsymbol{B}$. Anything that is not a flux (save for the time derivative) we call a *source term* as it describes the generation and destruction rate of the parameter in the time derivative. Anything that heats or cools is an example of a source in equation (3.5), such as the gravitational term which describes heating due to collapse.

Because the code does not strictly conserve $\nabla \cdot \boldsymbol{B} = 0$ (§3.1.1) we can symmetrize the ideal MHD equations above (ignoring non-ideal terms). This allows for a unique solution to the Riemann Problem across cell boundaries (e.g. Powell et al. (1999)).

A Riemann Problem consists of solving the conservative laws across cell boundaries (i.e. a one step initial condition). The Riemann problem in MHD was outlined by Sergei K. Godunov (Godunov, 1959), and solvers following his work are often attributed as being a *Godunov scheme.* Riemann solvers are computationally expensive so approximate solvers are developed which do a very good job, but make sense numerically. The so-called *8-wave solver* described by Powell et al. (1999), and used in FLASH, is such a scheme. The eighth wave describes the propagation of $\nabla \cdot \boldsymbol{B}$.

In the FLASH module, solutions following this approximation are *split.* This means that the MHD equations are solved in *sweeps* of each direction, for each timestep. A sweep involves evolving the equations along x, y and z components separately (sources are also split up into three terms). This affects how averaging over the sweep direction is done (see §3.2). We describe in §3.2.3 the implementation and splitting of ambipolar diffusion fluxes and sources derived in §2.2.1.

One further aspect of FLASH that needs only minor attention is the *materials* package. FLASH has a built in set of modules that handle multiple species of particles, atoms or molecules (designed for solar nuclear reaction networks, but applicable to whatever chemistry you wish to implement). For our purposes however, we simply use it to set the molecular masses that we require in varying test problems and in the main runs. Our main runs, describing the collapse of Bonnor-Ebert spheres (§3.2.1), contain a chemistry of H_2, H, and Z (metals), where H_2 dominates, but where H can form through dissociation of H_2 (see §3.2.2).

3.1.1 $\nabla \cdot \boldsymbol{B}$ Considerations

The MHD module in FLASH employs a somewhat controversial scheme that does not explicitly constrain $\nabla \cdot \boldsymbol{B} = 0$, based on Powell et al. (1999)[2]. The $\nabla \cdot \boldsymbol{B}$ terms are left in all of our equations to emphasize this fact: $\nabla \cdot \boldsymbol{B}$ *is* not *explicitly zero in FLASH, but constrained below truncation-level error after each timestep* (Powell et al., 1999). Considering these terms during a timestep is thus important in guaranteeing the stability of any computational scheme applied to FLASH's MHD module. We find it helps decrease $\nabla \cdot \boldsymbol{B}$ by a couple orders of magnitude in our main runs, however it may not be important in more steady flows. Note that we are also using a method employed in FLASH which eliminates $\nabla \cdot \boldsymbol{B}$ as it's created through a simple diffusive method (described below).

The evolution of $\nabla \cdot \boldsymbol{B}$ in our isothermal C-shock test (§3.3.2) evolves very much

[2]The code has been well tested and, despite the controversy, is widely used in numerical simulations as one of the "go to" codes for AMR-based MHD simulations.

the same with or without these extra terms (there is only a minor advantage of having such terms in the code). As the shock reaches a steady state, the average value remains constant. We note that this former case involves small integration times of a few hours and a steady state, whereas the collapse performed in Chapter Chapter 4 is continually evolving over integration times of a few days. In a general sense it may be advisable to only use these terms if $\nabla \cdot \boldsymbol{B}$ becomes an issue (as in the collapse calculations performed in Chapter 4). Otherwise, skipping the lines of code pertaining to these terms could save important computing time.

Including $\nabla \cdot \boldsymbol{B}$ terms makes the MHD equations symmetrizable, allowing for a Godunov scheme to be employed (as discussed in §3.1). The advantage of this method permits one to use the 8-wave, approximate Riemann solver employed by Powell et al. (1999). This method provides very accurate shock capturing, which is important for practically any astrophysical problem (in particular our molecular core collapse). The principal disadvantage is that significant values of $\nabla \cdot \boldsymbol{B}$ lead to incorrect physics. This is corrected by constraining such values below numerical truncation-level values (via the diffusive method in FLASH). Even if values are small, we are left with the physical dissatisfaction of having $\nabla \cdot \boldsymbol{B} \neq 0$, though we note all numerical values are only approximately correct.

Comparisons following seven different codes, including the above method used in FLASH, show that the 8-wave solver can generate incorrect shock jump conditions (incorrect J-shocks) due to the erroneous generation of $\nabla \cdot \boldsymbol{B}$ (Tóth, 2000). For this reason FLASH also employs a simple diffusive cleaning mechanism which destroys the generation of $\nabla \cdot \boldsymbol{B}$ at the rate in which it is created by numerical diffusion of the field. This is a numerically inexpensive routine which generally works very well. An optional cleaning method which projects the numerical solution of $\boldsymbol{B}$ to a 0 divergence state is also available if necessary, though computationally more expensive. This latter method has been shown to be very effective in keeping $\boldsymbol{\nabla} \cdot \boldsymbol{B}$ below truncation-level error (Tóth, 2000). We use the diffusive method in all of our simulations.

Smooth Particle Hydrodynamic (SPH) MHD codes are also known to typically have problems with $\boldsymbol{\nabla} \cdot \boldsymbol{B} = 0$. We compared our $\boldsymbol{\nabla} \cdot \boldsymbol{B}$ with that of Hosking & Whitworth (2004a)—which performs a similar numerical simulation to ours—and demonstrate the effectiveness of our scheme (though it is hard to interpret the individual importance of these numbers). We find a maximal value at the end of our simulation (Chapter 4) of $|\boldsymbol{\nabla} \cdot \boldsymbol{B}|_{\text{max}} = 1.11 \times 10^{-15}$ G cm^{-1}, in comparison to the maximal values of 10^2 G cm^{-1} (and average values of 5.0 G cm^{-1}) of (Hosking & Whitworth, 2004a, they use SI units.)! Note that our values come from very large integration times of a few days (real time), and about 2 Myr (simulation time). Note that we use the diffusive cleaning method employed in FLASH, while (Hosking & Whitworth, 2004a) use there own unique developed cleaning method. We conclude that, relative to an SPH calculation, we rigorously maintain zero divergence of the field.

A more recent AMR MHD code developed by Stone & Gardiner (2005) (ATHENA) has improved the Godunov scheme by conserving $\boldsymbol{\nabla} \cdot \boldsymbol{B} = 0$ through constrained transport (CT) methods. The very popular static grid code ZEUS also employs CT. Although we have presented results that show we can contain $\boldsymbol{\nabla} \cdot \boldsymbol{B}$ terms, we may wish to look at such a code in the future to completely enforce this strict physical law.

3.2 Implementation of New Physics into FLASH

3.2.1 Initial and Boundary conditions

The density distribution of a cloud of gas in a near-critical hydrostatic equilibrium with a more uniform inter-cloud medium can be analytically solved and is commonly called a Bonnor-Ebert (B-E) sphere (Bonnor, 1956; Ebert, 1955). The popularity of B-E spheres is due in part to their similarity to a Larson-Penston type profile; a flat inner density profile matched continuously with a $\rho \propto r^{-2}$ outer profile. The characteristics of a B-E sphere seem aesthetically favourable as an initial condition for star formation.

However, it is the observational (Alves et al., 2001), as well as the computational evidence (Tilley & Pudritz, 2004) that has supported the use of B-E spheres as an accurate initial condition to star formation. The mapping of the density profile of the Barnard 68 (B68) molecular cloud core through dust extinction of background stars is shown in Figure 3.1. There is a near exact correlation of B68's profile to the fitted profile of a B-E sphere. Many cores have since been observed to share such a profile. Even formation of molecular clouds through hydrodynamic turbulence seems to form B-E spheres (Tilley & Pudritz, 2004), among other profiles. Thus we note that while a proper 3-D turbulent core from such simulations may prove a true realistic initial condition (such as was done in the work by Banerjee et al. (2006)), the Bonnor-Ebert sphere provides a very accurate first step to studying core collapse.

The analytical solution of a B-E sphere's density profile reduces to a differential equation of the gravitational potential in terms of the spherical radius. This equation

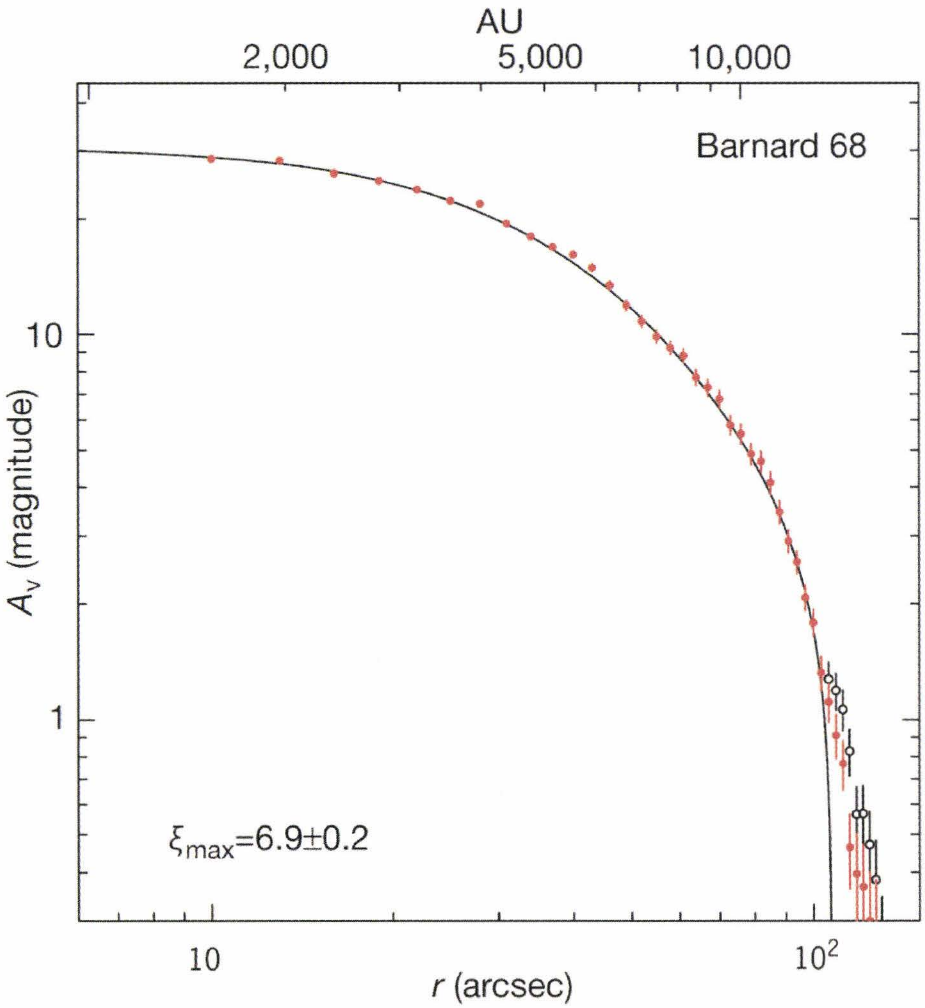

Figure 3.1: Visual extinction profile of Barnard 68 (from Alves et al. (2001)). The visual extinction is directly proportional to the column density along the line of sight. Barnard 68 is not completely spherical, so the red points indicate the observed profile excluding non-spherical features, while the black open points refer to the cloud as a whole. The solid line represents the best fit B-E sphere profile and it is clear that the fit is very good.

is the Lane-Emden equation,

$$\frac{1}{\xi^2}\frac{d}{d\xi}\left(\xi^2\frac{d\phi}{d\xi}\right) = e^{-\phi}, \tag{3.6}$$

where $\xi = r/r_0$, $r_0 = c_s/\sqrt{4\pi G\rho_0}$ is a characteristic length scale, c_s is the isothermal sound speed, ρ_0 is the central density, $\rho(\xi) = \rho_0 e^{-\phi(\xi)}$ is the density profile, and $\phi(\xi)$ is equal to the gravitational potential plus a constant. The variable $\phi(\xi)$ satisfies the boundary conditions,

$$\phi(0) = \frac{d\phi}{d\xi}(0) = 0. \tag{3.7}$$

Solutions with $\xi > \xi_c \approx 6.5$ are unstable to collapse and solution profiles must be interpolated from stable solutions. The module in the setup which calculates the density profile is carried over from previous work (Banerjee et al., 2004).

Our initial setup consists of a B-E sphere in hydrostatic equilibrium with an external medium. The density profile of the sphere is given a 10% over-density and a $m = 2$ perturbation ($\rho = \rho_{\rm BE}[1.0 + 0.1\sin(2\theta)]$) to ensure collapse. We use a large box with periodic boundary conditions, such that the box is large enough to ignore "rebounding" effects that may occur. In turn we give the B-E sphere a bit of a spin, in line with observations that suggest B68 has a rotational energy a few percent of it's gravitational energy. A small initial field is given such that the core remains supercritical to collapse. We employ two models, a low mass model matching characteristics of B68, and a high mass model which matches characteristics of high mass clouds observed by Chini et al. (2004). The parameters are given in Table 3.1.

The magnetic field is distributed such that the parameter $\beta = P/(B^2/8\pi)$ is constant, where $P = \rho c_s^2$ is the ideal pressure. The non-ideal version of the high-mass model is given $\frac{3}{4}$ the rotation of the ideal run to better match the final rotational characteristics during collapse (braking is less efficient in the non-ideal run §4.3.1).

Table 3.1: The parameters for our collapse runs. Note that the high-mass model for our non-ideal run is given $\frac{3}{4}$ the rotation of the ideal run, so $\Omega_{\mathrm{HM\ AD}} = 8.27\times10^{-15}\ \mathrm{s}^{-1}$.

model	ρ_0 [g cm^{-3}]	c_s [km s^{-1}]	$c_{s_{\mathrm{ext}}}$ [km s^{-1}]	β	$B_{\max}$ [μG]	Ω [s^{-1}]
high-mass	3.35×10^{-21}	0.408	1.289	76.0	1.36	1.10×10^{-14}
low-mass	9.81×10^{-19}	2.458	7.774	84.0	14.0	1.89×10^{-13}

The low mass run has shown a stronger tendency to generate outflows and to fragment (Banerjee & Pudritz, 2006), thus we keep the rotations the same in this case to better study the effects of braking.

3.2.2 Building on Added Physics

Our collapse simulations contain cooling rates taken from previously developed models (Banerjee et al., 2004, 2006). These models have developed methods in which to incorporate the cooling due to collisional excitation of molecules such as H_2, H, O, CO, O_2, HCl, C and O (Banerjee et al., 2004). Effects of dust-gas interactions were incorporated by Banerjee et al. (2006) along with H_2 dissociation at high temperatures and a radiative diffusion approximation in the optically thick limit. This provides a more realistic method with which to account for the sudden change in the equation of state in a collapsing cloud, when cooling becomes inefficient. Many authors use a variable equation of state which jumps from isothermal to adiabatic (or something similar) at a given density (Tassis & Mouschovias, 2007a; Machida et al., 2006). Also, it forbids the analysis of effects like drift heating and energy distribution by diffusion by eliminating the energy equation.

3.2.3 Implementation of Ambipolar Diffusion

To put the equations in code form we will have to first separate sources and fluxes, and then add these to the FLUX and SOURCE arrays during the sweeping process of MHD_SWEEP.F90 in FLASH2.5. This module performs the sweeps, calls the interpolation of the data for ideal terms and calls fluxes and sources for a given sweep direction (including non-ideal data). After this, it evolves the MHD equations. In coding the ambipolar diffusion terms we follow closely how the resistive fluxes are applied (see MHD_ADD_RESISTIVE_FLUXES.F90 in FLASH2.5). They use a central difference method to discretize derivatives ($\nabla \times \boldsymbol{B}$ terms) at cell centers. This should be an effective method as the ambipolar diffusion terms, like the Ohmic dissipation terms, are parabolic in nature. They won't require the highly involved interpolation the rest of the MHD equations undergo to be accurate (the ideal MHD equations are hyperbolic).

To illustrate the central differencing technique, we evaluate an imaginary flux term of the form

$$F = \left(\frac{A_{i,j,k}B_{i,j,k}}{C_{i,j,k}}\right) + \frac{dD_{i,j,k}}{dx_{i,j,k}} + \frac{D_{i,j,k}}{dy_{i,j,k}}, \tag{3.8}$$

where i,j, and k locate a given cell in the current block and A, B, C, D, x and y are evaluated at cell centers. The x and y coordinates are represented by $x_{i,j,k}$ and $y_{i,j,k}$ respectively (we omit the z coordinate for simplicity). Let the sweep direction be the x direction, and averaged terms be represented by a line over the character. Our averaging technique is as follows[3],

$$\overline{A} = 0.5\left(A_{i,j,k} + A_{i-1,j,k}\right), \tag{3.9}$$

[3]Note that we have also used a similar averaging technique which averages final terms as a whole, rather than basic values (like B_x, β_{AD} or in this imaginary case, A). We find no significant difference between the two. However, the one presented here more closely resembles that which is already employed in the FLASH code.

where $\overline{B}$ and $\overline{C}$ are found in a similar fashion. Derivatives in line with the sweep follow:

$$\frac{dD}{dx} = \left(\frac{D_{i,j,k} - D_{i-1,j,k}}{x_{i,j,k} - x_{i-1,j,k}}\right). \tag{3.10}$$

Derivatives that are against the sweep follow this form:

$$\frac{dD}{dy} = 0.5\left(\frac{(D_{i,j+1,k} - D_{i,j-1,k}) + (D_{i-1,j+1,k} - D_{i-1,j-1,k})}{y_{i,j+1,k} - y_{i,j-1,k}}\right). \tag{3.11}$$

Thus our final flux term will have the form:

$$F = \left(\frac{\overline{A}\,\overline{B}}{\overline{C}}\right) + \frac{dD}{dx} + \frac{dD}{dy}. \tag{3.12}$$

Now we will evaluate the ambipolar diffusion flux terms and put them in a form that makes sense for computation. In the code we have applied the above averaging technique. Please note our matrix notation for flux terms corresponding to $\boldsymbol{B}$. We have chosen to make each column correspond to B_x, B_y and B_z from left to right. Rows for flux and source vectors or matrices correspond to the direction of the sweep; x direction, y direction and z direction from top to bottom. For example, during a sweep in the x direction the flux terms only receive additions from the first component in the corresponding vector.

For simplicity we define the vector,

$$\begin{aligned}\boldsymbol{A} &= -\beta_{\mathrm{AD}}\boldsymbol{B} \times [\boldsymbol{B} \times (\boldsymbol{\nabla} \times \boldsymbol{B})] \\ &= -\beta_{\mathrm{AD}}\begin{pmatrix} B_x(B_y j_y + B_z j_z) - j_x(B_y^2 + B_z^2) \\ B_y(B_x j_x + B_z j_z) - j_y(B_x^2 + B_z^2) \\ B_z(B_x j_x + B_y j_y) - j_z(B_x^2 + B_y^2) \end{pmatrix},\end{aligned} \tag{3.13}$$

where $\boldsymbol{j} = \boldsymbol{\nabla} \times \boldsymbol{B}$.

We find that the flux vectors for the magnetic field components are,

$$\begin{pmatrix} \boldsymbol{F}_{B_x} & \boldsymbol{F}_{B_y} & \boldsymbol{F}_{B_z} \end{pmatrix} += \begin{pmatrix} 0 & -A_z & A_y \\ A_z & 0 & -A_x \\ -A_y & A_x & 0 \end{pmatrix}. \tag{3.14}$$

Similarly we define the vector,

$$\begin{aligned} \boldsymbol{a} &= (\boldsymbol{j} \times \boldsymbol{B}) \\ &= \begin{pmatrix} j_y B_z - j_z B_y \\ j_z B_x - j_x B_z \\ j_x B_y - j_y B_x \end{pmatrix}, \end{aligned} \tag{3.15}$$

for the source. The sources for (2.20) are coded as follows (only terms with a β_{AD} need to be added, others are already taken care for):

$$S_B += -\beta_{\mathrm{AD}}(\boldsymbol{\nabla} \cdot \boldsymbol{B}) \begin{pmatrix} a_x & 0 & 0 \\ 0 & a_y & 0 \\ 0 & 0 & a_z \end{pmatrix}, \tag{3.16}$$

where I have split up the source into a vector for each direction for simplicity (following my notation outlined above).

The energy flux works out to,

$$\boldsymbol{F}_E += -\beta_{\mathrm{AD}} B^2 \begin{pmatrix} a_x \\ a_y \\ a_z \end{pmatrix}. \tag{3.17}$$

The ambipolar diffusion heating term works out to,

$$\boldsymbol{S}_E += \beta_{\mathrm{AD}} \begin{pmatrix} a_x^2 \\ a_y^2 \\ a_z^2 \end{pmatrix}, \tag{3.18}$$

where again I've chosen how to split up the source.

Finally, the $\boldsymbol{\nabla} \cdot \boldsymbol{B}$ source term works out to,

$$\boldsymbol{S}_E \mathrel{+}= -\beta_{\mathrm{AD}} \begin{pmatrix} (B_x a_x)(\boldsymbol{\nabla} \cdot \boldsymbol{B}) \\ (B_y a_y)(\boldsymbol{\nabla} \cdot \boldsymbol{B}) \\ (B_z a_z)(\boldsymbol{\nabla} \cdot \boldsymbol{B}) \end{pmatrix}, \tag{3.19}$$

where I've chosen to split the source term up partly to save coding and match the usage of $\boldsymbol{a}$'s components in Equation (3.16). The energy equations in this form are quite efficient, relying on the calculation of only one component of $\boldsymbol{a}$ for each sweep.

3.2.4 Units, Constants and Dimensionality

One advantage of FLASH is that the dimensionless constants are all 1.0, save the constant for the magnetic field. The four principle scaling constants are (Powell et al., 1999):

$$\begin{aligned} a_\infty &= 1.0 \ \left[\frac{\mathrm{cm}}{\mathrm{s}}\right] \\ \rho_\infty &= 1.0 \ \left[\frac{\mathrm{g}}{\mathrm{cm}^3}\right] \\ L &= 1.0 \ [\mathrm{cm}] \\ \mu_0 &= 4\pi \ \left[\frac{\mathrm{cm\ s^2\ G^2}}{\mathrm{g}}\right], \end{aligned} \tag{3.20}$$

from which most variables can be made dimensionless through combinations of these constants.

Important examples are the magnetic field, $B' = (a_\infty\sqrt{\rho_\infty \mu_0})^{-1} B$ and $\beta'_{\mathrm{AD}} = a_\infty \rho_\infty L^{-1} \mu_0 \beta_{\mathrm{AD}}$. Otherwise, all other variables are quite straightforward. One can imagine equations (2.18-2.20) the same, but drop all μ_0 terms to 1.

3.2.5 Timesteps

The timestep is taken from equation (2.24) and written as:

$$\begin{aligned}\tau_{\mathrm{AD}} &= T_0 \frac{(\Delta x)^2}{\eta_{\mathrm{AD}}} \\ &= T_0 \left[\frac{(x_{i,j,k} - x_{i-1,j,k})^2}{\overline{\beta_{\mathrm{AD}}}\ \overline{B}^2} \right],\end{aligned} \tag{3.21}$$

where T_0 is typically chosen as $\frac{1}{30}$ or $\frac{1}{120}$ in our runs (the latter factor is used in Mac Low et al. (1995)). We find little difference between the two while anything larger tends to quickly create un-physical states such as negative densities and sharp magnetic field gradients.

The Δx represents the coordinate of the sweep, so it would be Δz if the sweep was in the z direction. The smallest such timestep in a sweep is given to the timestep chooser which multiplies the smallest timestep from all processes by a CFL factor of typically 0.8. The ambipolar diffusion timestep is small and usually dominates over other timesteps (such as from the cooling or hydrodynamic processes).

3.3 Testing the Code

To test the code we have performed first a qualitative check in §3.3.1 and a more detailed check in §3.3.2 which we believe includes the first quantitative test in practice of an ambipolar diffusion code with a non-isothermal energy equation. Our hope is that this test is applied for future codes developed with ambipolar diffusion.

3.3.1 Quasi-Static Collapse

This test involves matching qualitatively the characteristics (such as timescales and curve features) of a quasi-static collapse of a thermally critical but otherwise magnetically sub-critical, non-rotating core. This calculation was first performed by Fiedler & Mouschovias (1993). Its history as use for a test code for ambipolar diffusion is sporadic, appearing in Safier et al. (1997) (an analytical model) and more recently in SPH models by Hosking & Whitworth (2004b).

For comparison, we use the parameters of model 1 from Fiedler & Mouschovias (1993). These are presented in Table 3.2. The model we use is somewhat different than Fiedler & Mouschovias (1993), however it produces a thin quasi-static disk of the same characteristics. In this sense it is studying the same problem, the timescale between thin disk formation and dynamic collapse. The difference in models is due to the unique way in which the problem was initially setup in Fiedler & Mouschovias (1993), using a small cylinder (described below) with periodic boundary conditions on all surfaces (our setup in FLASH is cartesian). Our model consists of a sphere of uniform density and radius R_{test} in thermal equilibrium with an external medium of low density ($\rho_{\text{ambient}} = 0.1\rho_{\text{core}}$). The setup is shown schematically in Figure 3.2. The model of Fiedler & Mouschovias (1993) used a uniform cylinder of density ρ_{core}, radius R_{test} and height above the midplane $Z = R_{\text{test}}$, otherwise using the same parameters. Both have periodic boundary conditions, thus the former will have less of an ambient source of material in which to accrete due to a smaller box size. Also, our initial setup will collapse much quicker into the quasi-static state as it is highly unstable. The setup of Fiedler & Mouschovias (1993) is only slightly thermally critical to fragmentation.

The sphere quickly collapses along the field lines into a quasi-static disk (which matches the description of the *thin disk* model described in §2.3.1). The evolution of the central density is shown in Figure 3.3. The initial rise in density is due to the rebounding after the initial infall, as described by Fiedler & Mouschovias (1993). Gas

Table 3.2: The parameters used in the quasi-static collapse test run. Note that the ionization is that described in §2.1.1, with $\mu_{\rm mol} = 2.33$. The sound speed then corresponds to a temperature of 10 K. The box dimensions extend from -3.24 pc to $+3.24$ pc.

$R_{\rm test}$ [pc]	$n_{\rm in}$ [cm^{-3}]	$n_{\rm out}$ [cm^{-3}]	$b_{\rm test}$ [μG]	c_s [km s^{-1}]
0.75	300.0	30.0	30.0	1.889

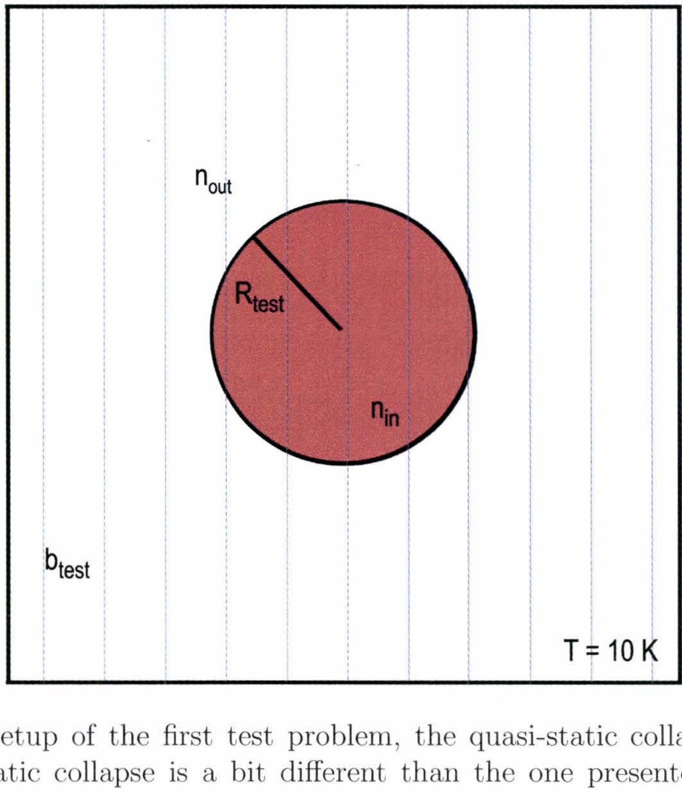

Figure 3.2: Setup of the first test problem, the quasi-static collapse. Our setup of the quasi-static collapse is a bit different than the one presented by Fiedler & Mouschovias (1993). The key parameters are shown. The whole box is kept at 10 K throughout the collapse.

piles into the disk while magnetic pressure is pushing it out. When the disk reaches the quasi-stable equilibrium—where gravitational forces are balanced by magnetic forces—the infalling gas takes a while to respond, continuing to accrete a bit more matter onto the disk. Magnetic pressure forces then drive out the excess matter and the disk settles into a quasi-equilibrium. Note that the cited authors reach this characteristic peak at 6 Myr, while we reach it at 2 Myr. The perfectly magnetized case will evolve only marginally after this, accreting material from the ambient medium. It is clear then that the non-ideal disk is accreting mass internally as well as from the ambient medium as its central density evolves at a higher rate than that of the ideal case.

Eventually, freefall occurs in the non-ideal model. Fiedler & Mouschovias (1993) have a freefall collapse that begins at about 16 Myr while ours begins at about 12 Myr. The discrepancy is solved by observing that each freefall state occurs 10 Myr after the rebounding "bump" occurs and the quasi-static disk is formed. In this sense our models agree on the timescale of ambipolar diffusion.

The evolution of the central magnetic field with density in Figure 3.3 gives a clearer agreement with Fiedler & Mouschovias (1993) as it is independent of time, and more a reflection of the physics at work. Our curve has the right qualitative features: a constant field followed by a positive power law. The power law begins at roughly $(2-4)\times 10^4$ in agreement with Fiedler & Mouschovias (1993).

We have correctly found the timescale of collapse described by Fiedler & Mouschovias (1993), matching all qualitative features of the quasi-static collapse. We conclude that we have passed this initial test.

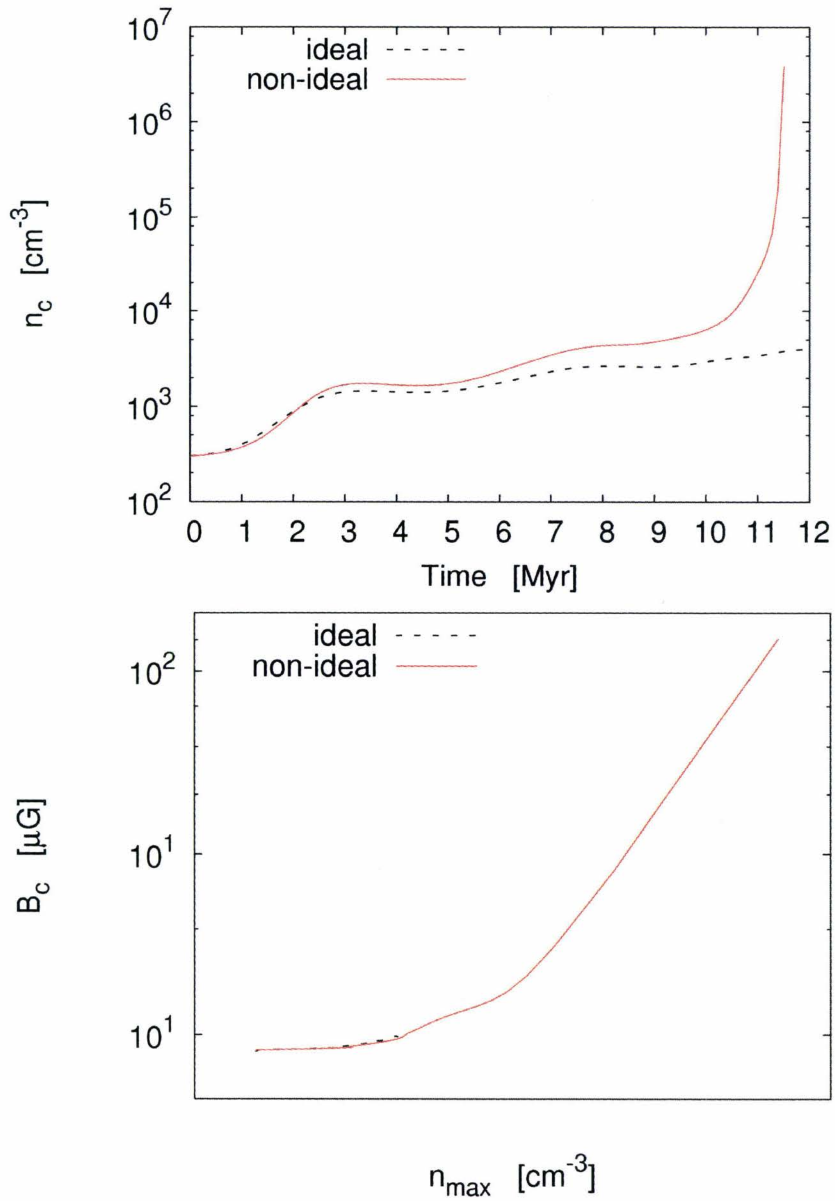

Figure 3.3: Results from the first test run showing the evolution density and magnetic field initiated from our quasi-static collapse setup. The central density evolution is shown above and the evolution of the central magnetic field is shown below. The ambipolar diffusion run is shown in the red (solid) line and the ideal run is shown in the black (dashed) line.

3.3.2 C-Shocks

We recall from §2.3.3 that C-shocks are continuous transitions of hydrodynamic variables mediated by ambipolar diffusion. Without ambipolar diffusion such flow transitions are very discontinuous and are classified as J-shocks. C-shocks have quickly become a common test case for ambipolar diffusion codes due to recent interest that has sprung up in a variety of subjects, particular turbulence models (see section §2.3.3 for a more physical discussion; Li et al., 2006; O'Sullivan & Downes, 2006; Falle, 2003; Mac Low & Smith, 1997; Smith & Mac Low, 1997; Mac Low et al., 1995). Tests for ambipolar diffusion, with a given analytic solution, are very hard to generate due to the complex nature of the equations. The C-shock has provided a very convenient test case for the papers mentioned, all of which are isothermal. As astrophysical problems generally involve shocks, we will eventually require non-isothermal simulations in which to better study them. A test for such simulations which includes the effects of drift heating and energy dissipation does not exist to our knowledge. However, further development of the idea of C-shocks can be expanded to include effects of having a proper treatment of energy evolution. We present the first such test of a non-isothermal ambipolar diffusion energy code that we are aware of in the literature, in the hopes it will be used as a standard test in the future. Alongside this we perform an isothermal C-shock test to independently test the induction equation.

Basic Setup

In Figure 3.4 the basic idea of a C-shock is illustrated in our initial setup, such that the field $\boldsymbol{B}$ is initially oblique to the normal of the shock front by an angle θ_s. The discontinuity will be transformed into a more continuous transition as the neutrals sift through the ions and feel the magnetic forces only through friction (see §2.3.3).

Table 3.3: The initial conditions for the C-shock test. The value of γ_{AD} is 1.0, and the ion density is kept constant at $\rho_i = 10^{-5}$ cm^{-3}. The temperature is adjusted to 10 K by setting the molecular mass appropriately, given that the sound speed is $c_s = 0.1$ cm s^{-1}. The initial field deflection is $\theta_s = \pi/4$ and $B_x = B_0 \cos(\theta_s) = \sqrt{4\pi} \cos(\theta_s)$ is a constant. Non-isothermal post-shock states are only slightly different than isothermal ones (save pressure).

	ρ_n [g cm^{-3}]	P_n [dyne cm^{-2}]	v_x [cm s^{-1}]	v_y [cm s^{-1}]	B_y [G]
left	1.000	0.0100	$v_s = 5.000$	0.000	2.507
right$_{\mathrm{iso}}$	8.045	0.0804	0.621	0.840	23.553
right$_{\mathrm{non-iso}}$	7.982	0.2246	0.626	0.836	23.463

The dimensionality of the problem is two, so we run the simulation in permutated orientations of x, y and z to fully test our code. However each run involves a 3D tube. The boundary conditions are inflow at the left x boundary and outflow at the right x boundary, while periodic conditions are used for every other boundary.

The C-shock analytical solutions are based on work from the 80's and 90's (Wardle, 1991a,b, 1990; Draine, 1986), where the first paper deals with the oblique shocks we present here. The equations presented therein offer a working analytical solution to a steady state, isothermal, two-fluid C-shock, mediated by ambipolar diffusion.

We have found some inconsistencies with the how the energy equation was reduced to give a differential equation for the pressure. This seems to have been the subject of contention in the past, despite a paper devoted to settling the theoretical impasse (Draine, 1986). We note that in addition to missing terms in the pressure relation, only drift heating is considered and not the redistribution of energy by ambipolar diffusion (see §2.1). We include the full effects of ambipolar diffusion on the energy equation, in addition to providing proper solutions to the problem outlined below. We keep the notation used in the papers mentioned for consistency.

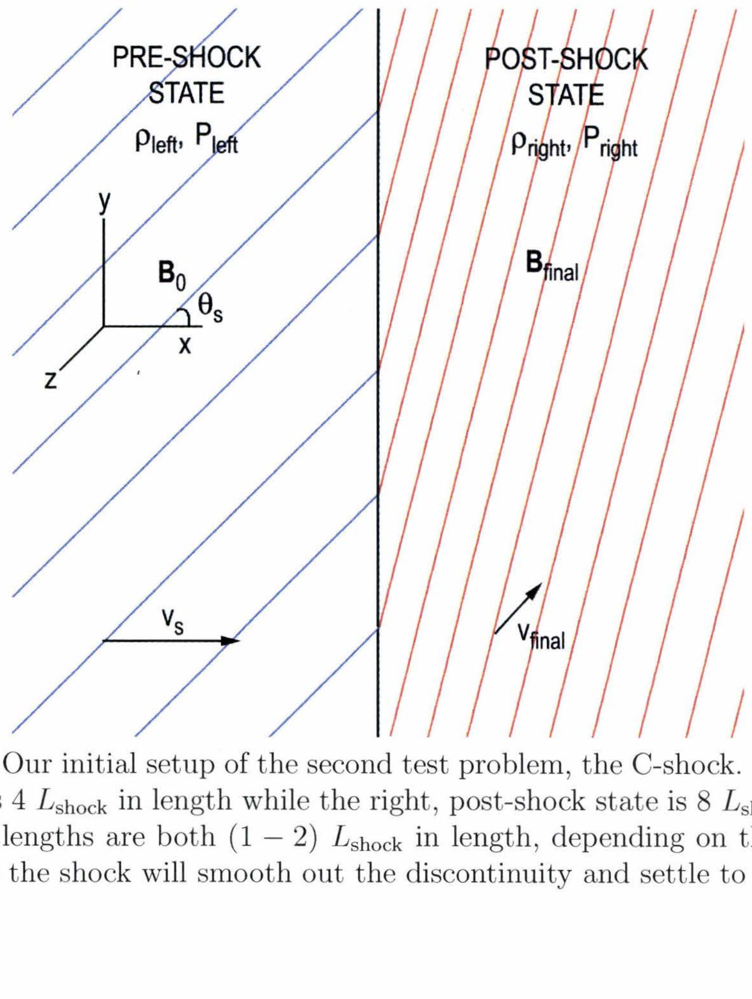

Figure 3.4: Our initial setup of the second test problem, the C-shock. The left, pre-shock state is 4 $L_{\rm shock}$ in length while the right, post-shock state is 8 $L_{\rm shock}$ in length. The y and z lengths are both $(1-2)$ $L_{\rm shock}$ in length, depending on the resolution. After a while the shock will smooth out the discontinuity and settle to form a stable C-shock.

Also note that since we use a single fluid code, we must make a choice on how to treat the ion density evolution. A simple choice would be to keep it constant ($\rho_i = \rho_{i_0}$). To account for this involves adjusting a term in the analytical solution, and we outline how this is done below (as well as how to change the equations to ion mass-conserving form).

We take the initial values of Mac Low et al. (1995) as their shocks show long transitions, indicating strong ambipolar diffusion. Running these through the analytic solutions we find the values of the post shock front. Our initial setup consists of a left state with these pre-shock values and a right state with the post-shock values (Figure 3.4 and Table 3.3). We evolve the shock tube and allow it to settle to its final configuration, which we compare to analytical values.

The analytic solutions we derived consist of a coupled set of two first order ordinary differential equations in parameters p and b. The equations are, given a steady shock as discussed above:

$$\left(\frac{1-\gamma r_n p}{(\gamma-1)r_n}\right)\frac{dp}{dz} = \frac{\gamma_{\mathrm{AD}}\rho_{i0}}{v_s}\left[\left(\frac{1}{r_n}+\frac{\gamma}{\gamma-1}p-\frac{s_n+\sin\theta_s}{b}\right)r+\frac{(G_n-\Lambda_n)}{\gamma_{\mathrm{AD}}\rho_{i0}\rho_{n0}v_s^2}\right] \quad (3.22)$$

$$\frac{db}{dz} = \frac{\gamma_{\mathrm{AD}}\rho_{i0}}{v_s}A^2\left(\frac{r}{b}\right), \quad (3.23)$$

where,

$$r_n = \frac{1}{1-(p-p_0)-\left(\frac{b^2-b_0^2}{2A^2}\right)} \quad (3.24)$$

$$r = \left(1-\frac{r_n}{r_i}\right) \quad (3.25)$$

$$r_i = r_n \left(\frac{b^2 + \cos^2 \theta_s}{b r_n (s_n + \sin \theta_s) + \cos \theta_s{}^2} \right) \tag{3.26}$$

$$s_n = \frac{b - b_0}{A^2} \cos^2 \theta_s, \tag{3.27}$$

and γ is the adiabatic index of the neutral gas, $\gamma_{\rm AD}$ is the collisional constant between ions and neutrals described in §2.1, ρ_{n_0} and ρ_{i_0} are the initial density states of the ions and neutrals respectively, v_s is the initial speed of the gas towards the shock, $A = v_s/v_A$ is the Alfvén number of the initial state and $v_A = B_0/\sqrt{4\pi\rho_{n_0}}$ is the Alfvén velocity. The velocity compression of the neutral and ionized gases are described by the parameters $r_i = v_s/v_{i_x}$ and $r_n = v_s/v_{n_x}$. The dimensionless pressure is $p = P_n/\left(\rho_{n_0} v_s^2\right)$, and the dimensionless field (in the y-direction) is $b = B_y/B_0$, where B_0 is the total initial field magnitude. The deflection of the field is quantified by $s_n = \left(v_{n_y} B_x\right) / \left(v_s B_0\right)$, as the deflected field will accelerate a velocity in the y direction as it moves through the gas. The x-component of the field stays constant due to the symmetry in the problem, and in our runs the ionization is kept constant (though its velocity shocks strongly). The parameter r defines what type of chemistry is used or if ion mass is simply conserved. The value given above is for a constant ion density. For ion mass conservation (as in Wardle (1991a)) the value is $r = (r_i - r_n)$. For a general chemistry, $r = f(x)\left(1 - r_n/r_i\right)$ (such that one can derive $\rho_i = f(x)\rho_{i_0}$, where $f(x)$ is some function in the x direction which may include variables such as r_n).

Drift heating is governed by the parameter:

$$\begin{aligned} G_n &= \gamma_{\rm AD} \rho_i \rho_n \parallel \boldsymbol{v}_n - \boldsymbol{v}_i \parallel^2 = \mu_0 \beta_{\rm AD} \parallel \boldsymbol{J} \times \boldsymbol{B} \parallel^2 \\ &= \gamma_{\rm AD} \rho_{n_0} \rho_{i_0} v_s^2 \frac{r^2}{b^2 r_n} \left(b^2 + \cos \theta_s{}^2\right), \end{aligned} \tag{3.28}$$

and Λ_n is the cooling rate. The analytical solutions prove to be rather difficult to solve without cooling (via a simple Runge-Kutta 4 technique). By including a cooling rate as done in Wardle (1991a), solutions can be obtained that are significantly different than un-heated shocks yet realistically integratable. We take a simplified cooling rate that approximates those of Lepp & Shull (1983), relevant to molecular clouds:

$$\Lambda_n = \begin{cases} \Lambda_{n_0}[(\gamma_{\mathrm{AD}}\rho_{i_0})/(p_0^3 v_s)]p^3 \text{ [erg s}^{-1}] & (p > p_0) \\ 0 & \text{(otherwise)}, \end{cases} \tag{3.29}$$

where p_0 is the initial dimensionless pressure and Λ_{n_0} is a fudge factor. We found $\Lambda_{n_0} = 5 \times 10^{-5}$ provides good analytical graphs at a reasonable computational cost.

The lengthscale of the shock is given as $L_{\mathrm{shock}} = \sqrt{2}v_A t_{\mathrm{flow}}$, where $t_{\mathrm{flow}} = 1/(\gamma_{\mathrm{AD}}\rho_{i_0})$ is the timescale for the shock. We use these parameters in our simulation setup, having a box 12 × (1-2) × (1-2) L_{shock} in dimensions (depending on resolution), and printing plot files every 0.1 t_{flow} (for a total of 300 files). The evolution consists of a large outward propagating density enhancement which is ejected from the box as the flow settles to form a C-shock. Note that while this density wave is in the box timesteps are smaller, by about an order of magnitude. Because of this, a longer box means longer computation times.

Note that our solution for the pressure derivative in equation (3.22) is significantly different than that derived in Draine (1986) and used in Wardle (1991a). Even without our addition of energy dissipation we find a different equation[4]. We compare our solution to that of Wardle (1991a) in Figure 3.5 for an adiabatic index of $\gamma = 1.1$ and using the values presented in Table 3.3. The significant difference between the results is quickly apparent. See typical isothermal values of pressure in Table (3.3) to understand the scope of the numbers in this figure. Other quantities have only minor

[4]Note that while Draine (1986) has used physical arguments to explain away magnetic terms in the energy equation, our derivation follows mathematically from first principles. This may be a source of error. This discrepancy will not affect the isothermal solution, thus it's widespread success in testing other codes.

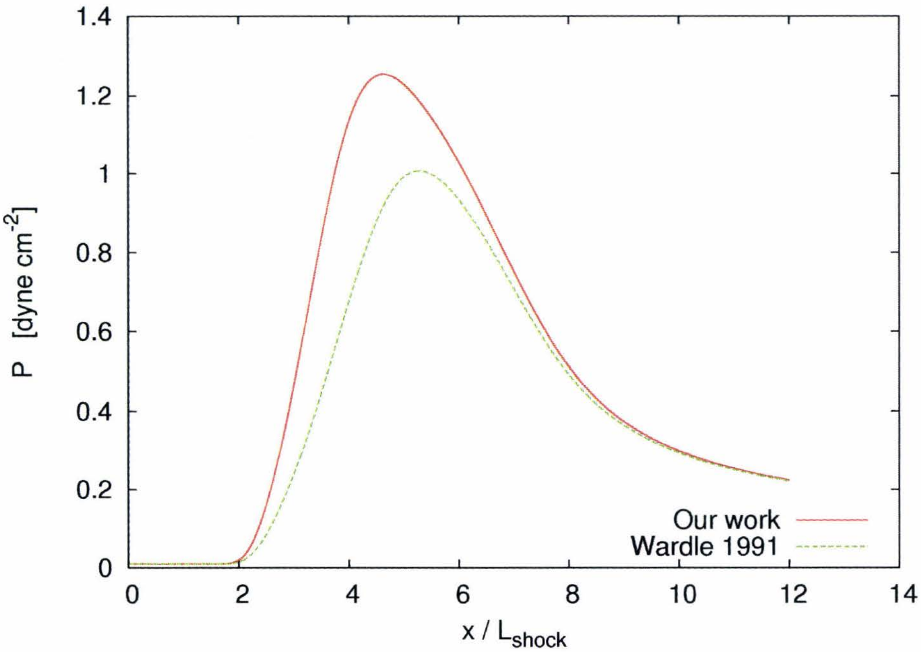

Figure 3.5: Pressure profiles comparing our analytic solution to that of Draine (1986) and Wardle (1991a). A significant difference is apparent.

differences.

Numerical Results

In the following subsection we present comparisons of isothermal and non-isothermal C-shock simulations relative to analytical solutions. The error is calculated as in Mac Low et al. (1995):

$$\% \text{ error} = 100 \left| \frac{q_{\text{analytic}} - q_{\text{numerical}}}{\max\left(q_{\text{analytic}}\right)} \right|. \tag{3.30}$$

We employ very poor resolutions in simulations; our low resolution has cell sizes of (1/2) L_{shock} while our 'high' resolution run resolves (1/4) L_{shock} (though in 3D). This is enough to show the high accuracy of our models (giving similar errors to that of Mac Low et al. (1995) with half the resolution) and demonstrate a clear convergence, thus confirming our implementation of the induction equation. Our results are in

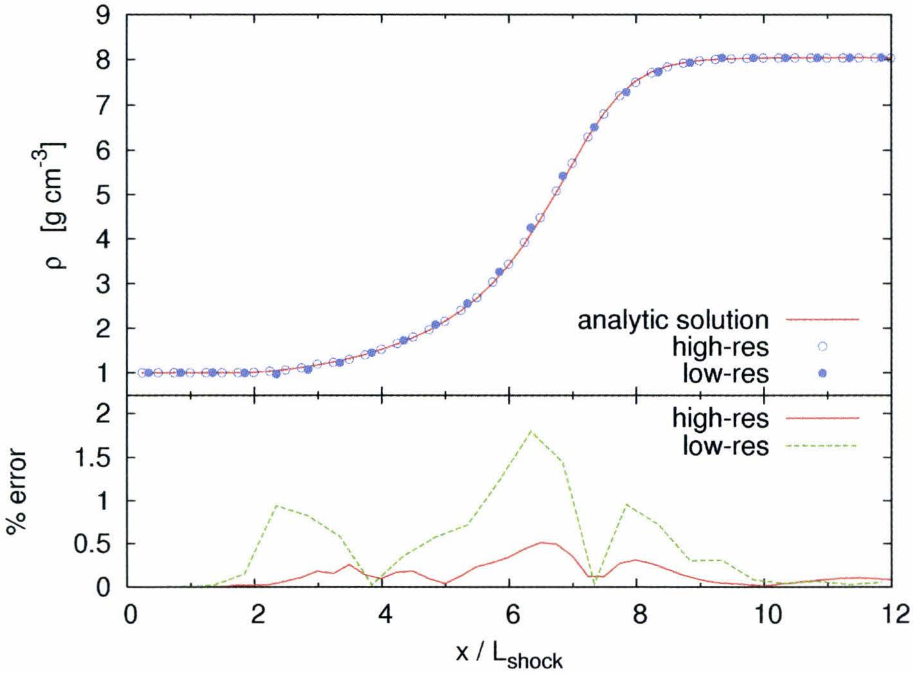

Figure 3.6: Density profiles comparing simulations of isothermal C-shocks with analytical solutions at different resolutions. Accuracy is high and convergence is evident. Pressure distributions are identical (though scaled) for the isothermal case.

Figures (3.6)-(3.9). Recall that we are using very poor resolutions in these tests.

Finally we present the results of the non-isothermal run, testing our energy terms. For these simulations we use an adiabatic index of $\gamma = 1.1$. These simulations also show high accuracy and a clear convergence (the right end of the box is explained below). Our results are seen in Figures (3.10)-(3.14).

We note that the shocked pressure structure is very long, and would be inefficient to encapsulate in a much larger simulation box. We maintain the same box size, but only attain a partially stable, non-isothermal C-shock. It is seen to slowly push out of the right boundary (the isothermal C-shock is stable). For this reason shocked values beyond the discontinuity at 5 $L_{\rm shock}$ do not fully attain the correct values. This explains the large tail of increasing errors which do not show convergence. Right state

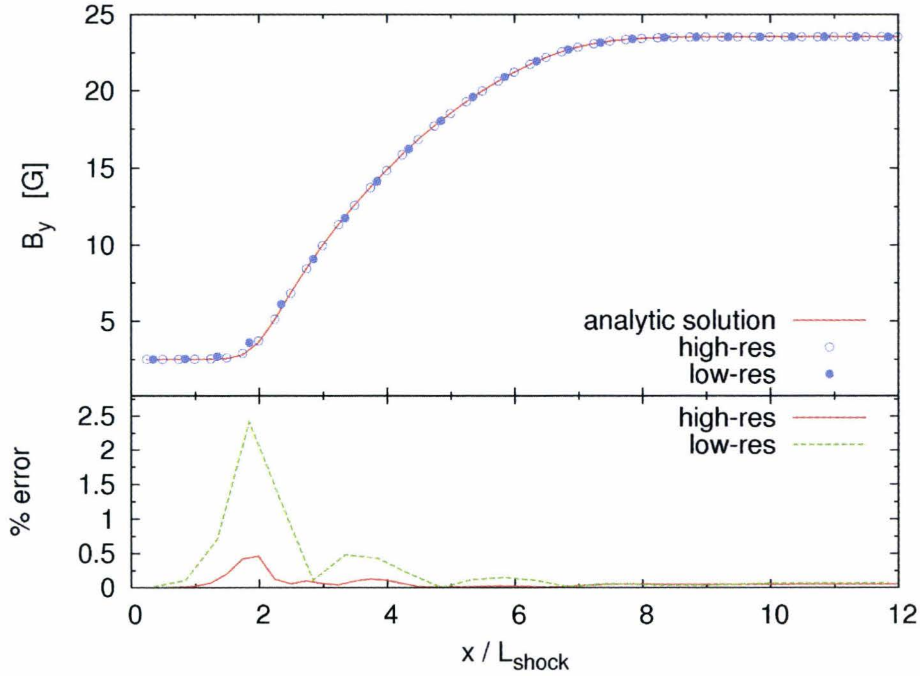

Figure 3.7: Magnetic field profiles comparing simulations of isothermal C-shocks with analytical solutions at different resolutions.

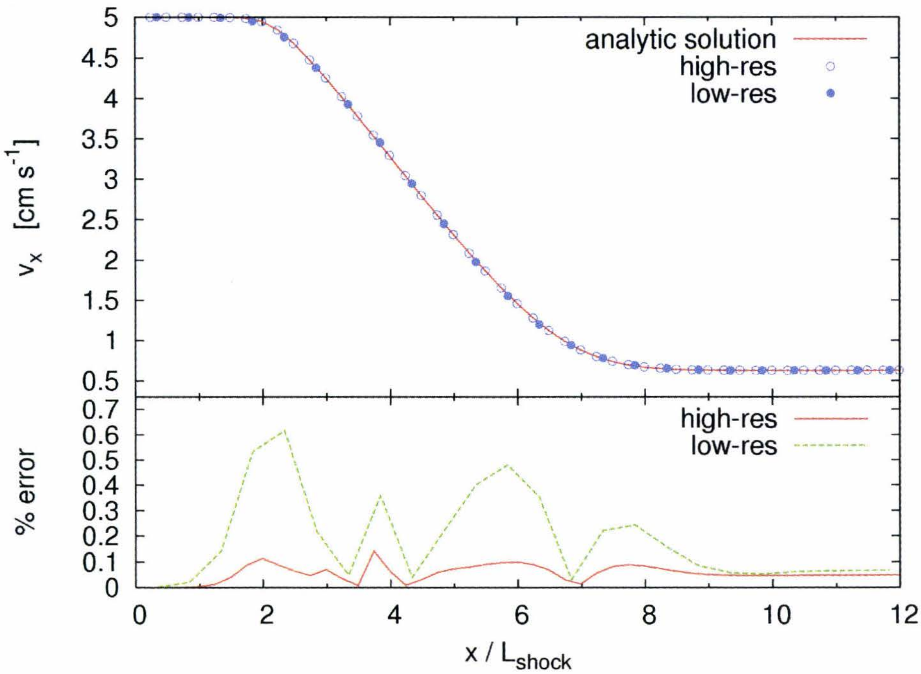

Figure 3.8: X-component velocity profiles, comparing simulations of isothermal C-shocks with analytical solutions at different resolutions.

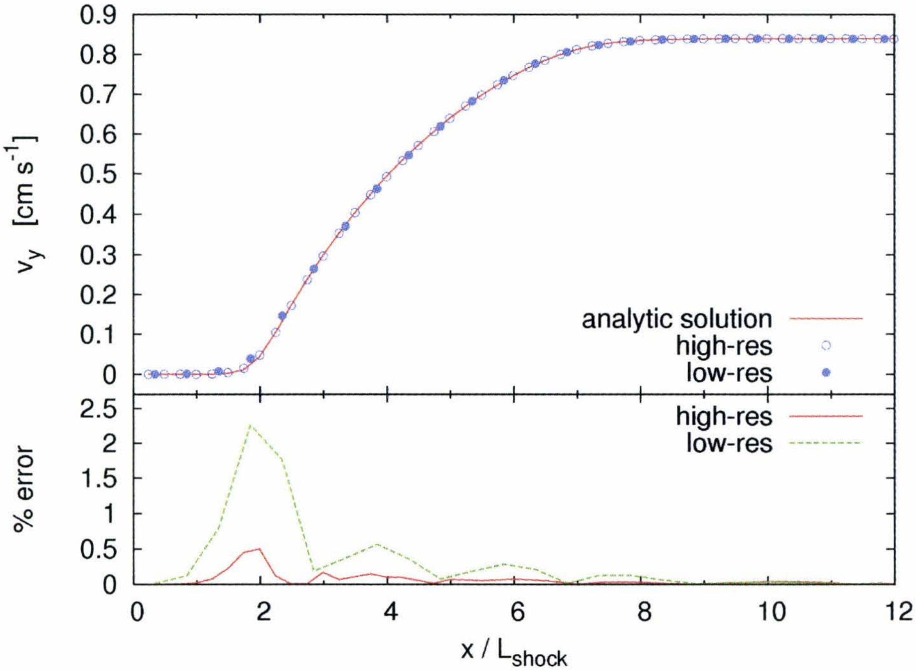

Figure 3.9: Y-component velocity profiles, comparing simulations of isothermal C-shocks with analytical solutions at different resolutions.

values are seen to generally decrease with flow time. To emphasize this we show in Figure (3.15) two different fits for the density at the same resolution, but for different times when the shock appears established (the simulations are both translated to a 'best-fit' position on the graph, in reality the later curve is displaced from the earlier curve towards the right boundary). This shows how error increases with time in the post-shock region due to our not correctly encapsulating the pressure shock.

Further work needs to be done on this test to perfect it for quick testing procedures. However, it is clear from the above tests that our code performs admirably in all facets.

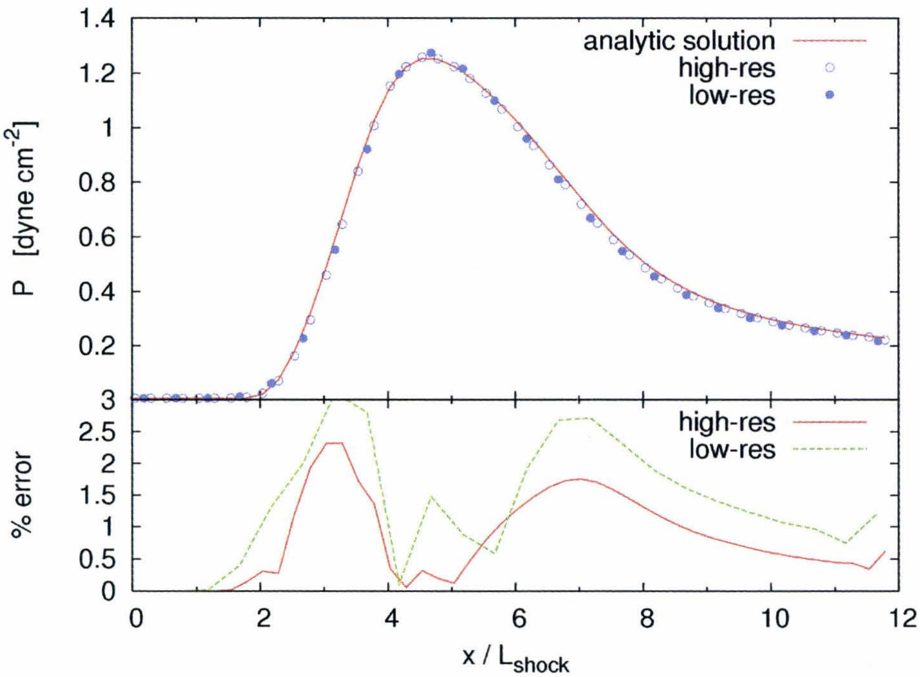

Figure 3.10: Pressure profiles comparing simulations of non-isothermal C-shocks with analytical solutions at different resolutions. Accuracy is high and convergence is evident. Temperature distributions are similar (though scaled).

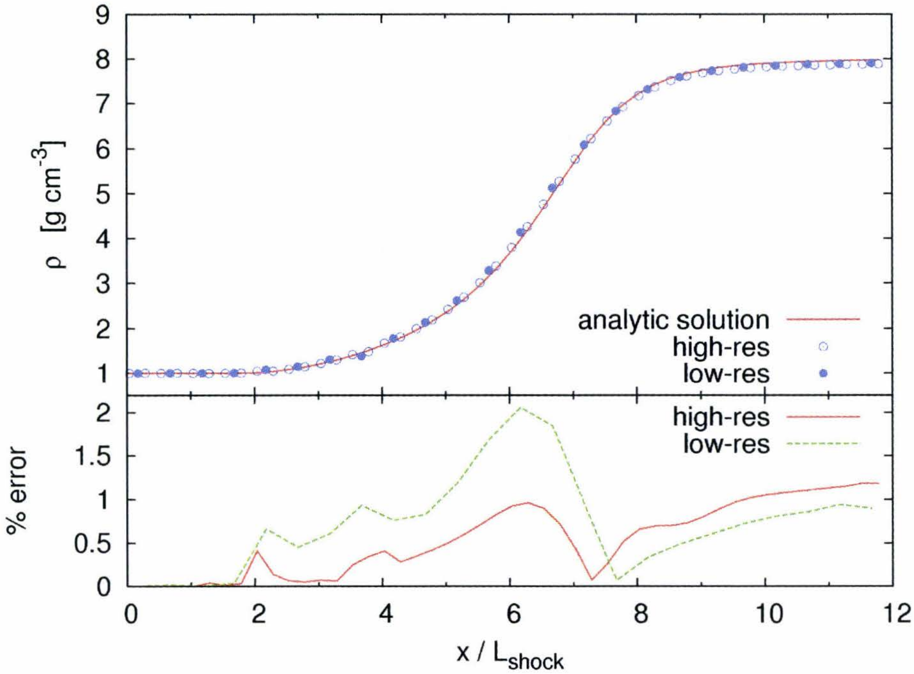

Figure 3.11: Density profiles comparing simulations of non-isothermal C-shocks with analytical solutions at different resolutions.

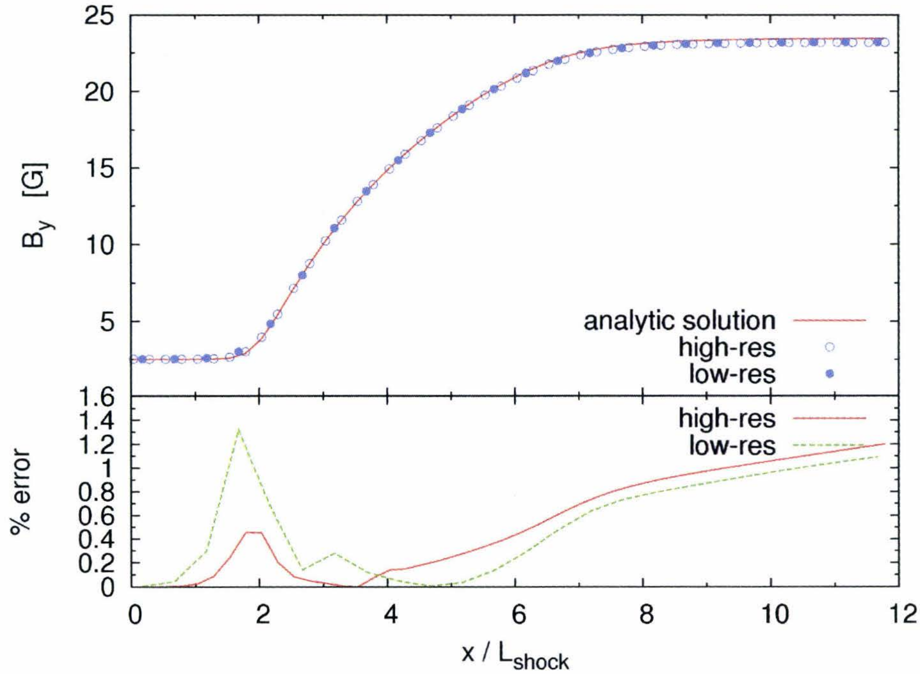

Figure 3.12: Magnetic field profiles comparing simulations of non-isothermal C-shocks with analytical solutions at different resolutions.

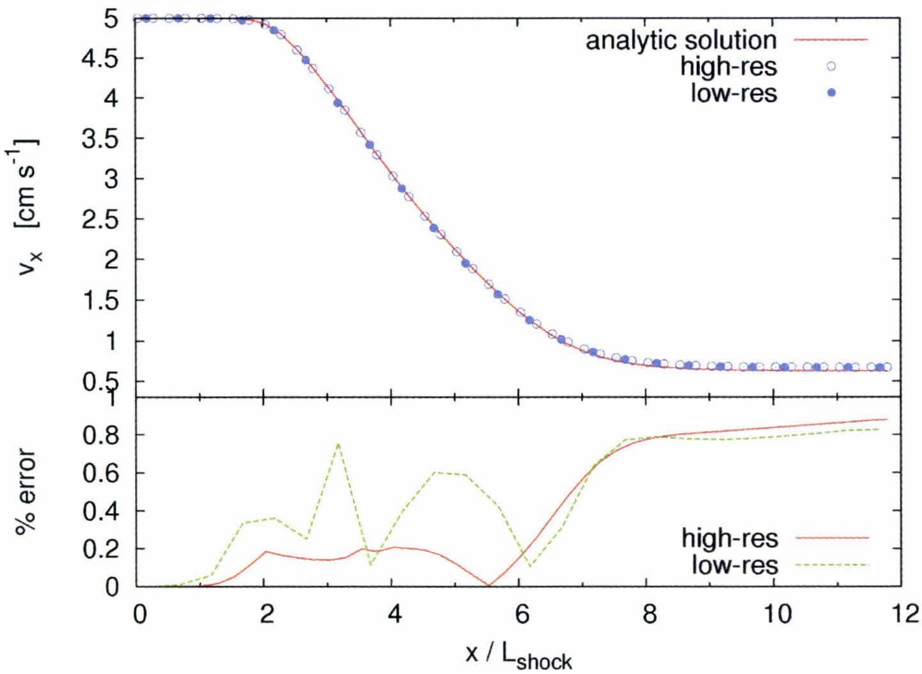

Figure 3.13: X-Component velocity profiles, comparing simulations of non-isothermal C-shocks with analytical solutions at different resolutions.

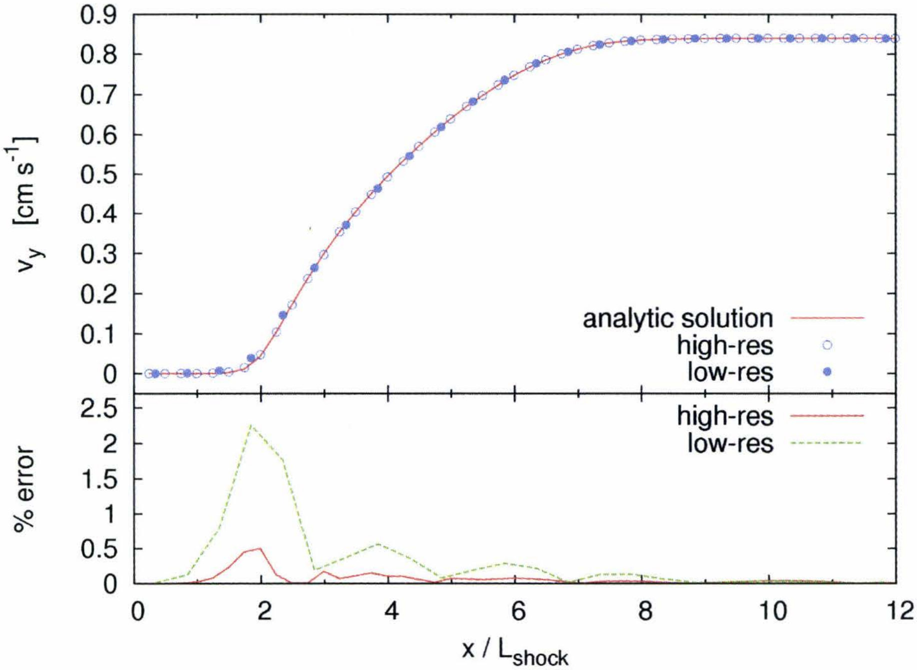

Figure 3.14: Y-Component velocity profiles, comparing simulations of non-isothermal C-shocks with analytical solutions at different resolutions.

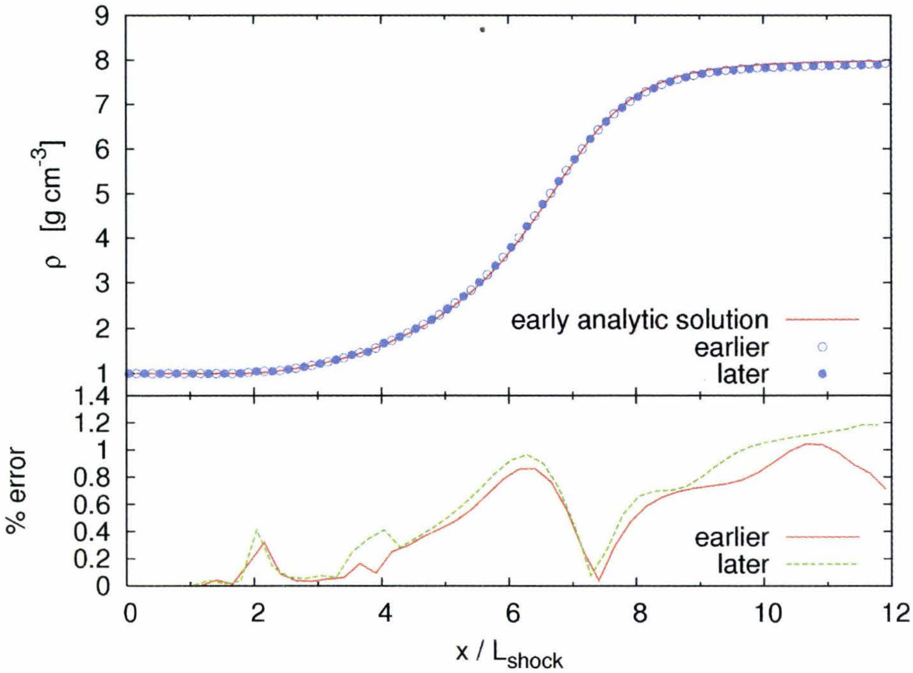

Figure 3.15: Density profiles at similar resolutions, but different times in the non-isothermal C-shock test.

Chapter 4

Results: The Collapse of Magnetized, Rotating Bonnor-Ebert Spheres with Ambipolar Diffusion

4.1 Introduction

Over the past decade numerical simulations have revealed a variety of very important physical processes at play during the collapse of a molecular cloud core from realistic initial conditions. These processes help us understand the key issues associated with the evolution of a pre-Class 0 object, such as how rotation is effectively lost through magnetic braking, how multiple stars form through fragmentation, why outflows and jets begin so early and how all these effects help drive very high accretion able to overcome radiation pressure from a massive internal protostar. The introduction of magnetic fields into these models has been a necessary physical ingredient in most phenomena, or else having a significant effect on others. In most computations to date, however, the magnetic field is coupled perfectly with the gas as a whole, where in fact real molecular clouds have only a small fraction of charged species. In dense star forming regions ions and electrons have abundances on the order of $\chi \approx 10^{-7}$, where χ represents the number of ions per H atom (including those in molecular H_2). Realistic conditions provide only partial magnetic support to most of the gas, allowing neutral components to sift through their coupled counterparts at the cost of collisional friction.

This physical process is called ambipolar diffusion and has been studied in a large variety of astrophysical contexts very much relevant to star formation, since the work of Mestel & Spitzer (1956). In this early study, a cloud of gas gradually loses magnetic support through the straightening of its field lines. Numerical simulations which stemmed from this idea suggested clouds form in magnetically supported environments and require ambipolar diffusion as a mechanism in which to lose this support and collapse (Tassis & Mouschovias, 2007b; Ciolek & Basu, 2006; Desch & Mouschovias, 2001; Basu & Mouschovias, 1994; Fiedler & Mouschovias, 1993), despite long formation timescales of (10-20) Myr in contrast with observations. Sharply discontinuous shocks were seen to become more continuous transitions (C-shocks) under the addition of ambipolar diffusion and susceptible to a unique instability (Mac Low & Smith, 1997; Smith & Mac Low, 1997; Mac Low et al., 1995; Wardle, 1991a,b, 1990; Draine, 1986). Ambipolar diffusion has also been seen as important in damping the magnetorotational instability (MRI; Kunz & Balbus, 2004), in the fragmentation of cloud cores during collapse (Hosking & Whitworth, 2004a) and even in turbulence models of molecular clouds (O'Sullivan & Downes, 2006; Zweibel, 2002). These studies formed an early basis for numerical techniques using ambipolar diffusion, from which point we proceed.

Many authors have studied the collapse of supercritical clouds both analytically (Hunter, 1977; Larson, 1969; Penston, 1969) and through numerical simulations involving increasingly complex physics and multiple dimensions (Machida et al., 2007; Banerjee & Pudritz, 2006; Banerjee et al., 2004; Foster & Chevalier, 1993). In these collapses it was revealed that magnetic fields in combination with rotation help drive early rotating disk-winds during the collapse phase. Rotating disks wind up a toroidal magnetic field which then acts to torque down the disk. In turn, magnetic field lines attached to the ambient, non-rotating medium are wound up, extracting angular momentum from the rotating cloud through a process called magnetic braking.

The effects of braking are important when one considers the fragmentation of a collapsing cloud during these early stages. Simulations have shown ambipolar diffusion reduces this effect and allows more fragmentation to occur (Hosking & Whitworth, 2004a). Effects of magnetic pressure have been shown to have a more prominent role in the fragmentation process by stabilizing the collapsing disk against instabilities (Price & Bate, 2007; Banerjee & Pudritz, 2006). The role of ambipolar diffusion may be understood to decrease the effects of pressure by suppressing the overall build-up of the magnetic field. Large fossil fields of 1 kG have been recently observed in the core of the protostellar accretion disk FU Orionis (Donati et al., 2005), in agreement with results from ideal MHD collapse simulations of (Banerjee & Pudritz, 2006). From this, we don't expect magnetic field build-up to be significantly affected by ambipolar diffusion. Rather, while the magnetic field distribution is certainly smaller, we argue in §4.3.1 that ambipolar diffusion allows for a diminished effective magnetic support, which in turn leads to a greater tendency for instabilities to form in the disk. This drives higher rates of fragmentation.

By extracting angular momentum it is found that magnetic fields are responsible for high accretion rates of around 10^{-3} $M_\odot$ yr^{-1} during the pre-Class 0 collapse. As massive protostars are likely to begin nuclear burning while accreting, radiation pressure may play a role in limiting their final mass. Axisymmetric numerical simulations have shown that slowly rotating, non-magnetic molecular clouds can form to at most 42.3 $M_\odot$ in face of radiation pressure from even the most massive cloud cores (Yorke & Sonnhalter, 2002). Accretion rates found in Banerjee et al. (2006) are strong enough to overcome radiation pressure from a newly formed massive protostar. In addition, outflows carve out magnetically supported bubbles as they advance from the disk. These bubbles provide avenues of escape for the radiation from a massive protostar, allowing the star to obtain very large masses through gravitational collapse (simulations currently obtain $M > 40$ $M_\odot$, but continue to accrete in a stable configuration; Krumholz et al., 2005). If magnetic fields regulate the creation of these outflow cavities, it becomes important to understand how a realistic treatment of collapse with non-ideal magnetic coupling affects if and when these early outflows occur. We will show in §4.3.4 that, surprisingly, outflows start even earlier if ambipolar diffusion is included.

Ultimately, the driver of angular momentum transport, in which toroidal magnetic fields are wound up and outflows are launched, is the pseudodisk which forms early on in the collapse. This disk is generally non-Keplerian and is held up by a combination of thermal, rotational and magnetic supports. The size of the disk is commonly defined by the presence of a sharp shock at a scale of $(20 - 100)$ AU, wherein the size depends on the cooling model used in the numerical simulation (Banerjee & Pudritz, 2006; Banerjee et al., 2004). It is also the region in the collapse where ambipolar diffusion is the strongest; ionization fractions decrease with increasing density at a rate dependent on the chemistry used and the ionization sources considered. Unable to cool efficiently and remain isothermal, the disk should experience a significant amount of frictional drift heating. We show that this leads to a 'puffy' disk in §4.3.3.

Furthermore, the surface layers of the disk will be more coupled to the field than the midplane under realistic ionization conditions. We call the effectively decoupled disk midplane a *decoupled zone* and provide a quantitative measure of its extent in §4.3.5. This will drive higher accretion rates along surface layers through increased transport of angular momentum. This leads to a sort of precursor to the idea of layered accretion in a Keplerian accretion disk, as introduced by Gammie (1996). Coupled disk layers will furthermore drag in field lines with respect to the decoupled midplane. This differs significantly from the ideal picture where the midplane is seen to drive magnetic field build-up, producing a 'pinched-in' field structure towards the center of the cloud and along the disk midplane (Machida et al., 2007; Banerjee & Pudritz, 2006).

Finally, MRI turbulence in an ambipolar diffusion dominated disk has been shown to be significantly damped if the rotational timescale, Ω^{-1}, is shorter than the timescale of neutral-ion collisions, $\tau_{ni} = 1/\gamma_{\rm AD}\rho_i$ (Kunz & Balbus, 2004), where Ω is the rotational frequency, ρ_i is the ion density and $\gamma_{\rm AD} = 3.28 \times 10^{13}$ g^{-1} cm^3 s^{-1} represents the collisional coupling of the ions to the neutrals. A question we pose is whether or not a sort of proto-dead zone can form early on in the disk midplane, where MRI turbulence is significantly damped due to the lack of coupling of the field to the gas. Do we provide the initial conditions of dead zones during the initial collapse?

It is very important to elucidate the initial conditions a dead zone may have, as it has been shown to have important consequences in planet formation models treating migration (Matsumura & Pudritz, 2005), helping to determine final planet masses and to stop planets from entering their parent star. Such a dead zone would be different as it is governed by ambipolar diffusion rather than Ohmic dissipation, which will be important at only the highest densities considered in pre-Class 0 collapse (Desch & Mouschovias, 2001). We will discuss this further with the aid of our results in §4.3.5.

4.2 Numerical Methods

To perform numerical studies of the physical questions raised in §4.1 we use FLASH2.5 (Fryxell et al., 2000). FLASH provides us the ability to compute magnetohydrodynamics (MHD) in three dimensions while employing adaptive mesh refinement (AMR). Its computational scheme, based on the *8-wave* Riemann solver of Powell et al. (1999) with the addition of a simple yet effective diffusive $\nabla \cdot \boldsymbol{B}$ cleaning technique, allows very accurate capturing of shocks.

We build on previous studies of collapsing molecular clouds (Banerjee & Pudritz, 2007; Banerjee et al., 2006; Banerjee & Pudritz, 2006; Banerjee et al., 2004) from which the details of the cooling modules used can be found. Additions to the FLASH code include resolving the Jeans length ($\lambda_J = \left(\frac{\pi c_s^2}{G\rho}\right)$) by a variable number of grid cells in accordance with the Truelove criterion (Truelove et al., 1997, our runs use 8 or 24 cells per λ_J) and various cooling effects. The cooling effects include cooling due to collisional excitation of molecules such as H_2, H, O, CO, O_2, HCl, C and O (Neufeld & Kaufman, 1993; Neufeld et al., 1995; Banerjee et al., 2004), as well as dust-gas interactions (Banerjee et al., 2006) along with H_2 dissociation at high temperatures (and corresponding formation) and a radiative diffusion approximation in the optically thick regime.

This provides a more realistic method in which to account for the sudden changes in the equation of state of a collapsing cloud core, when cooling becomes inefficient. Many authors use a variable equation of state which jumps from isothermal to adiabatic (or something similar) at a given density (Tassis & Mouschovias, 2007a; Machida et al., 2006). The latter technique forbids the analysis of special energetic effects like drift heating, shocks or energy diffusion, by eliminating the energy equation for that of a polytropic equation of state.

4.2.1 Initial Conditions

Our initial conditions are those of a critical Bonnor-Ebert sphere in pressure equilibrium with a warm, low density environment. The details of our setup can be found in Banerjee et al. (2004). The sphere is given a small spin such that $\Omega t_{\rm ff} > 0.2$ (the freefall time is $t_{\rm ff} = (3\pi/32G\rho_0)^{1/2}$, where ρ_0 is the central density.), which has been shown to be a supercritical value for fragmentation in hydrodynamic collapses (Matsumoto & Hanawa, 2003).

We simulate the collapse of our low mass model of $M = 2.1\ M_\odot$ (which follows characteristics of the observed Bonnor-Ebert sphere Barnard 68 Alves et al., 2001) and a high mass model of $M = 168\ M_\odot$ (which follows characteristics of observations made on massive disks Chini et al., 2004). The former model has been used in the study of early outflow formation in (Banerjee & Pudritz, 2006), while the latter has been used in comparing ideally coupled to purely hydrodynamic and purely isothermal collapses, producing high accretion rates in all cases (Banerjee & Pudritz, 2007). We further this study in comparing the effects of a more realistic coupling through the implementation of ambipolar diffusion. The model details are outlined in Table 4.1.

Magnetic fields are introduced such that the plasma beta, $\beta = P/(B^2/4\pi)$, is

Table 4.1: The parameters for our collapse runs. Note that the high-mass model for our non-ideal run is given $\frac{3}{4}$ the rotation of the ideal run, so $\Omega_{\text{HM, AD}} = 8.265 \times 10^{-15}$ s^{-1}.

model	ρ_0 [g cm^{-3}]	c_s [km s^{-1}]	$c_{s_{\text{ext}}}$ [km s^{-1}]	β	B_{max} [μG]	Ω [s^{-1}]
high-mass	3.35×10^{-21}	0.408	1.289	76.0	1.36	1.10×10^{-14}
low-mass	9.81×10^{-19}	2.458	7.774	84.0	14.0	1.89×10^{-13}

constant and magnetic support does not prevent the cloud from collapsing. The field is initially aligned with the rotation axis. This follows work by Machida et al. (2006) which suggests oblique field components brake quickly in an ideal collapse, provided $\Omega > \Omega_{\text{crit}} = 0.39 B_0 G^{1/2} c_s^{-1}$, where Ω is the rotational frequency, B_0 is the initial field and c_s the isothermal sound speed. If the rotation is not strong enough, an oblique field will dominate, maintained by MRI. We note that our parameters are borderline to satisfying the condition of an aligned field (this allows us to better study outflows and other magnetic effects, yet maintain justification for an aligned field).

We use the low mass model of B68 more as a study of fragmentation and outflow generation and have given ideal and non-ideal models the same initial rotation of $\Omega t_{\text{ff}} = 0.4$. The high mass model is used more to study the characteristics of collapse, and so we adjust the rotation parameters such that the ideal model has $\Omega t_{\text{ff}} = 0.4$, the non-ideal model has $\Omega t_{\text{ff}} = 0.3$, and a corresponding hydrodynamic collapse has $\Omega t_{\text{ff}} = 0.2$, to correct for the effects of magnetic braking.

We use periodic boundary conditions on a box that is more than an order of magnitude larger than the radius of the initial B-E sphere.

4.2.2 Magnetohydrodynamic Equations with Ambipolar Diffusion

We use a single fluid approximation for our implementation of ambipolar diffusion in this initial study. The gain is a reduction in the effective number of fluids in the problem to one. Molecular clouds have small ionization rates such that $\rho_i \ll \rho_n$, where the subscripts i and n indicate properties of ions and neutral species respectively. More accurately, we approximate the ion density as((Hosking & Whitworth, 2004b; Fiedler & Mouschovias, 1993)):

$$n_i = K\left(\frac{n_n}{10^5\ \mathrm{cm}^{-3}}\right)^k + K'\left(\frac{n_n}{10^3\ \mathrm{cm}^{-3}}\right)^{-2}, \tag{4.1}$$

where n is a number density, $K = 3 \times 10^{-3}\ \mathrm{cm}^{-3}$, $k = \frac{1}{2}$ and $K' = 4.64 \times 10^{-4}\ \mathrm{cm}^{-3}$. The second term dies off quickly in the higher density regime, at which point we're left with the common $n_i \propto n_n^{1/2}$. The relation (4.1) comes from approximating the results of ionization equilibrium calculations (Elmegreen, 1979; Nakano, 1979) where the sole form of ionization is through cosmic rays (the cited authors assume a cosmic ray ionization rate of $\zeta_0 = 6.9 \times 10^{-17}\ \mathrm{s}^{-1}$).

This approximation can be used to eliminate the magnetohydrodynamic equations of the ions (see appendix A in Patel & Pudritz (1994) or Chapter 2 for a derivation of the isothermal equations and non-isothermal equations respectively) and provide an equation for the drift velocity $\boldsymbol{u}_d$ between the two species:

$$\boldsymbol{u}_d \equiv \boldsymbol{u}_i - \boldsymbol{u}_n = \beta_{\mathrm{AD}}(\boldsymbol{\nabla} \times \boldsymbol{B}) \times \boldsymbol{B}, \tag{4.2}$$

where $\boldsymbol{u}$ is a velocity, $\boldsymbol{B}$ is the magnetic field and $\beta_{\mathrm{AD}} = \frac{1}{\mu_0 \gamma_{\mathrm{AD}} \rho_i \rho_n}$. The constant $\gamma_{\mathrm{AD}} = \frac{<\sigma\omega>_{ni}}{m_i + m_n} = 3.28 \times 10^{13}\ \mathrm{g}^{-1}\ \mathrm{cm}^3\ \mathrm{s}^{-1}$ represents the coupling of the neutrals and ions. Ions are considered to be typically HCO^+ or Na^+ which have similar masses (about 29.0 a.m.u.) and collision rates with H_2 ($< \sigma\nu >_{\mathrm{ni}} = 1.7 \times 10^{-9}$ cm^{-3} s^{-1} (McDaniel & Mason, 1973)).

We can derive a set of MHD equations for the neutrals, consisting of frictional interaction with the ions, plus some extra ambipolar diffusion terms:

$$\frac{\partial \rho}{\partial t} + \boldsymbol{\nabla} \cdot (\rho \boldsymbol{u}) = 0 \tag{4.3}$$

$$\frac{\partial (\rho \boldsymbol{u})}{\partial t} + \boldsymbol{\nabla} \cdot \left(\rho \boldsymbol{u}\boldsymbol{u} + P + \frac{B^2}{2\mu_0} - \frac{1}{\mu_0}\boldsymbol{B}\boldsymbol{B} \right) = -\rho \boldsymbol{g} - \frac{1}{\mu_0}\boldsymbol{B}\left(\boldsymbol{\nabla} \cdot \boldsymbol{B}\right) \tag{4.4}$$

$$\begin{aligned} &\frac{\partial E}{\partial t} + \boldsymbol{\nabla} \cdot \left[\boldsymbol{u} \left(E + P + \frac{B^2}{2\mu_0} \right) + \frac{1}{\mu_0} (\boldsymbol{u} \cdot \boldsymbol{B})\, \boldsymbol{B} \right] + \boldsymbol{\nabla} \cdot \left[\beta_{\mathrm{AD}} B^2 \left(\boldsymbol{J} \times \boldsymbol{B} \right) \right] \\ &\quad = \rho \boldsymbol{g} \cdot \boldsymbol{u} - \frac{1}{\mu_0} \left(\boldsymbol{u} \cdot \boldsymbol{B} \right) \left(\boldsymbol{\nabla} \cdot \boldsymbol{B} \right) + \mu_0 \beta_{\mathrm{AD}} \, \| \boldsymbol{J} \times \boldsymbol{B} \|^2 \\ &\quad - \beta_{\mathrm{AD}} \left[\boldsymbol{B} \cdot (\boldsymbol{J} \times \boldsymbol{B}) \right] \left(\boldsymbol{\nabla} \cdot \boldsymbol{B} \right) \end{aligned} \tag{4.5}$$

$$\begin{aligned} &\frac{\partial \boldsymbol{B}}{\partial t} + \boldsymbol{\nabla} \cdot (\boldsymbol{u}\boldsymbol{B} - \boldsymbol{B}\boldsymbol{u}) + \boldsymbol{\nabla} \cdot \left(\mu_0 \beta_{\mathrm{AD}} \left[(\boldsymbol{J} \times \boldsymbol{B})\, \boldsymbol{B} - \boldsymbol{B}\, (\boldsymbol{J} \times \boldsymbol{B}) \right] \right) \\ &\quad = - \left(\boldsymbol{\nabla} \cdot \boldsymbol{B} \right) \boldsymbol{u} - \left(\boldsymbol{\nabla} \cdot \boldsymbol{B} \right) \left[\mu_0 \beta_{\mathrm{AD}} (\boldsymbol{J} \times \boldsymbol{B}) \right], \end{aligned} \tag{4.6}$$

where $\boldsymbol{g}$ is the gravitational acceleration, P is pressure, E is energy and $\boldsymbol{J} = \frac{1}{\mu_0} \boldsymbol{\nabla} \times \boldsymbol{B}$. Note that $\boldsymbol{\nabla} \cdot \boldsymbol{B} \neq 0$ in the scheme of Powell et al. (1999) used in FLASH. These these terms must be included to ensure stability. However, values are kept below truncation-level error by the scheme and through an additional diffusive cleaning method employed in FLASH after each timestep.

The overall application of this ionization formula in the code is relatively simple, but may become more complicated once charged grains become important. The effect of grains has been predicted to become important at densities of $n = 10^{10}$, from which point a multi-fluid approach may be necessary (Tassis & Mouschovias, 2007b; Nakano et al., 2002). A first reasonable step in dealing with ambipolar diffusion in highly time-dependent, 3D calculations is to take (4.1) as the ionization (Kudoh et al., 2007; Ciolek & Basu, 2006; Hosking & Whitworth, 2004a; Safier et al., 1997; Fiedler & Mouschovias, 1993). Further work on implementing the complications introduced by charged grains can later be developed and readily implemented.

4.2.3 Timestep

The Courant condition is satisfied by a diffusive timestep (Mac Low et al., 1995):

$$\tau_{\rm AD} = T_0 \frac{(\Delta x)^2}{\eta_{\rm AD}}, \tag{4.7}$$

where T_0 is a fudge factor (we typically use 1/30 or 1/120), (Δx) represents the smallest cell length and the ambipolar diffusivity is $\eta_{\rm AD} = \beta_{\rm AD} B^2$ (Zweibel, 2002). Clearly, the $(\Delta x)^2$ limitation is a harsh one, especially in an AMR simulation. New developments have been seeking to get around this in a two fluid approach (Li et al., 2006) claiming longer timesteps by factors of 10-100. Ultimately, however, the numerical need to resolve the Jeans mass will limit any simulation studying gravitational collapse with ambipolar diffusion to a maximal central density.

4.2.4 Testing of the Code

We have thoroughly tested our implementation of ambipolar diffusion in the FLASH code through i) qualitative tests of the quasi-static collapse of a magnetically supported critical cloud (based on numerical simulations done by Fiedler & Mouschovias (1993), ii) isothermal C-shocks (Mac Low et al., 1995) and iii) non-isothermal C-shocks with drift heating (Wardle, 1991a) and energy diffusion. The latter two provide analytic solutions in which we observed accuracy (below 0.5 % for poor resolutions of $L_{\text{shock}}/4$) and convergence when increasing our resolution. The third test was properly derived and customized by us in hopes that it become a standard test for non-isothermal ambipolar diffusion codes. The details can be found in Chapter 3.

4.3 Results and Discussion

4.3.1 Magnetic Braking, Magnetic Pressure and Fragmentation

Rotation poses a large obstacle to star formation due to the vast difference between rotational energy in molecular clouds and that observed in stars. Large initial rotational velocities are imparted upon these cores via oblique shocks from their turbulent beginnings. This is found to be on the order of $\Omega t_{ff} > 0.2$ for a third of the clouds in numerical simulations (Tilley & Pudritz, 2005). Magnetic braking has long been known to be very efficient at reducing large rotational velocities in clouds, through analytic (Mouschovias & Paleologou, 1986, 1980) and numerical studies (Machida et al., 2006; Banerjee & Pudritz, 2006; Hosking & Whitworth, 2004a; Basu & Mouschovias, 1994).

The physical process of magnetic braking involves interplay between a rotating cloud and the static ambient medium. As the cloud rotates, it drags field lines along with it. This transfers angular momentum to the external medium in the form of an outward propagating torsional wave at the speed of the Alfvén velocity $v_{\text{A}} = B_0/(4\pi\rho)^{1/2}$. By extracting angular momentum these Alfvén waves will effectively slow the cloud's rotation.

We compare the braking effects in ideal and non-ideal collapses on our low-mass

B68 model, starting with identical initial conditions. It is difficult to measure the effect of braking as the gas is collapsing. By conserving angular momentum, infalling material naturally rotates faster. Also, there are many physical processes at work which are actively redistributing angular momentum within the cloud (see §4.3.2). However, the external medium is initially non-rotating and any toroidal field built up must be generated purely by magnetic braking. Our method involves measuring the largest absolute value of the toroidal field outside the initial cloud radius. The maximum value gives a good indication of the strength of the outward propagating torsional Alfvén waves, and thus the efficiency of the magnetic braking.

In Figure 4.1 we observe that the maximum $|B_\phi|$ extracted in the non-ideal case is about 3/4 that of the ideal ideal collapse for a given time. From analytic models of magnetic rotors undergoing braking due to ambipolar diffusion, we can derive the relation:

$$E_{\text{toroidal}} = B_\phi^2/(8\pi) = \frac{1}{2}\rho r^2 \Omega^2 = \frac{1}{I_0} E_{\text{rotational}}, \tag{4.8}$$

where r is the cylindrical radius, E indicates an energy density, ρ is the density of the rotor (or our envelope, which we can approximate as constant) and $I = I_0 M r^2$ is the rotor's moment of inertia (I_0 is a dimensionless constant). This gives us an indication of the efficiency of magnetic braking. It also tells us that 'rotation extracted' is proportional to 'toroidal field generated', which completes our analysis of Figure 4.1.

We conclude that braking of a non-ideal cloud is about 3/4 as strong as ideal braking and use this to correct the rotation of our high mass model so the non-ideal simulation has 3/4 the rotation of its ideal counterpart. This is a important result as it has long been argued that magnetic braking through the addition of ambipolar diffusion is only affected by "a few percent" (Basu & Mouschovias, 1994; Mouschovias & Paleologou, 1986). These previous studies simulated quasi-static thin disks, so here

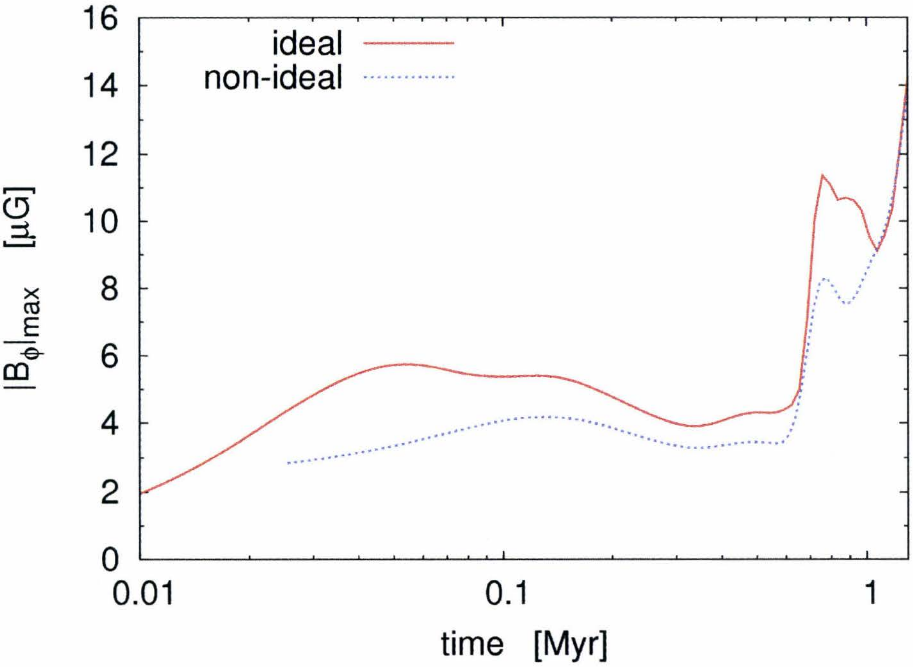

Figure 4.1: The evolution of the largest value of $|B_\phi|$ outside 1.9×10^{18} cm from the center, which is about the initial radius our low-mass B68 model. The ideal model (solid red line) is more efficient at generating a toroidal field through magnetic braking than the non-ideal model (dashed blue line) by about 4/3.

collapse is playing an important role in mediating braking affects.

Recent studies of fragmentation with ambipolar diffusion have also suggested that the effect of decreased magnetic braking is indeed significant, leading to increased rates of fragmentation. However, it is magnetic pressure which plays a dominant role in supporting the collapsing cloud against instabilities that would otherwise form (Price & Bate, 2007; Banerjee & Pudritz, 2006). We present x-y snapshots of the B68 model during the later phases of its evolution in Figures 4.2 and 4.3. In the ideal case the magnetic pressure is observed to form a ring and then fragment into two clumps at a separation of (2-3 AU). The density follows this by forming a bar which fragments into 2 clumps. These clumps oscillate between separated and rejoined from then on. In the non-ideal case, magnetic pressure support is seen as reduced and noticeably fragmented. This allows fragmentation on much larger scales due to a strong reduction in effective magnetic pressure (note scale differences in Figures 4.2 and 4.3 by an order of magnitude). The disk in this case forms a wide ring which has fragmented into 2 or 3 clumps at 10 AU separations at the point we end the simulation. This is consistent with purely hydrodynamic collapse simulations of B68 (with these parameters) which suggest instablilities such as rings form on scales of 200 AU, much larger than their magnetic counterparts which find similar results as in Figure 4.2 (Banerjee et al., 2004; Banerjee & Pudritz, 2006). In this case, the ambipolar diffusion collapse is seen to lie somewhere between a hydrodynamic and a magnetohydrodynamic collapse.

We conclude that ambipolar diffusion increases significantly the rate of fragmentation of the disk by reducing magnetic pressure support within it.

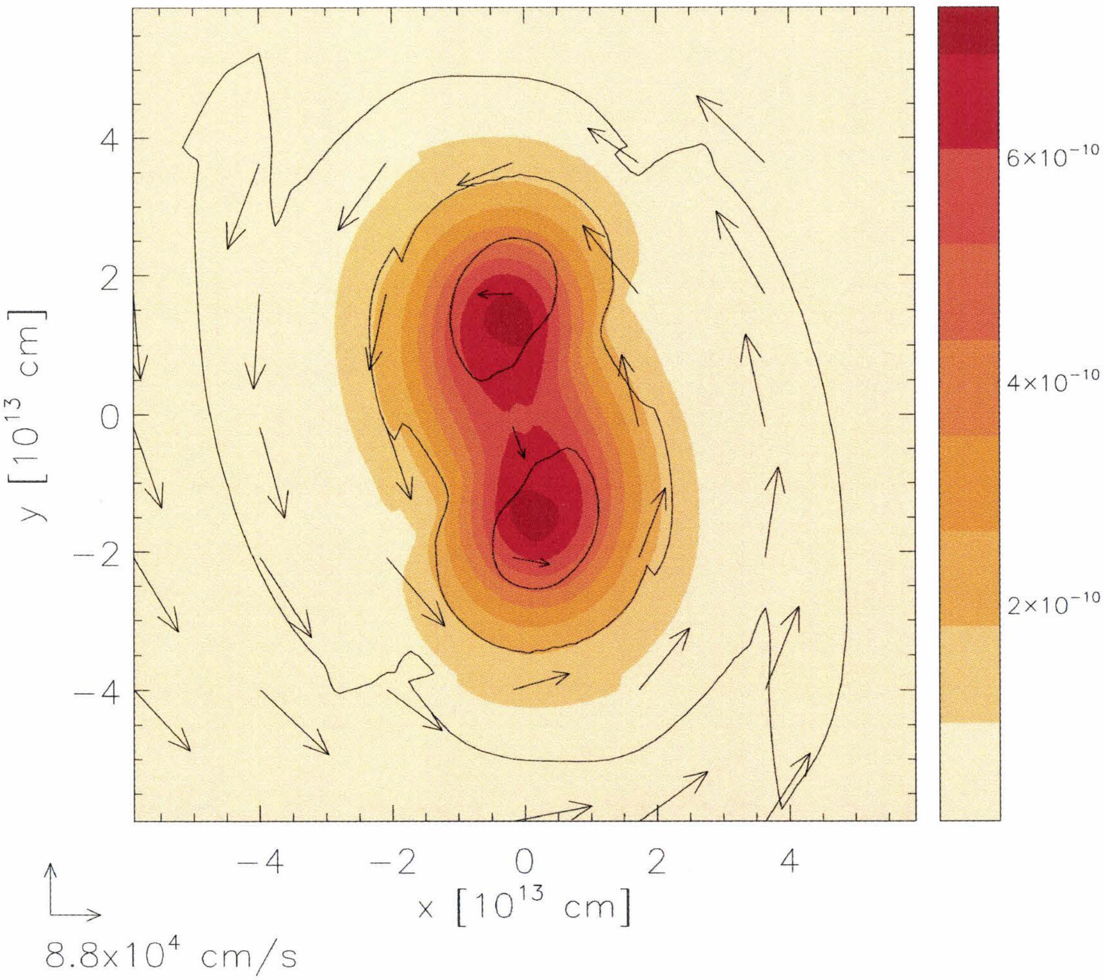

Figure 4.2: Fragmentation of our low mass model from the ideal collapse of B68. Presented through x-y pseudocolors (linear in density) behind magnetic pressure contours (each contour represents a shift of $10^{0.7}$ dyne cm^{-2}). The ideal simulation above may be compared with the non-ideal simulation in Figure 4.3. Note the different scales, times and densities of the models (ideal model: $t = 1.52$ Myr, $n_{\max} = 2.03 \times 10^{14}$ cm^{-3}; non-ideal model: $t = 1.47$ Myr, $n_{\max} = 4.23 \times 10^{12}$ cm^{-3}). Separations are about (2-3) AU for the ideal model and 10 AU for the non-ideal model.

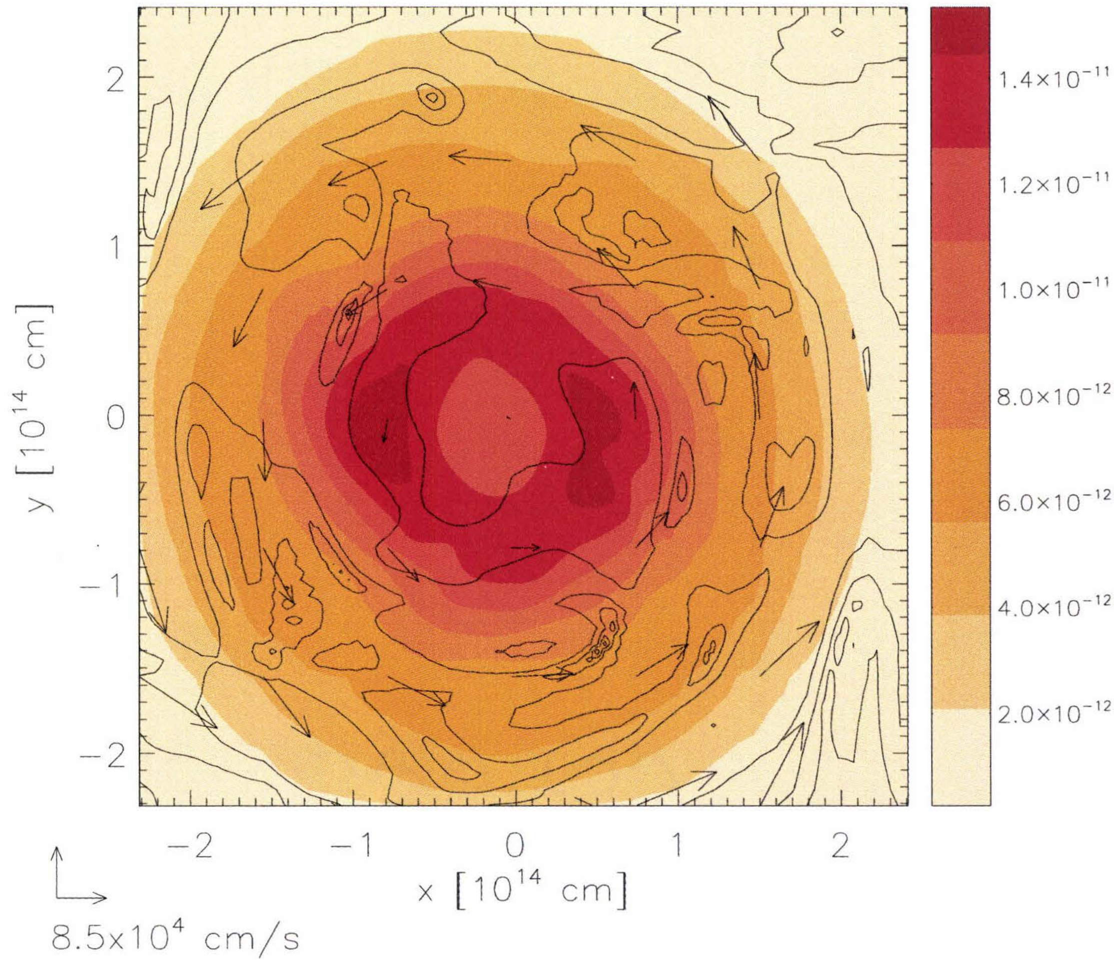

Figure 4.3: Fragmentation of our low mass model from the non-ideal collapse of B68. The graph properties are similar to those of Figure 4.2 except for a difference in scale by about an order of magnitude. Note that pressure contours are maximal in a ring about the center, and decrease towards the center (they trace the density somewhat).

4.3.2 High Accretion Rates Persist

We show that in the collapse of our high mass model, ambipolar diffusion does not affect the high mass accretion rates observed in previous studies (e.g. Banerjee & Pudritz, 2007). This is due to the fact that magnetically driven redistribution of angular momentum is still effective in a resistive medium. Drift heating is found to be apparent in shocked structures as well as in the disk.

We compare collapse profiles of a hydrodynamic (HD) collapse, an ideal magnetic collapse and a magnetic collapse with ambipolar diffusion. For our results we have chosen the end state of our ambipolar diffusion run and compared that with states in HD and ideal runs which have similar central column densities of about 300 g cm^{-3}. These are not very high values of column densities due to the strong limiting timestep of ambipolar diffusion (see §4.2.3).

Differences in the profiles shown in Figures 4.4-4.6 begin to become apparent inside about (200-300) AU, the disk envelope. Drift heating has been shown to have a strong effect on pressures and temperatures in shocks through analytic solutions derived by Wardle (1991a) and in our C-shock test runs which included drift heating as well as efficient cooling approximated from Lepp & Shull (1983). It is seen to dramatically increase the pressure in the presence of efficient cooling, compared to a C-shock where drift heating and cooling are turned off. This extra thermal support will cause more bunching up of gas in magnetically driven shocks, as seen in the column density profiles in Figure 4.4[1]. In particular, the ambipolar collapse shows

[1]All quantities are azimuthally averaged, weighted with density ρ such that a value $f(R) = [2\pi\Sigma(R)]^{-1} \int dz d\phi \rho(\boldsymbol{x}) f(\boldsymbol{x})$, where $\Sigma(R) = (2\pi)^{-1} \int d\phi dz \rho(\boldsymbol{x})$ is the column density as a function of cylindrical radius R. Note that temperature values taken under this averaging are deceptive, as central temperatures in the ambipolar model actually reach more than 500 K by the time we end the simulation. This is due to concentrations of high temperatures in small regions. However, our method nonetheless captures the general

additional heating in the initial shock at about 100 AU. Further heating inside the disk occurs due to the intense dragging of field lines along magnetized disk layers, as described in §4.3.3.

We find accretion rates in our ambipolar model of

$$\left(\frac{dM}{dt}\right)_{\max} = 10^{-3}\ \mathrm{M}_{\odot}\ \mathrm{yr}^{-1} = 60\ c_{\mathrm{iso}}^{3} G^{-1} = 89.5\ c_{\mathrm{local}}^{3}\ G^{-1}, \tag{4.9}$$

where c_{iso} is the original isothermal sound speed at 18 K and $c_{\mathrm{local}} = P/\rho$ is a local approximation of the thermal sound speed. The magnetized cases have higher accretion rates than the non-magnetized case. The mass accretion rates have similar profiles when plotted in units of the local sound speed. This reflects the fact that the gas is supersonic and inflow velocities are sensitive to higher temperatures and the Mach number (as discussed in Banerjee & Pudritz (2007)). Figure 4.5 shows the infall velocities, showing maximal supersonic infall on the order of 2-3 c_{local}. The ambipolar drift heating in this case is providing additional thermal energy to the magnetic shock at 100 AU which boosts infall speeds, but the overall local profiles are similar.

We also note that these are early stages for these types of simulations and accretion rates will continue to rise. It is difficult to follow disk evolution very far because of the severe limitation of the ambipolar diffusion timestep. The effects of magnetism on collapsing magnetized cloud cores, with similar initial profiles as our high mass model, found that at central column densities of 5000 g cm^{-2}, accretion rates had reached 10^{-3} M$_{\odot}$ yr^{-1} (Banerjee & Pudritz, 2007). In our simulation, the ideally magnetized collapse has only reached column densities of 300 g cm^{-2} and accretion rates of 4×10^{-4} M$_{\odot}$ yr^{-1}. From this we expect mass accretion rates should increase through further evolution of the collapse. Note that the ambipolar diffusion collapse already shows about twice the mass accretion rate of its ideal counterpart, due to

trends in this case.

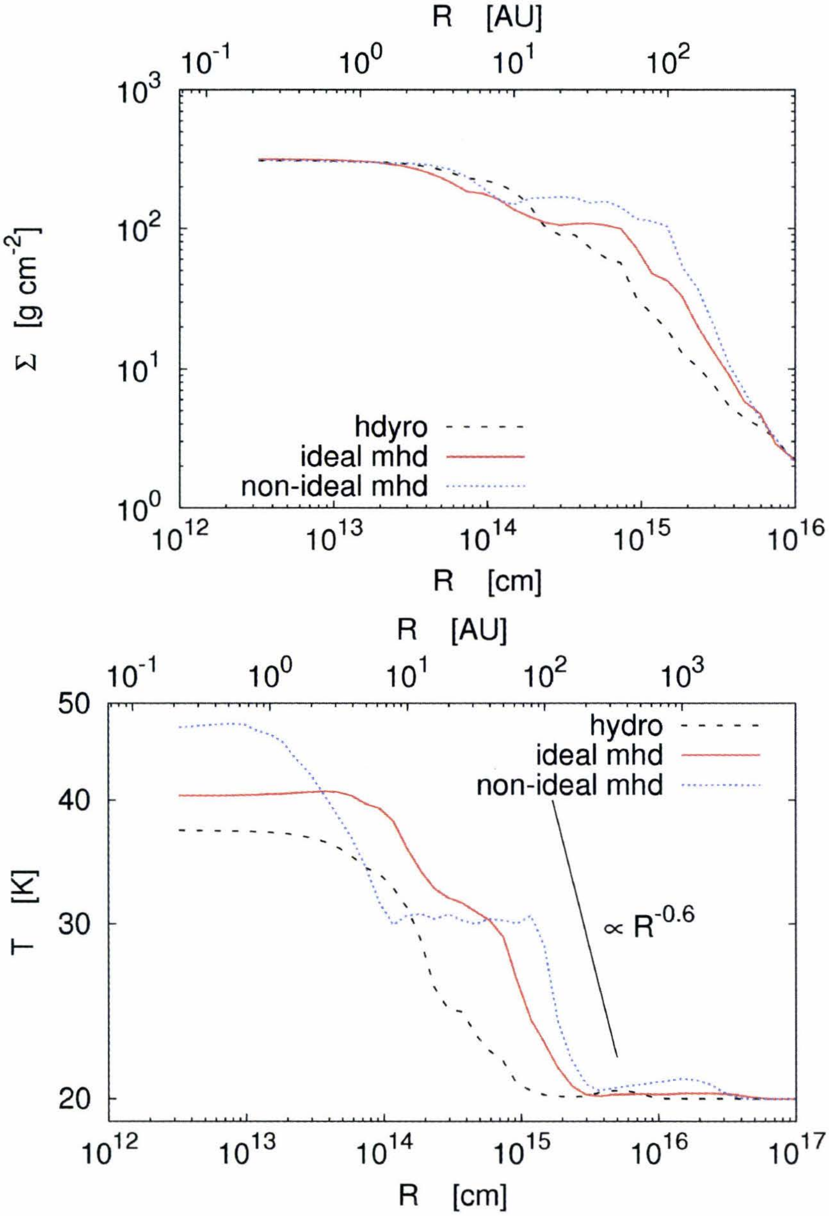

Figure 4.4: The column density profiles (above) and temperature profiles (below) of the high mass model, comparing hydrodynamic, ideal MHD, and ambipolar MHD collapses. One can connect drift heating at 100 AU to the surface density bunching there. Profiles to the right of the graph are very nearly identical; the temperatures are isothermal and the column density follows a $\Sigma \propto r^{-1.2}$ profile. We show that the general trend of temperature inside 100 AU is approximately $T \propto r^{-0.6}$, though clearly the heating and cooling produce a complicated profile.

decreased support from magnetic pressure.

In the inner regions of the disk, magnetic coupling has decreased significantly. We observe a gradual change of behaviour in the ambipolar collapse which initially follows the ideally magnetized profile but deviates at small distances. This effect is independent of the choice of thermal sound speed (though less so in the local sound speed approximation), and thus stems from a non-thermal cause. As coupling is lost, so is magnetic support in the disk midplane and this drives up accretion rates to a more hydrodynamic profile.

Magnetic torques extract angular momentum and create higher accretion rates. Figure 4.7 shows the efficiency of this process through profiles of the z-component of specific angular momentum, $j_z = (\boldsymbol{r} \times \boldsymbol{u})_z$, where $\boldsymbol{r}$ is the radial position and $\boldsymbol{u}$ is the velocity. Note that originally the ideal core had 2 and 4/3 times the angular momentum of the HD and ambipolar collapses respectively. Also note that the initial distribution of angular momentum is that of a solid body and that j_z vs M should be constant in time if j_z is *not* redistributed within the disk.

Magnetic torque is efficient enough at extracting angular momentum to drive j_z below HD values for much of the disk and surrounding envelope. Due to the lack of magnetic coupling inside the inner disk of 20 AU, these processes are inefficient for the ambipolar collapse. It has a higher angular momentum than the HD case here as due to the fact that it started out with more rotation and that only HD processes are effective in an decoupled zone.

Plotting j_z with respect to mass is important as it should be constant with time if angular momentum is not redistributed in the disk. In the lower graph of Figure 4.7 we see that j_z vs M is not constant with time in all three cases. The principal effect is due to the formation of a bar in the disk which naturally extracts angular momentum

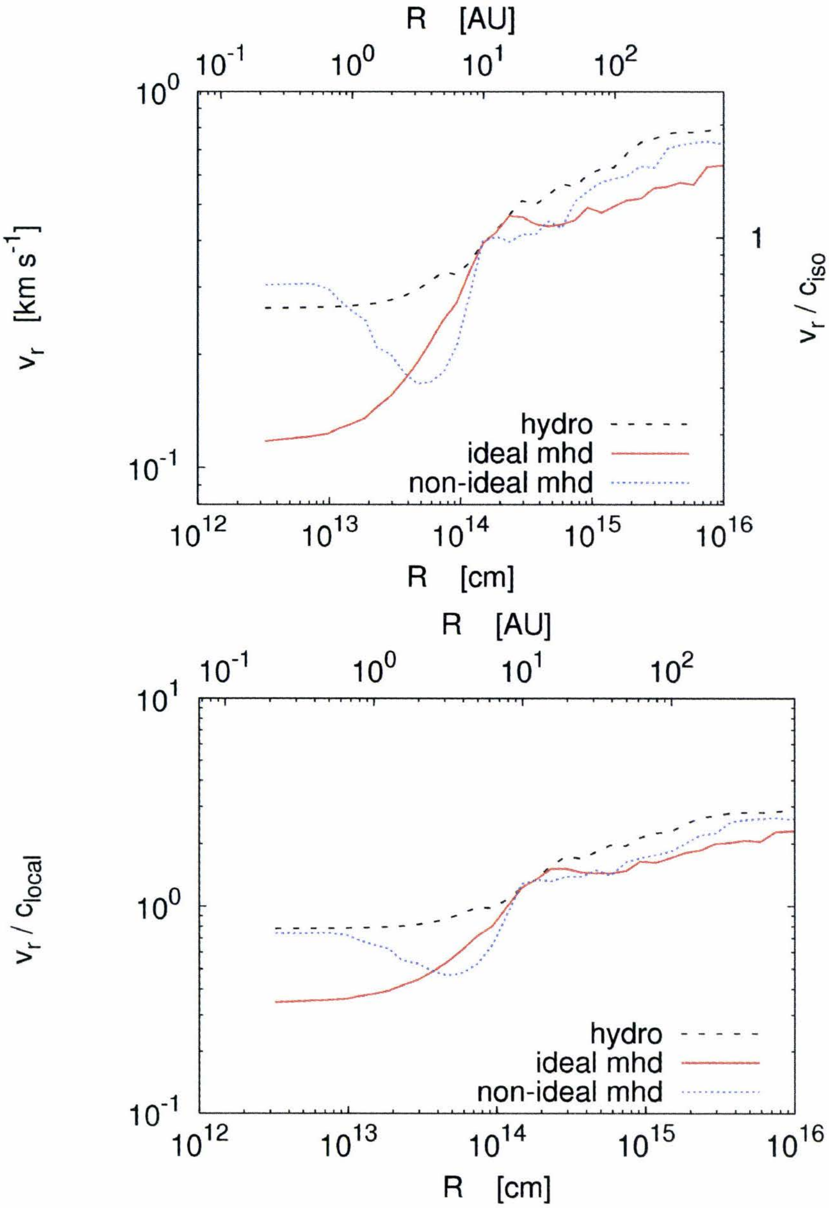

Figure 4.5: Radial infall velocites for hydrodynamic, ideally and partially magnetized models. The upper graph gives the normal infall velocities in km s^{-1} and in units of the isothermal sound speed $c_{\rm iso}$. The lower graph corrects for the effects of heating by replacing $c_{\rm iso}$ with $c_{\rm local}$, the local isothermal sound speed. Even with this correction, infall rates are seen to be supersonic. Central column densities of $\Sigma_c = 300$ g $\rm cm^{-2}$ are the same for each model.

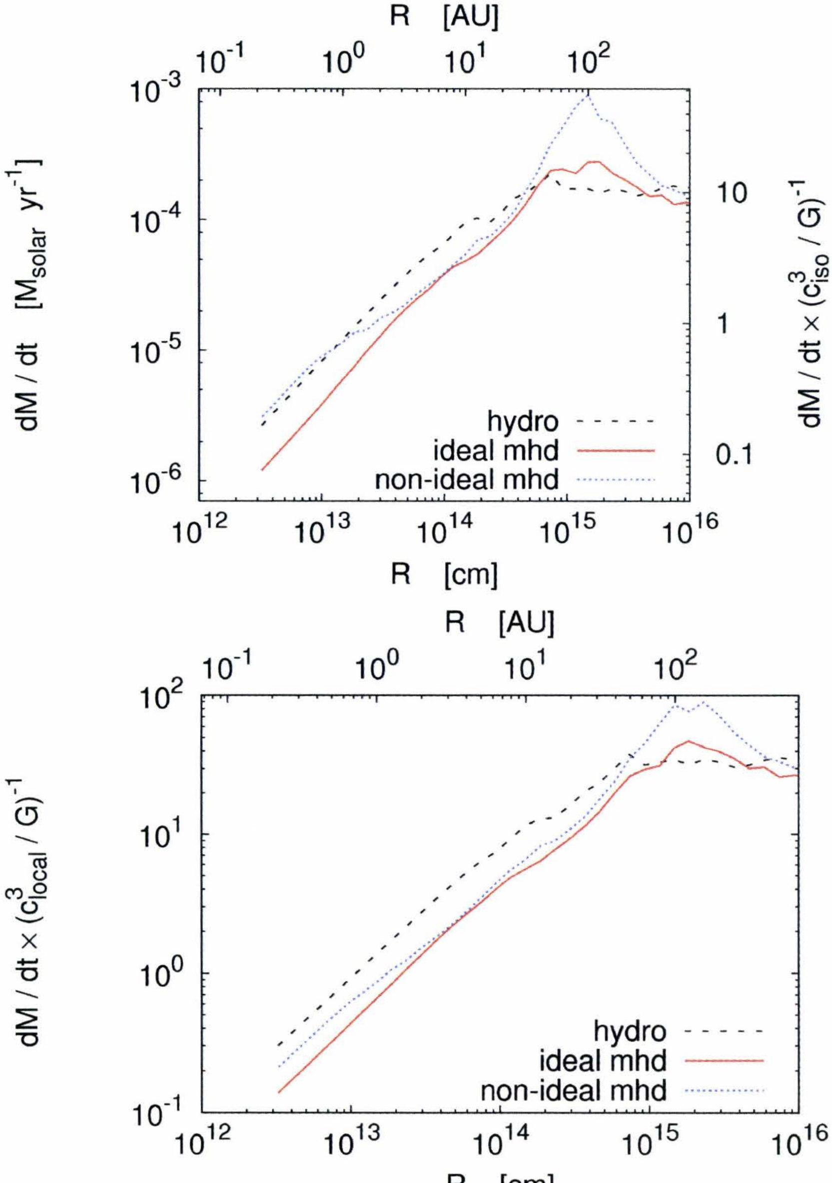

Figure 4.6: Mass accretion rates for hydrodynamic, ideally and partially magnetized models. Note that the limitation of the diffusive timestep (§4.2.3) has halted simulations quite early and these rates should increase with further evolution of the cloud. The upper graph gives the normal accretion supersonic accretion rates in $M_\odot$ yr^{-1} and in $c_{\rm iso}^3\ G^{-1}$, where c_{iso} is the isothermal sound speed. The lower graph corrects for the effects of supersonic collapse by replacing c_{iso} with c_{local}, the local isothermal sound speed. Central column densities of $\Sigma_c = 300$ g cm^{-2} are the same for each model.

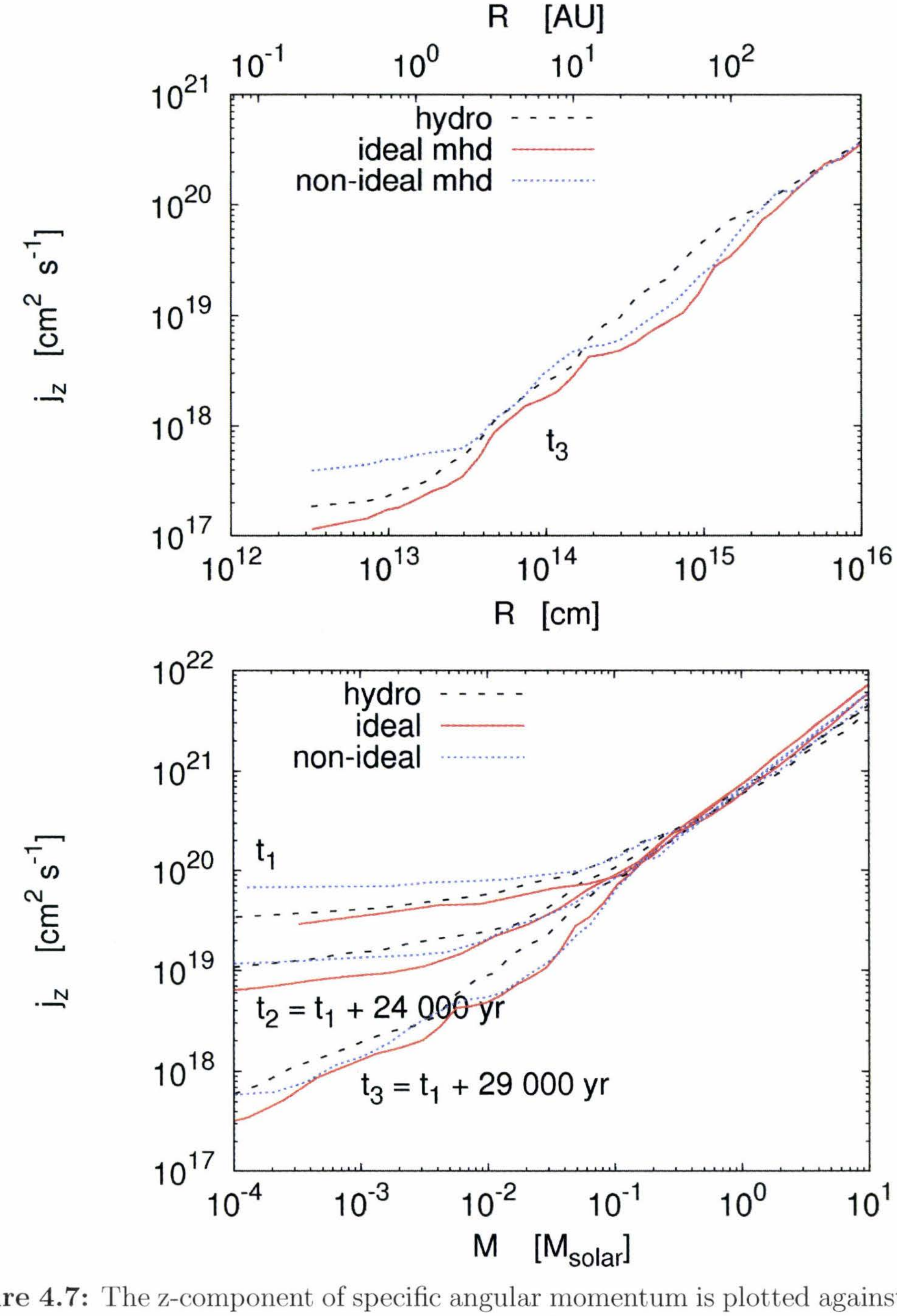

Figure 4.7: The z-component of specific angular momentum is plotted against cylindrical radius and enclosed mass in these cylindrically averaged profiles of each collapse, for three different times. In the upper graph, the states are at an identical central column density of 300 g cm^{-2}. In the lower graph, the time t_1 is chosen such that by time $t_3 = t_1 + 29000$ yr the column densities of each model have reached 300 g cm^{-2}. Time $t_2 = t_1 + 25000$ yr is an intermediate time. The profile of j_z vs M should be constant in time if j_z is not transported in the disk.

as gas collides with it or is drawn to it through gravitational attraction. We have taken a snapshot of this distribution in the bottom graph of 4.7 for three different times starting at some time t_1 (not necessarily the same for each case). At this point we see that the ambipolar starts out lagging behind both the hydro and the ideally magnetized collapses. However, after 24 000 yr (t_2) magnetic process have begun to take effect, and more of the ambipolar j_z distribution follows with the ideal collapse. Another 5000 yr (t_3), when the column density has also reached 300 g cm^{-2} in each model, a clear hierarchy is seen with the HD collapse having more angular momentum than the other two, and the ambipolar run lying in between. This is to be expected as magnetic effects are generally decreased in the non-ideal collapse. We conclude that the effects of magnetism are gradually aligning the j_z profiles of ideal and non-ideal collapses. Interior regions of the ambipolar collapse show a more hydrodynamic profile as magnetic processes are slower to enact redistribution of j_z. However, once these processes do take effect, they are very efficient and angular momentum profiles share more in common with those of the magnetic case than the hydro case.

4.3.3 Effects on Disk Shock Structures and Field Lines

A large scale feature of note is the large scale accretion shock that occurs on scales of 1000 AU in the vertical direction (see Figures 4.8, 4.9 and 4.10 for the ideal, non-ideal and HD case respectively). Accreting gas in the cloud midplane is fed through the vertical collapse of the envelope. As gas hits the midplane it clumps up in a shock and is forced to make a sudden transition in velocity. This shock can become non-isothermal as pressure forces from the infalling gas and magnetic fields become strong enough to make cooling inefficient in face of accretion and possible drift heating. We see in Figure 4.9 how the temperature distribution of the shock in the non-ideal collapse makes a much more continuous transition through the shock before it is effectively cooled off in the post-shock region than it dos in the ideal case in Figure 4.8. This profile is similar to that of a C-shock, rather than the sharp J-shock type transition made by the ideal collapse. Flow times at this density ($n_{\rm shock} \approx 10^5$ cm^{-3}) are on the order of $t_{\rm flow} = 10^7$ s and length scales are on the order of $L_{\rm shock} = 10^{13}$ cm. We note that in running analytic and numeric tests of C-shocks with drift heating that it is not unusual to see gradual changes of pressure and temperature on the order of (50-100) $L_{\rm shock}$ while other variables make sharper transitions on the order of (2-10)$L_{\rm shock}$ (where ambipolar diffusion is strong). Thus it is not surprising that we find this feature well developed in a collapse that has a freefall time on the order of 10^{13} s.

Also, by comparing to the hydrodynamic features on this scale we see the role of magnetic pressure is to prop up this large scale shock structure. In Figure 4.8, which shows the ideal MHD case, the "disk" is quite thick, while it becomes thinner as magnetic support is lost partially in the non-ideal case(Figure 4.9) and even more so when there is no magnetic support in the HD case (Figure 4.10).

Magnetic field build up is an important issue to understand. Measurements by Levy & Sonett (1978) note the presence of large fossil fields of about 3 G at 1 AU sometime in our solar system's history. Recent measurements by Donati et al. (2005) find 1 kG fields in the core of the protostellar accretion disk FU Orionis. This has been resolved through ideal MHD calculations of Barnard 68 through which previous studies (Banerjee & Pudritz, 2006) show a 3 kG field being built up at 0.05 AU, along with the production of a jet and a large scale disk wind. It was unclear if the role of ambipolar diffusion in limiting this value. In Figure 4.11, we plot the poloidal field profile for the collapse of our high mass model, comparing ideal and

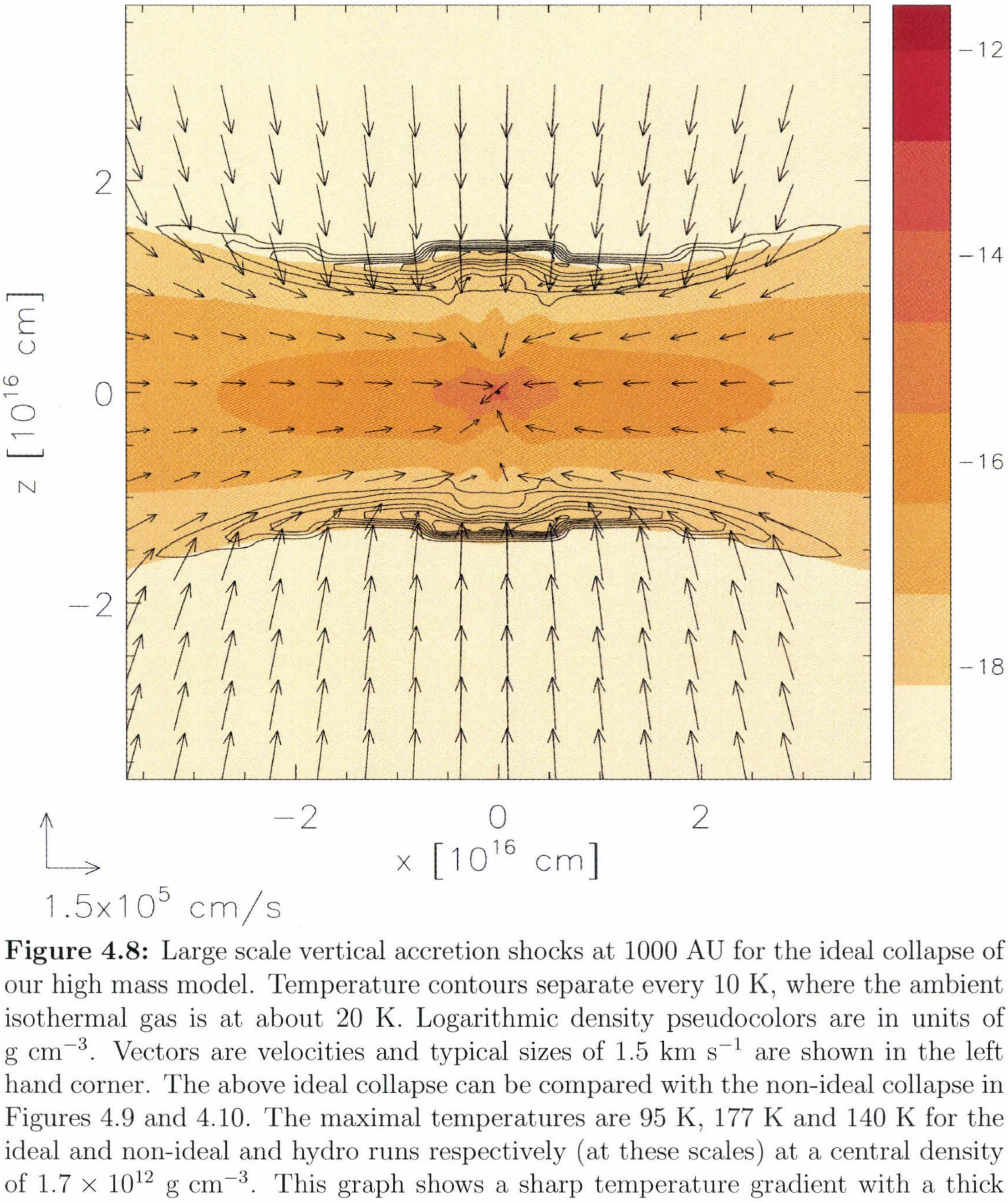

Figure 4.8: Large scale vertical accretion shocks at 1000 AU for the ideal collapse of our high mass model. Temperature contours separate every 10 K, where the ambient isothermal gas is at about 20 K. Logarithmic density pseudocolors are in units of g cm^{-3}. Vectors are velocities and typical sizes of 1.5 km s^{-1} are shown in the left hand corner. The above ideal collapse can be compared with the non-ideal collapse in Figures 4.9 and 4.10. The maximal temperatures are 95 K, 177 K and 140 K for the ideal and non-ideal and hydro runs respectively (at these scales) at a central density of 1.7×10^{12} g cm^{-3}. This graph shows a sharp temperature gradient with a thick magnetically supported accretion disk.

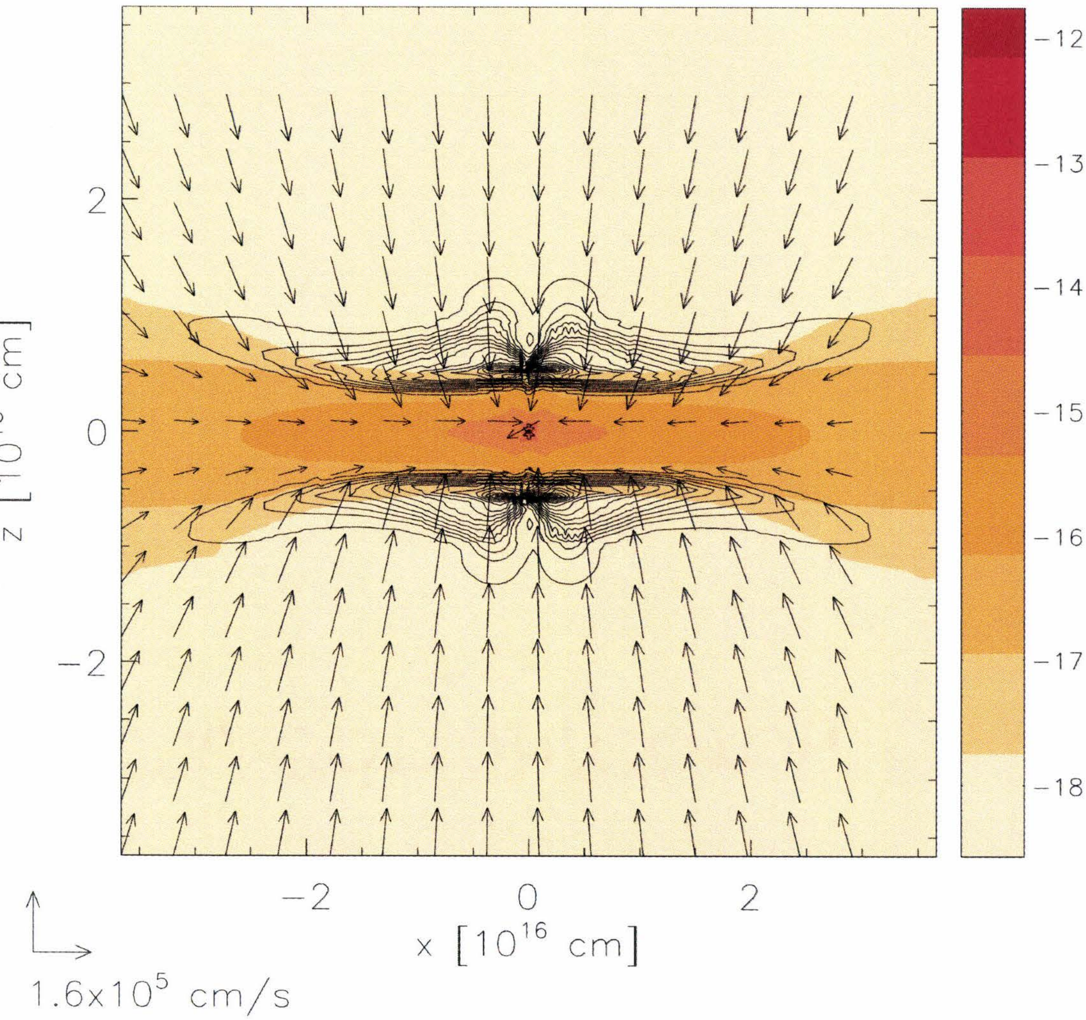

Figure 4.9: Large scale vertical accretion C-shocks at 1000 AU for the non-ideal collapse of our high mass model. Graph properties are similar to those of Figures 4.8 and 4.10 and show a thin disk disk with a gradual temperature gradient. This is a clear example of the importance of drift heating and C-shocks even in this low density regime.

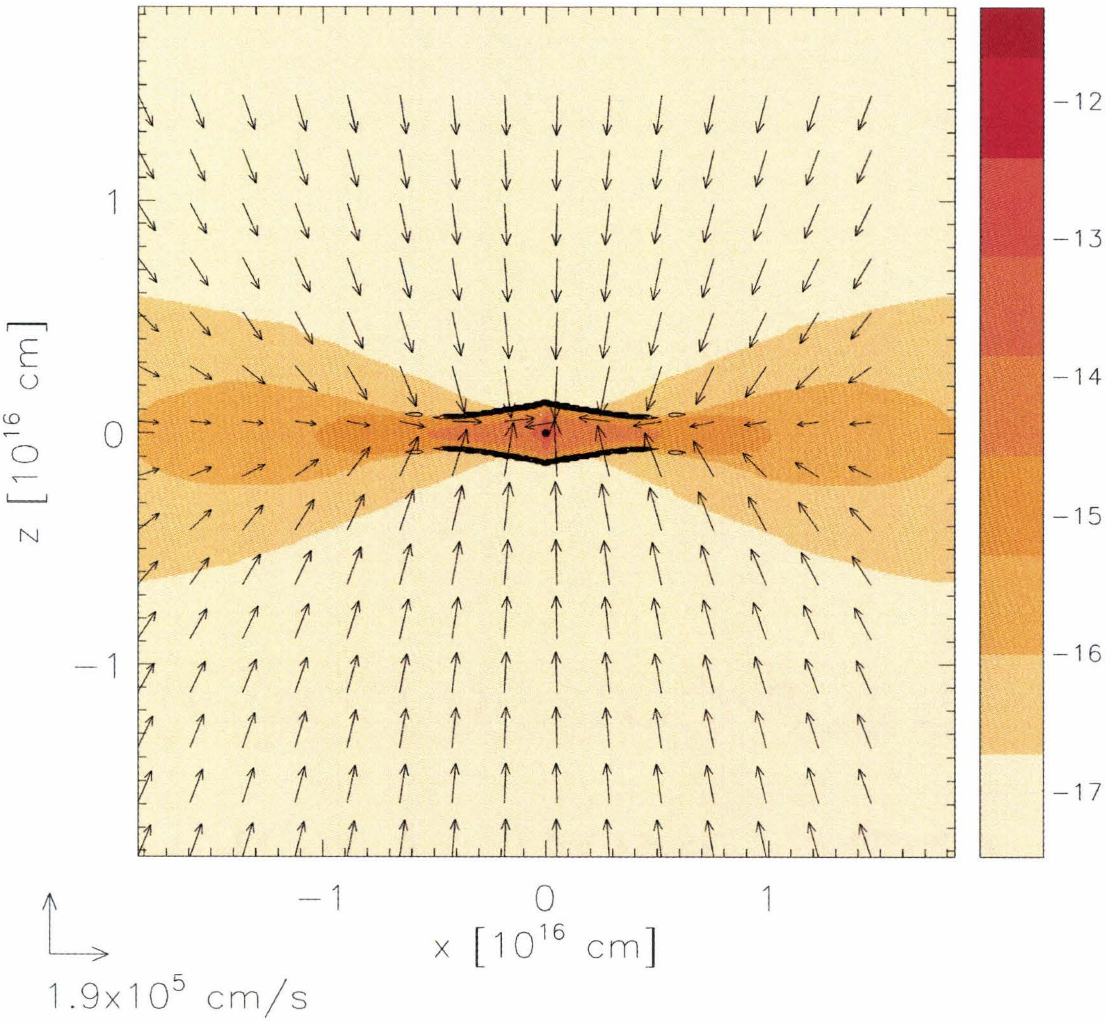

Figure 4.10: Large scale vertical accretion shocks at 1000 AU for the purely hydrodynamic collapse of our high mass model. Graph properties are similar to those of Figures 4.8 and 4.9 and show a much thinner disk with a sharp temperature gradient.

non-ideal collapses at a common column density of 300 g cm^{-2}. We find that central values of $B_z = 0.032$ G in the ambipolar collapse are lower by a factor of 1.8 to that of the ideal collapse. Also, much of the radial profile is shared by the two models. Lagging is seen in the region of (300-2000) AU by the non-ideal collapse. However, this is made up in at 100 AU as more gas builds up due to active drift heating. In the disk, lack of magnetic coupling begins to affect magnetic field build up. From these simulations it does not appear as if ambipolar diffusion is seriously damping the build up of magnetic field, so that large fossil fields can still build up through the initial collapse. It will be important to follow the evolution of the collapse further to understand if this radial trend continues in a near self-similar fashion, as seen in the ideal collapse. If so, then we can predict the existence of large fossil fields of about 1 G at 1 AU and 100 G at 0.01 AU (where we have not accounted for steepening of the profile seen in later stages of the collapse). We need to follow this collapse to much higher densities and include the effects of grains and cosmic ray shielding before we can be completely confident that this conclusion is 'real'.

To further investigate the idea that ambipolar diffusion allows sufficient magnetic field transport in a collapse, we plot magnetic field strength versus density in our low mass simulation of B68 (which reaches higher central densities, with albeit weaker resolution). We fit power laws to the trends and find $B \propto n^{0.47}$ is followed in our non-ideal collapse, recovering a well known astrophysical power law observed over many orders of magnitude in density, and predicted through numerical simulations studying ambipolar diffusion (e.g. Desch & Mouschovias, 2001). We also recover the relation $B \propto n^{0.6}$ in our ideal collapse, as discussed in (Banerjee & Pudritz, 2006) studying the same ideal collapse of B68. The effect of ambipolar diffusion is more qualitatively clear in this case, suggesting that the B-n relation is the result of a finite conductivity in collapsing molecular cloud cores.

We note that the instability present in the disk is a strong bar on the scale of 100 AU. This structure is nearly identical for ideal and non-ideal cases. We show x-y plots of the instability in both case in Figures 4.12 and 4.13 to demonstrate the 3D nature of the collapse. For disk plots, we take slices for $y = 0$. Note that the ideal bar is a bit fatter than the non-ideal bar due to increased magnetic support.

To complete the picture of collapse and to better understand the physical processes at work, we take a look at the inner disk through 2D images. Here we are comparing magnetized and partially-ionized collapses such that each have the same central density $\rho_c = 6.25 \times 10^{-12}$ g cm^{-3} $= 1.73 \times 10^{12}$ cm^{-3} (corresponding to the end of our ambipolar collapse). In the ideal disk shown in Figure 4.14 we see that a strong mass accretion rate in the disk midplane is effective in building up magnetic field, as seen in the pinching of field lines there. This cannot be the case in a disk with ambipolar diffusion as coupling is weakest in the midplane (recall $\chi = n_i/n_n \propto n_n^{-1/2}$ through a simple chemical analysis). A more striking result seen in the non-ideal disk depicted in Figure 4.15 is that field lines are effectively dragged across actively coupled disk layers and left behind in the disk midplane. Also we find that the disk shock structure is very puffy, more-so in the vertical direction than the horizontal direction. This corresponds to heating of areas where the dragging is strong. Coupling is not strong enough in the layers, however, to prevent a significant increase in the gas movement against the field lines as compared to the ideal model. This allows gas to flow in layers above the disk shocks and subsequently break through the shock fronts nearer to the central regions of the disk. Also note the appearance of small outflow motions beginning in the non-ideal disk while the ideal disk will only begin this process at a few orders of magnitude *higher* central densities (see §4.3.4).

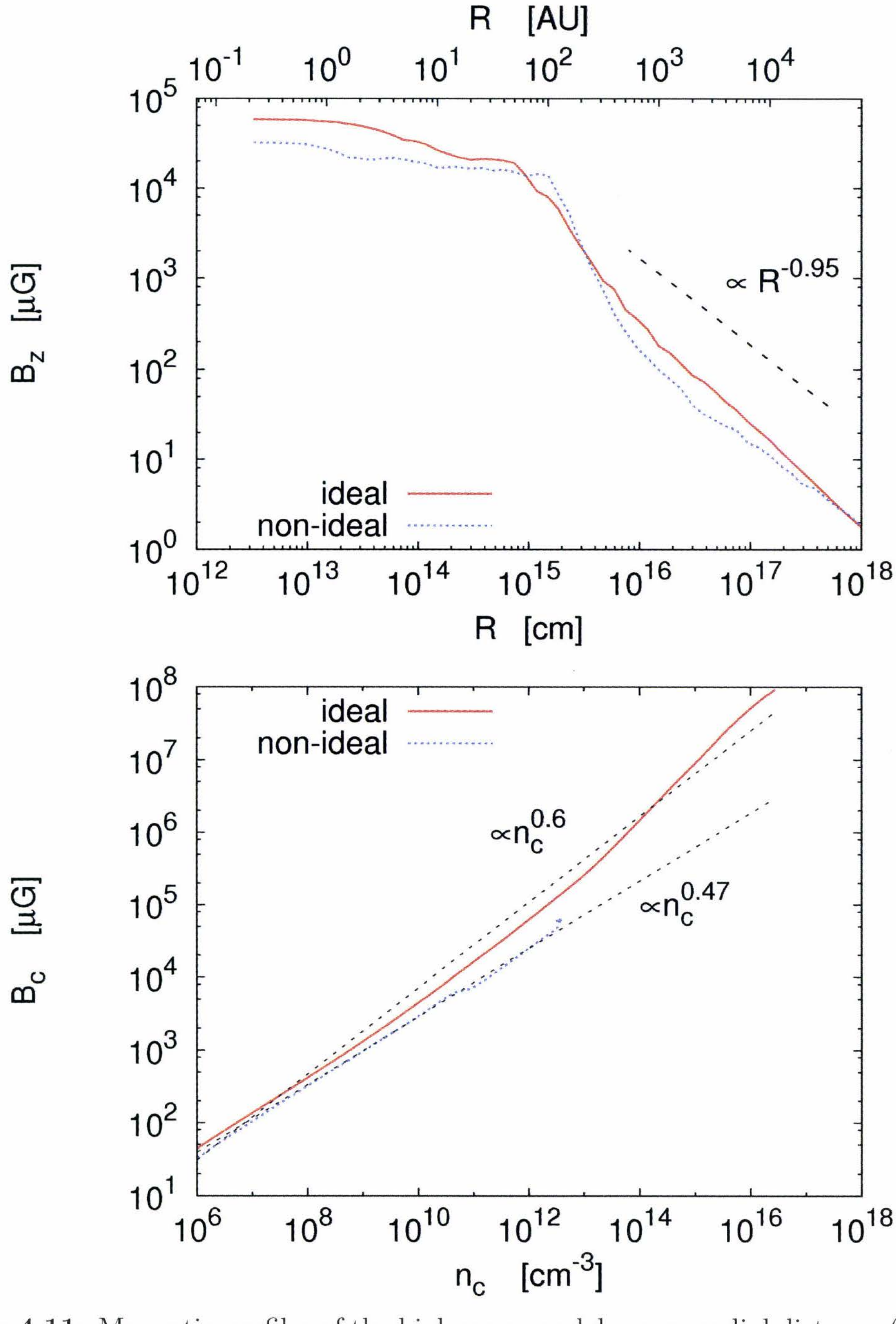

Figure 4.11: Magnetic profiles of the high mass model versus radial distance (above) and the low mass model versus central density (below). The upper graph shows the poloidal field strength profiles for ideal and non-ideal collapses at a column density of $\Sigma_c = 300$ g cm^{-2}. The lower graph depicts the variation of magnetic field strength with density in the collapse of B68. We have fitted power law trends to the data.

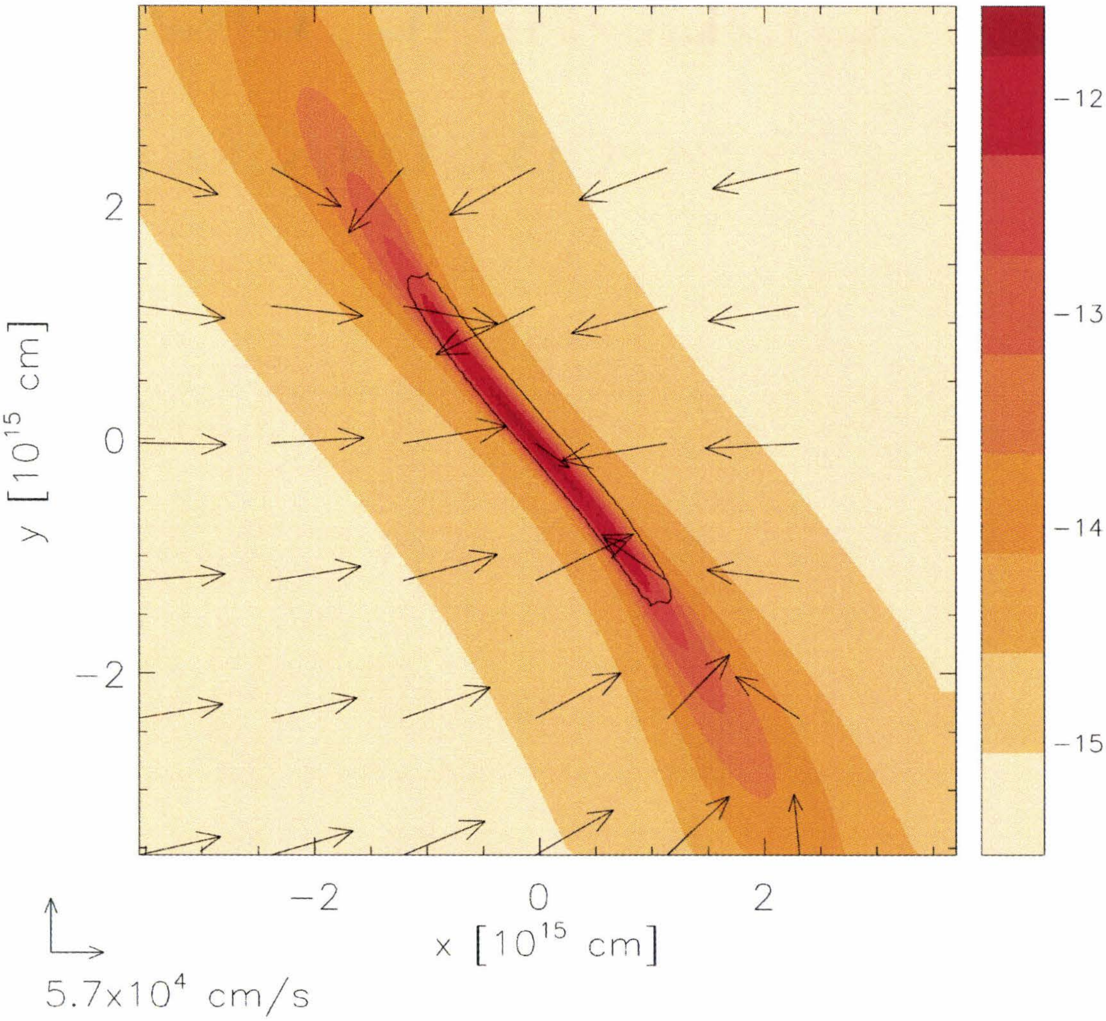

Figure 4.12: Density pseudocolor in the x-y plane (in g cm^{-3}) of the ideal disk of the high mass model showing the bar. Central densities are $\rho_c = 1.7 \times 10^{12}$ cm^{-3}, identical to those reached in Figure 4.15. Velocity vectors of 7.6 km s^{-1} are shown in the bottom left corner. Temperature contours are every 10 K. Note the similarity to Figure 4.13. The ideal bar is slightly fatter than the non-ideal bar.

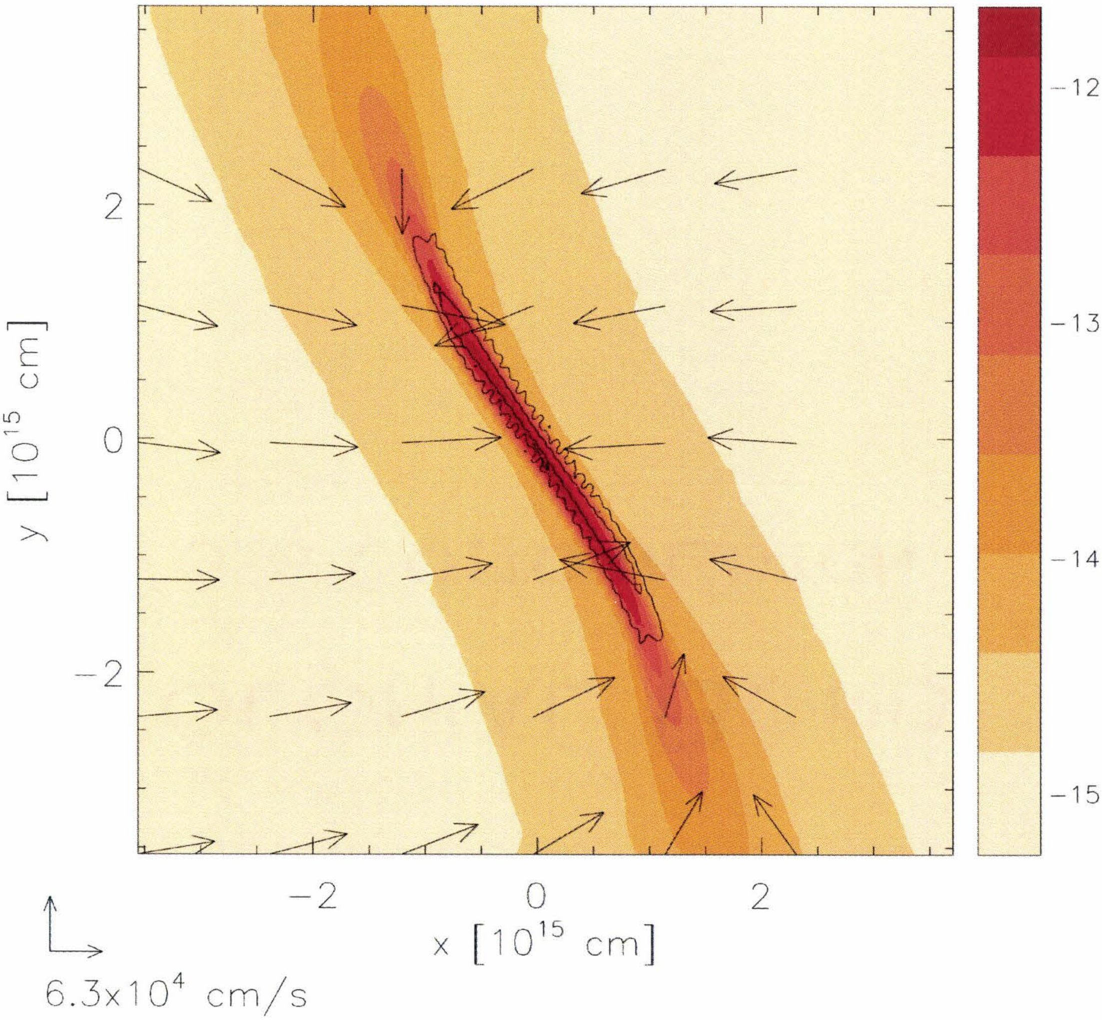

Figure 4.13: Density pseudocolor in the x-y plane (in g cm^{-3}) of the non-ideal disk of the high mass model showing the bar. Graph properties are comparable to those in Figure 4.12. Note the slight angular displacement of this image relative to the ideal case, indicating the difference in initial rotation combined with magnetic braking effects. Spiral structure appears unaffected by the introduction of ambipolar diffusion.

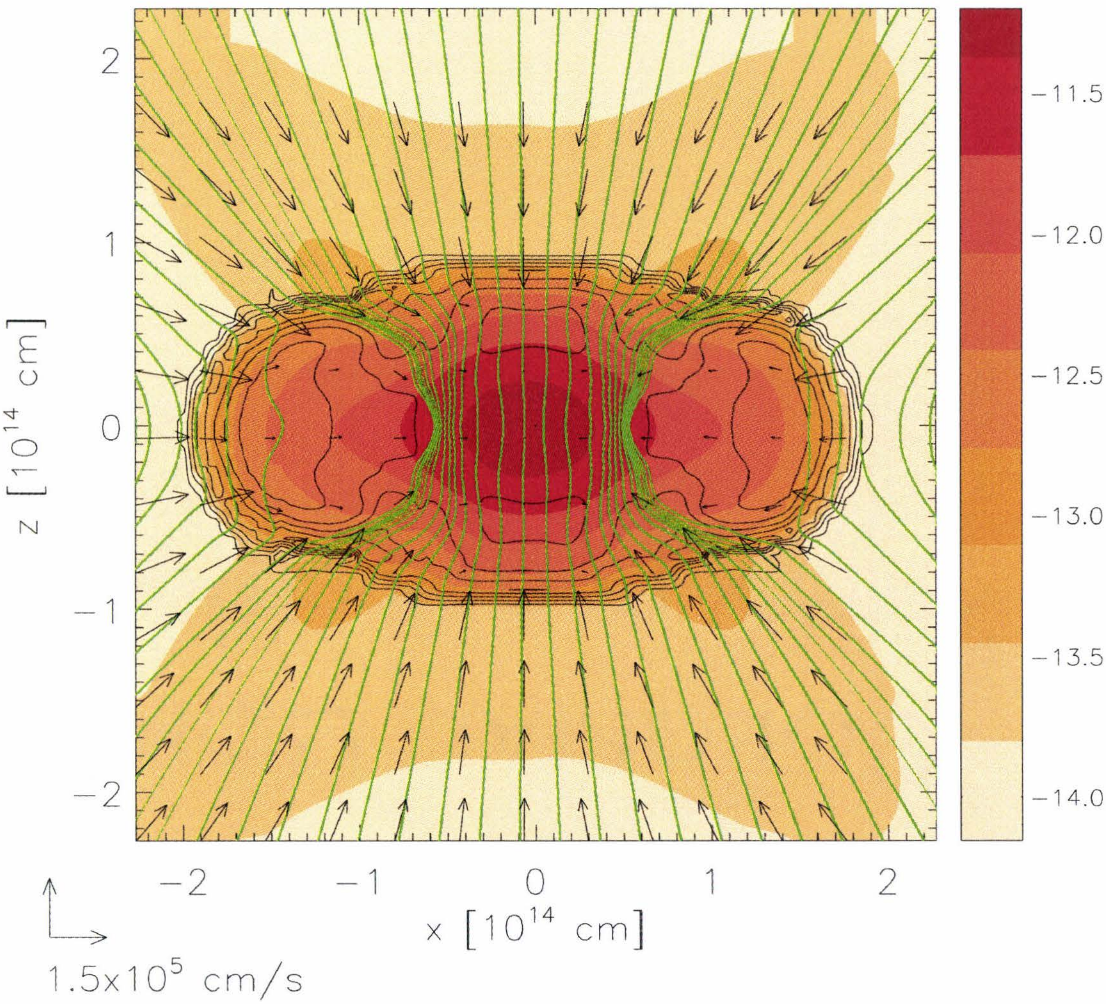

Figure 4.14: Density pseudocolor in the x-z plane (in g cm^{-3}) of the ideal disk of the high mass model. Central densities are $\rho_c = 1.7 \times 10^{12}$ cm^{-3}, identical to those reached in Figure 4.15. Field lines are in green and typical velocity vectors of 1.6 km s^{-1} are shown in the bottom left corner. Note that field lines integration omits y-component values of $\boldsymbol{B}$ and the magnetic void in the ideal disk is filled in by toroidal field components in facing in/out of the page (see Figure 4.18). Temperature contours are every 10 K.

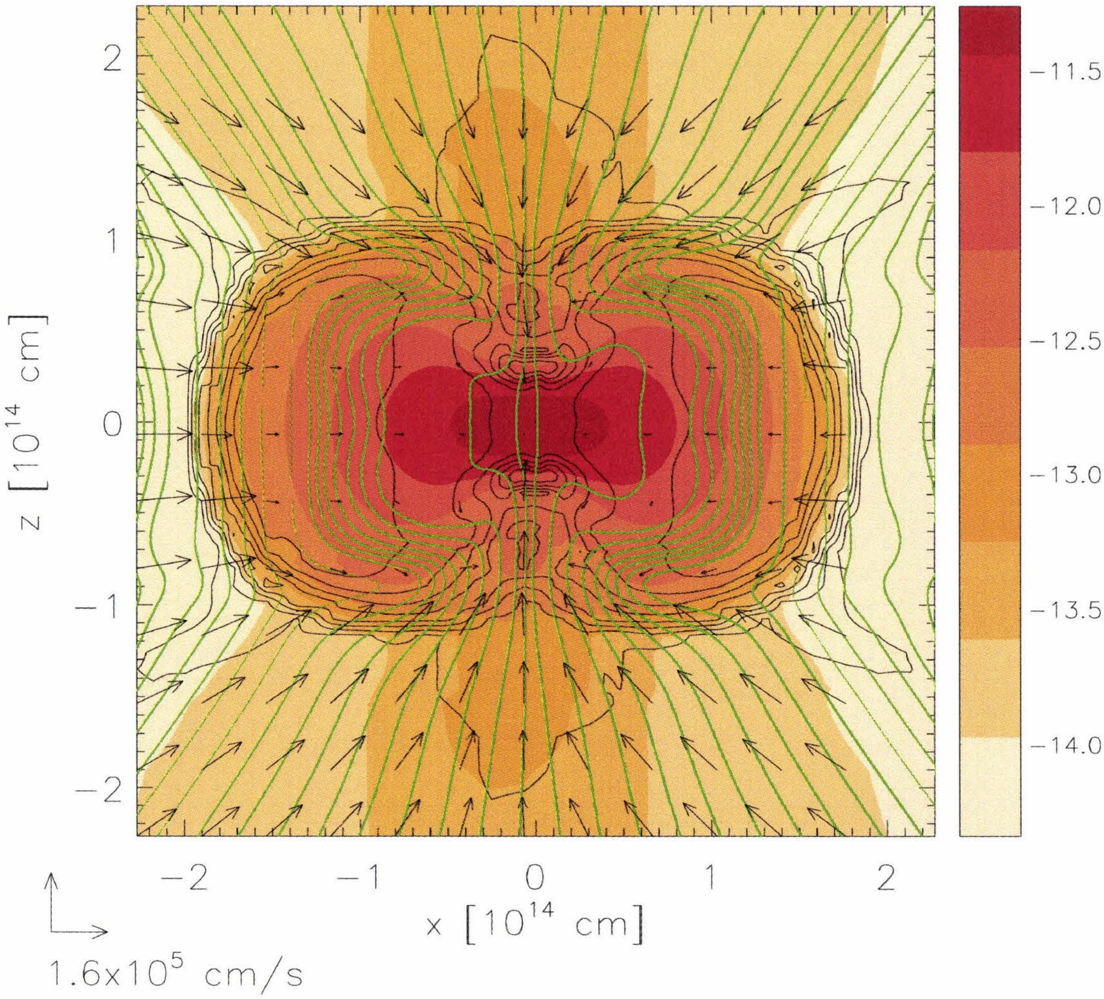

Figure 4.15: Density pseudocolor in the x-z plane (in g cm^{-3}) of the non-ideal disk of the high mass model. Graph properties are comparable to those in Figure 4.14. Note the puffy disk structure and dragged in field lines produced through effective ambipolar diffusion in the disk.

4.3.4 Earlier Than Expected Outflows

A surprising feature of the non-ideal collapse is the appearance of outflows that begin when central densities are only $n_c \approx 10^{12}$ cm^{-3}. Outflows in the ideal collapse will begin orders of magnitude *later* in central density, at $n_c \approx 10^{14}$ cm^{-3}. As magnetic coupling is presumed to be an important parameter in which to predict outflow generation, this comes as a surprise. In Figures 4.14 and 4.15 we see similar central density states of ideal and non-ideal collapses and we notice that the non-ideal collapse has begun launching outflows from the disk. This is hard to make out as outflow velocity vectors are small compared to the layered accretion speeds. We highlight the inner disk of the ambipolar collapse in Figure 4.17 so that this feature is more apparent. We "cut-out" infalling velocities which are too high to avoid saturating our image.

What becomes clear after analyzing the images is that layered accretion has created a very strong pinching effect, akin to the pinching seen in the ideal collapse. By the time outflows start in the ideal collapse, this pinching has become similarly pronounced (Figure 4.16). It is this pinching that provides effective pressure amplification to support a magnetic tower effect (Lynden-Bell, 2003). In the case of magnetized layers and the dragging of field lines inwards, an even stronger pinching effect is produced than is seen in the ideal case (at the same central density, Figures 4.14 and 4.15). Thin disk layers drag field lines as opposed to the whole disk midplane. Also, the pinching phenomena occurs twice, appearing on each layer instead of in the midplane. This supports the generation of a magnetic tower outflow. Outflows with speeds of 0.25 km s^{-1} are seen in the non-ideal case at central densities of $n = 10^{12}$ cm^{-3}, though in the early stages. Stronger outflow motions of 0.4 km s^{-1} are generated by the ideal collapse but at later times wherein central densities reach $n = 10^{15}$ cm^{-3}.

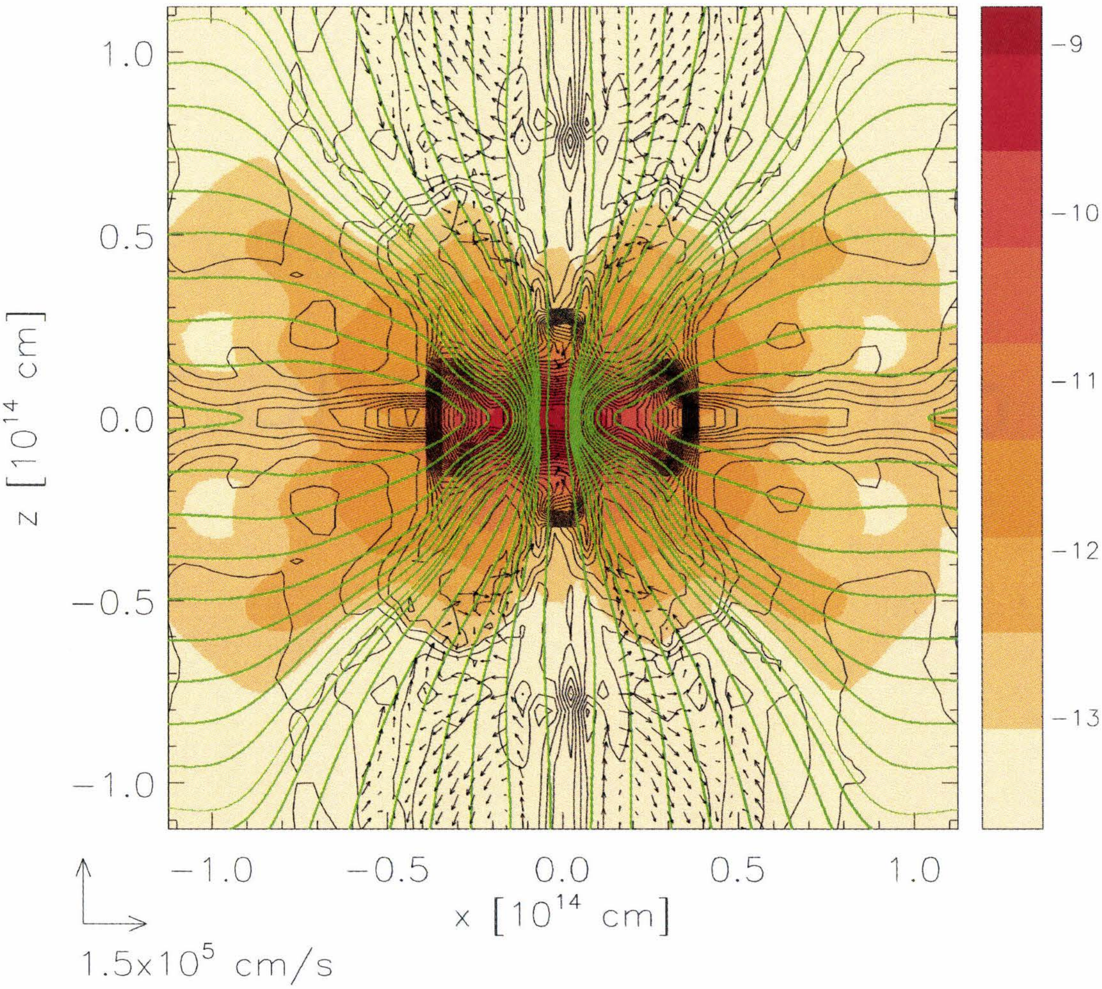

Figure 4.16: Launch of magnetic tower outflow in the ideal collapse of the high mass model. The later evolution of the upper panel of Figure 4.14. We see the launching of the magnetic tower through the inflating of vertical disk shocks (temperature contours), in much the same way outflows were launched from the low mass model in Banerjee & Pudritz (2006) . Sharp vertical pressure gradients are apparent following the outflow bubble which extends out of the graph to a height of 10 AU (and rising), consistent with the magnetic tower mechanism. Large infall velocities are omitted, while small outflow velocities of 0.4 km s^{-1} are shown. As central densities evolve outflow velocities will reach upwards of 4 km s^{-1} (Banerjee & Pudritz, 2007). The central density is $n_c \approx 10^{15}$ cm^{-3}.

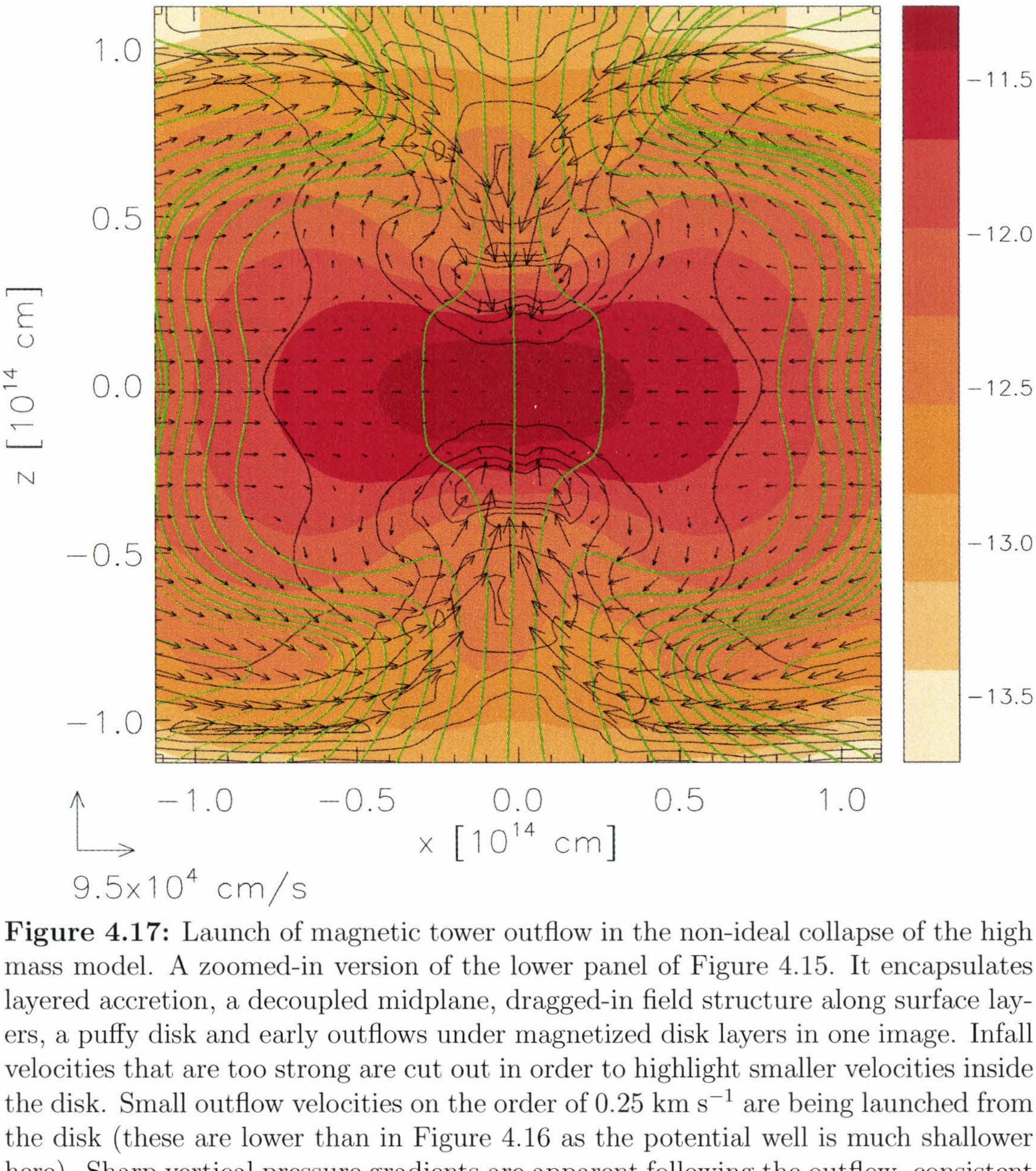

Figure 4.17: Launch of magnetic tower outflow in the non-ideal collapse of the high mass model. A zoomed-in version of the lower panel of Figure 4.15. It encapsulates layered accretion, a decoupled midplane, dragged-in field structure along surface layers, a puffy disk and early outflows under magnetized disk layers in one image. Infall velocities that are too strong are cut out in order to highlight smaller velocities inside the disk. Small outflow velocities on the order of 0.25 km s^{-1} are being launched from the disk (these are lower than in Figure 4.16 as the potential well is much shallower here). Sharp vertical pressure gradients are apparent following the outflow, consistent with the magnetic tower mechanism.

In Figures 4.18 and 4.19 we show the pressure of the magnetic tower flow through the distribution of the toroidal field components. In the ideal case these components are strictly confined through ram pressure, indicating that the magnetic tower has not yet launched. In the non-ideal case effective ram pressure on the field is decreased due to ambipolar diffusion, and the wound-up disk field is able to push out into the ambient medium. This is akin to the ideal magnetic tower mechanism, which describes a strong toroidal field build up in the disk, eventually pushing outwards with a sharp pressure gradient and remaining collimated due to ram pressure. One can relate (spatially) the ambient B_ϕ along diagonal directions seen in Figure 4.19 with the small outflow intensity seen in Figure 4.17. It is also interesting to note that while a magnetic tower mechanism has been established earlier, the overall toroidal field strength of the non-ideal disk is generally weaker than that of the ideal disk. Values at about 10 AU are 0.04 G in the non-ideal disk in comparison to 0.1 G in the ideal disk.

The question that remains however is, can a collapse with a finite conductivity produce a magnetic tower mechanism? Theoretical work by (Lynden-Bell, 2003), which described how pressure gradients worked in a magnetic tower, excluded a finite conductivity. The toroidal field is wound up in the disk until it can no longer be contained. Bubbles dominated by magnetic pressure then push out into the ambient medium taking gas with them. Continued rotation of the disk drives the tower ever higher while ram pressure confines its collimation. The ideal collapse will eventually use this mechanism in generating its outflows (Figure 4.16), and has been recognized as a outflow mechanism in previous studies (Banerjee & Pudritz, 2006).

We show the beginnings of this mechanism in our low mass model (under less resolution than our high mass model). Magnetized bubbles have extended into the

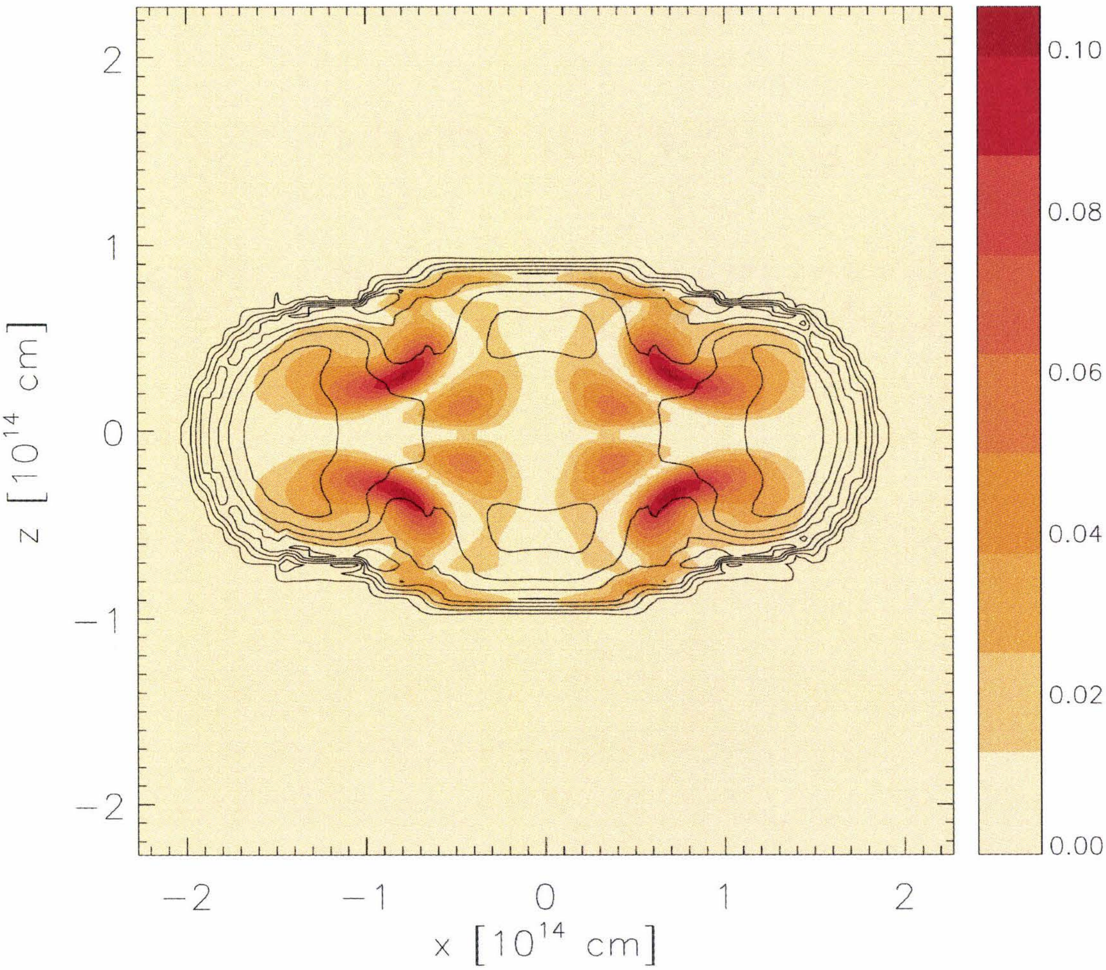

Figure 4.18: Distribution of B_ϕ in the disk of the ideal collapse of the high mass model. Temperature contours are every 10 K with central densities of 1.7×10^{12} cm^{-3}. This graph can be compared to the non-ideal case in Figure 4.19. The toroidal field is strictly confined to the disk in the ideal case, while it can slip out in the ambipolar diffusion case.

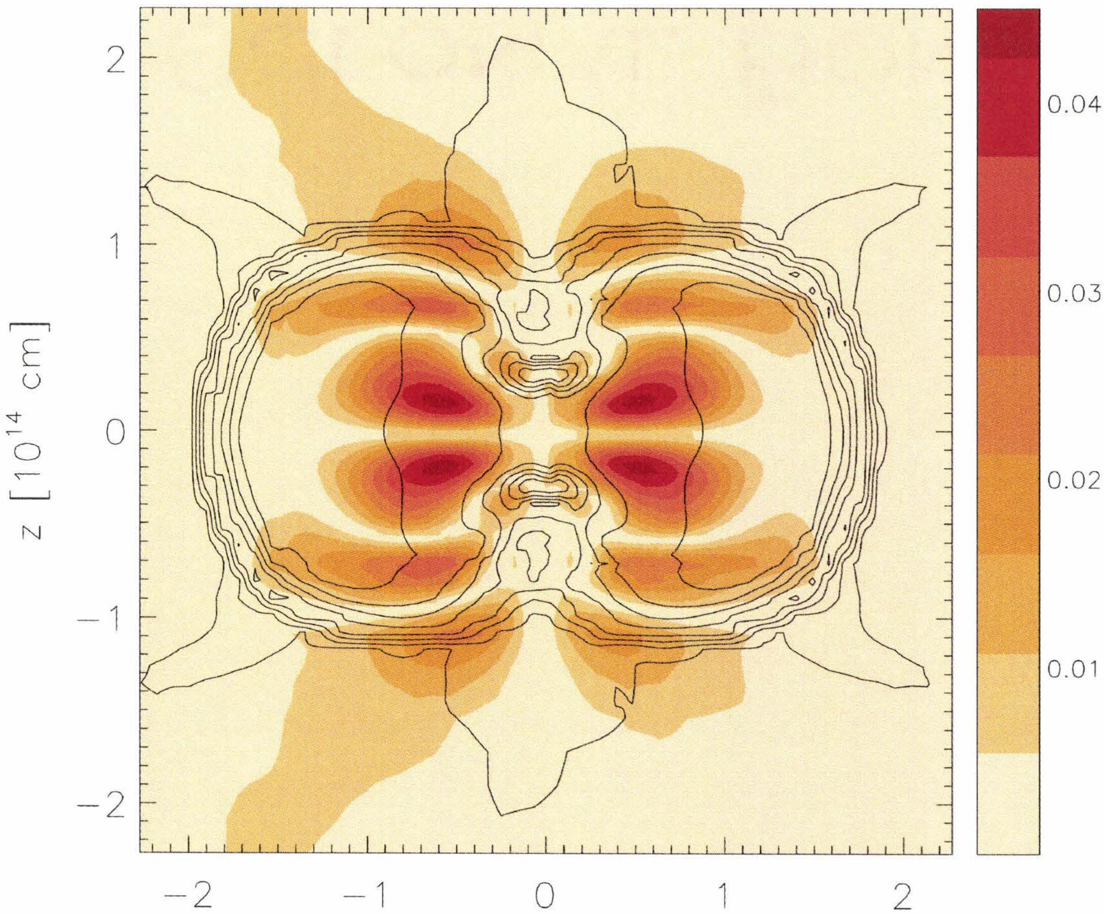

Figure 4.19: Distribution of B_ϕ in the disk of the non-ideal collapse of the high mass model. Graph properties are similar to those described in Figure 4.18. Note the established magnetic tower outflow through the ejection of toroidal magnetic field from the disk into the ambient medium.

ambient medium, more so in the ambipolar case. In the corresponding ideal case outflows are just beginning. The disks are dramatically different due to the increased fragmentation in the non-ideal model.

4.3.5 On Proto-Dead Zones and Decoupled Zones

One of our numerical goals was to present data of a self-consistently formed dead zone from the natural collapse of a Bonnor-Ebert Sphere. As local thermal velocities are greater than Alfvén velocities by a factor of 2-3 in our simulations, and angular velocity profiles decrease with radius, our collapsing clouds satisfy the weak field and the rotational conditions necessary for MRI turbulence to persist. Our simulation however won't be able to view the actual MRI turbulence as we observe only a few rotations in our simulations. In this case, we rely on the work from other authors studying local effects of MRI turbulence in accretion disks to understand how it is damped (Kunz & Balbus, 2004; Fleming & Stone, 2003; Balbus & Hawley, 1998).

Provided the ideal conditions, resistive MHD effects can diffuse field gradients faster than the growth conditions for MRI turbulence. This leads to regions in the disk (in particular the disk midplane) which are commonly known as *dead zones* (Gammie, 1996). Due to the lack of MRI, these zones are void of turbulence-induced viscosity. Disk viscosity is important to planet formation models, particularly migration models. These models show that the size of the dead zone controls the gap size a planet can open in its parent disk, thus controlling it's final mass (Matsumura & Pudritz, 2005). It also plays a role in stopping a migrating planet from falling into its parent star. In this sense we are interested in any initial conditions a dead zone may have. To study this we use a very global model of a collapsing Bonnor-Ebert sphere and our results are self-consistent in this sense. This global approach is complimentary to a

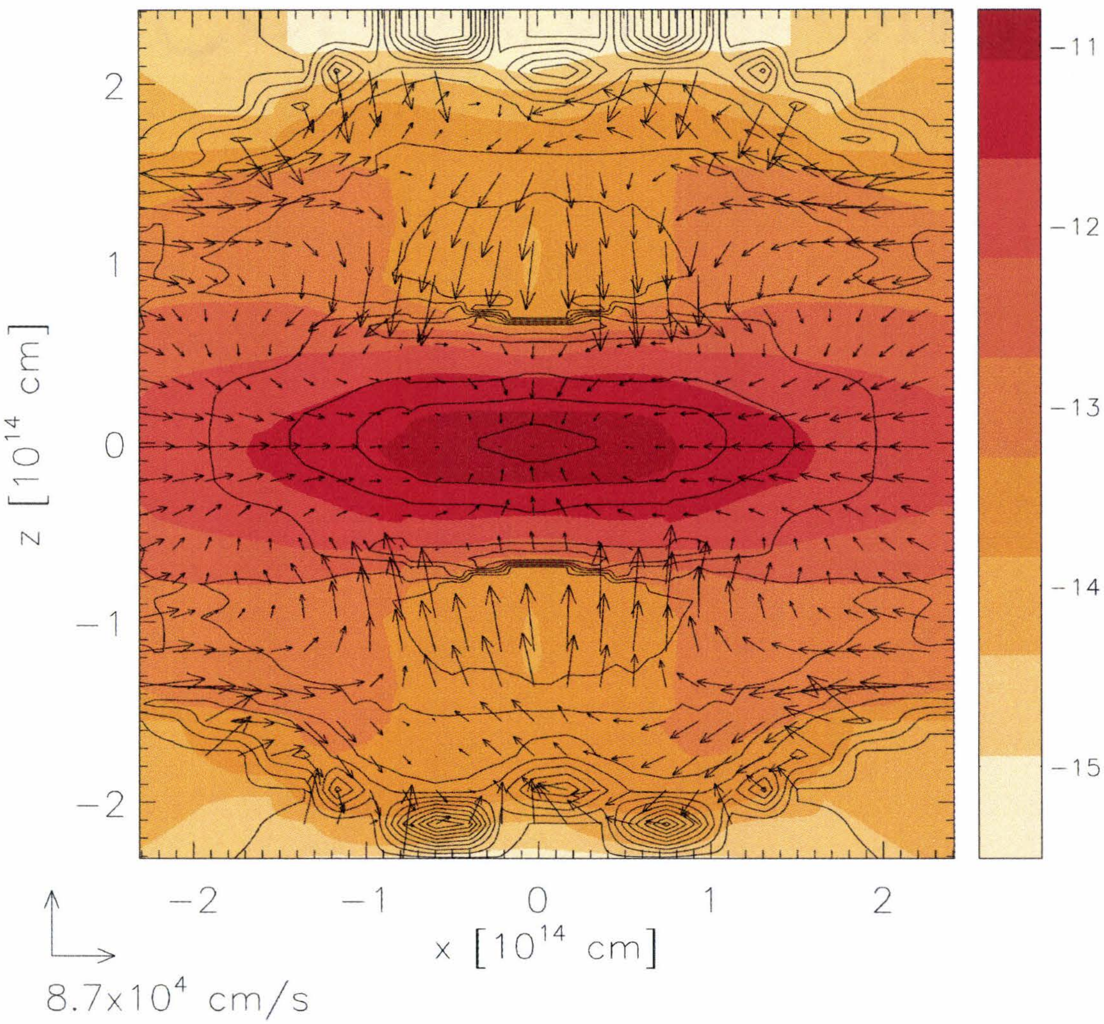

Figure 4.20: Outflows from the ideal low mass model collapse are only just beginning, as compared to stronger outflow motions seen in the non-ideal case portrayed in Figure 4.21. The pseudocolor is mass density, with temperature contours every $10^{0.4}$ K. We have cutoff velocity vectors larger than 1 km s^{-1} as vertical accretion would saturate the graph (thus the lack of vectors above and below the disk). This image corresponds to the upper image given in the section on fragmentation seen in Figure 4.2

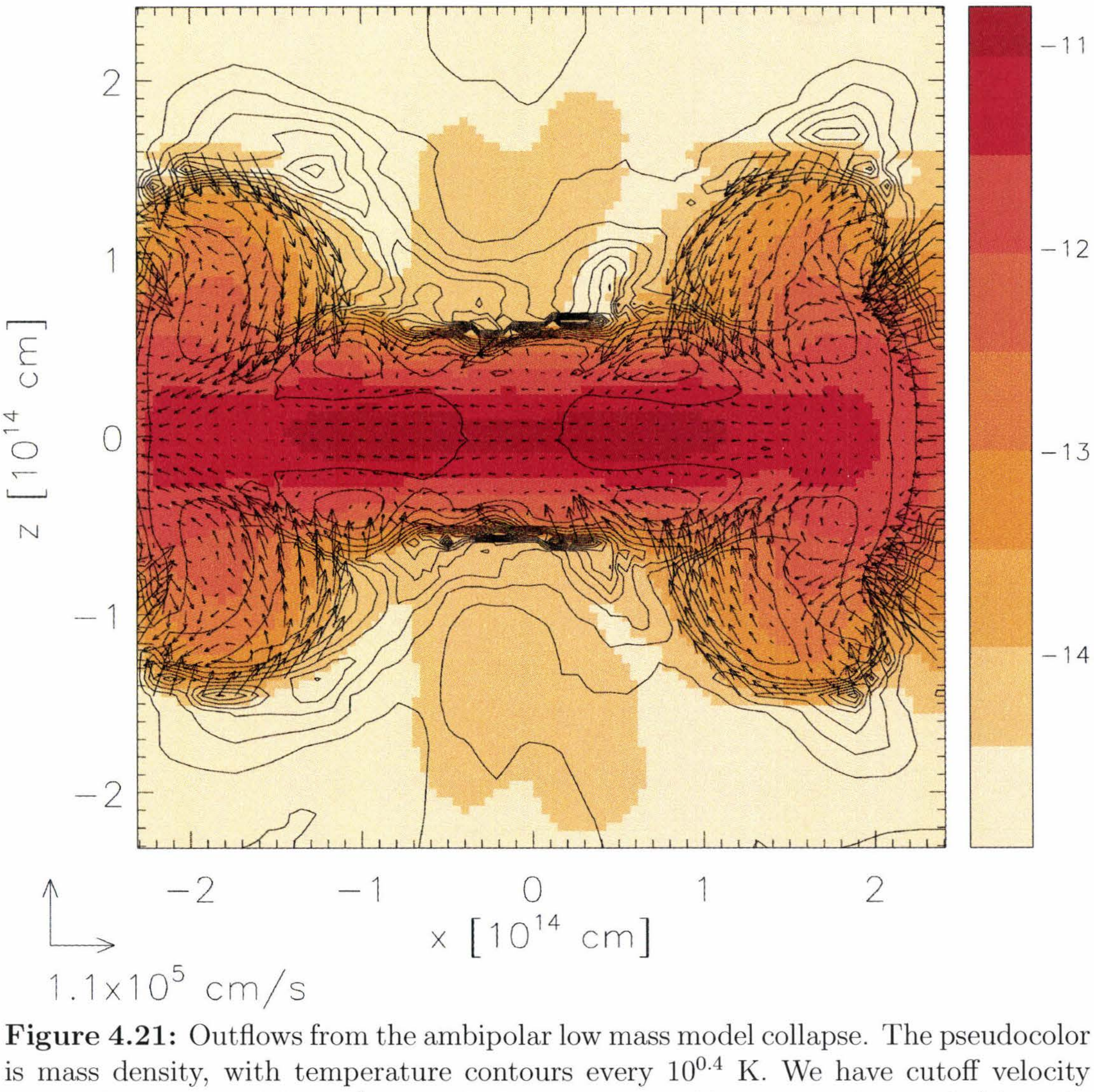

Figure 4.21: Outflows from the ambipolar low mass model collapse. The pseudocolor is mass density, with temperature contours every $10^{0.4}$ K. We have cutoff velocity vectors larger than 1 km s^{-1} as vertical accretion would saturate the graph (thus the lack of vectors above and below the disk). This image corresponds to the non-ideal fragmentation seen in Figure 4.3 which explains the very distorted disk shape. Gas is beginning to separate into two clumps about the center.

more efficient method which studies only very local models of disks through many rotational periods (e.g., Fleming & Stone, 2003).

Dead zones due to ambipolar diffusion are different than the classical model in which Ohmic diffusion is the dominating form of magnetic field dissipation. This makes sense if one is studying a Keplerian disk where densities are high and Ohmic terms become more important (Desch & Mouschovias, 2001). Our dead zone would be governed by ambipolar diffusion rather than Ohmic diffusion. Also, rotational velocities are sub-Keplerian (at about 0.4 $v_{\rm kepler}$ during this stage of the collapse). This allows the dead zone to still accrete while not being affected directly by the magnetic field. However, accretion is very much layered in intensity, as we will discuss later. Figures 4.14 and 4.15 shows xz slices of the cloud at the disk level, comparing ideal and non-ideal states at $n_{core} = 1.7 \times 10^{-12}$ cm^{-3} respectively. As our ionization goes as $x_{\rm ion} \propto n_n^{-1/2}$, we expect the disk midplane to be more decoupled than its shocked layers due to its Gaussian density distribution with height (as shown in Banerjee et al. (2004)). The decoupling of the magnetic field is evident in the non-ideal disk as the field lines are severely dragged along the ionized shocked layers and left behind in the disk midplane. Immediately we have an idea of the dead zone's possible extent.

Kunz & Balbus (2004) have shown analytically that the growth rate of MRI is severely damped for $\Omega/(\gamma_{AD}\rho_i) > 1$ in an ambipolar diffusion dominated disk. We plot our results in 4.22, showing that MRI can indeed propagate almost anywhere in this disk at this early stage and that no dead zone is formed despite the severe magnetic decoupling evident in 4.15. We note, however, that as we move into denser regions of the collapse, that are far better shielded from cosmic rays, Ohmic dissipation will become important. We leave this for future work to consider.

We note however that if we had included shielding of cosmic rays (cosmic rays

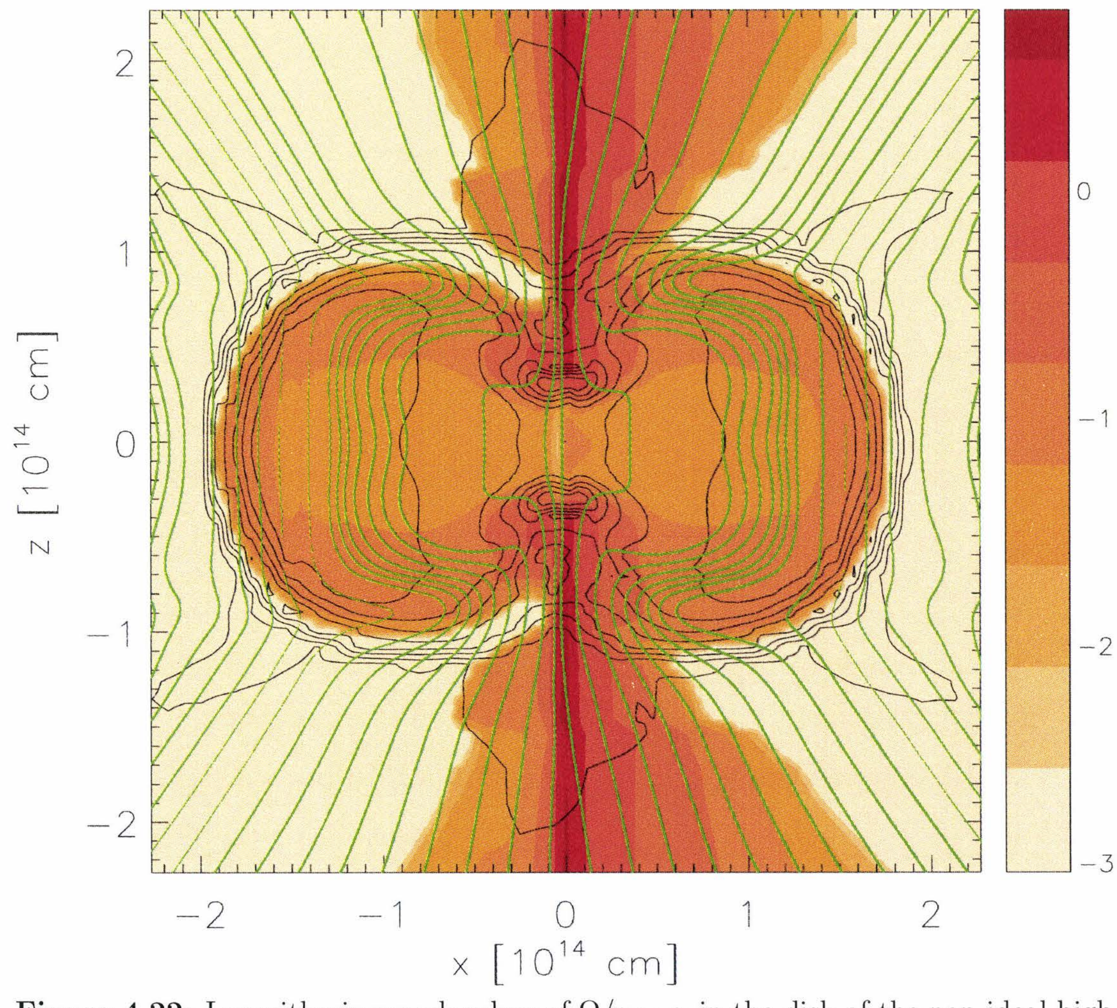

Figure 4.22: Logarithmic pseudocolors of $\Omega/\gamma_{AD}\rho_i$ in the disk of the non-ideal high mass model. Temperature contours are every 10 K and magnetic field lines are in green for reference to Figure 4.15. This is also the same state as in the non-ideal run of Figure 4.22. We note that the disk is not quite dead all to MRI turbulence as studied by Kunz & Balbus (2004) as it is mostly less than 1 and with a very even distribution in the disk (thus the lack of colored features).

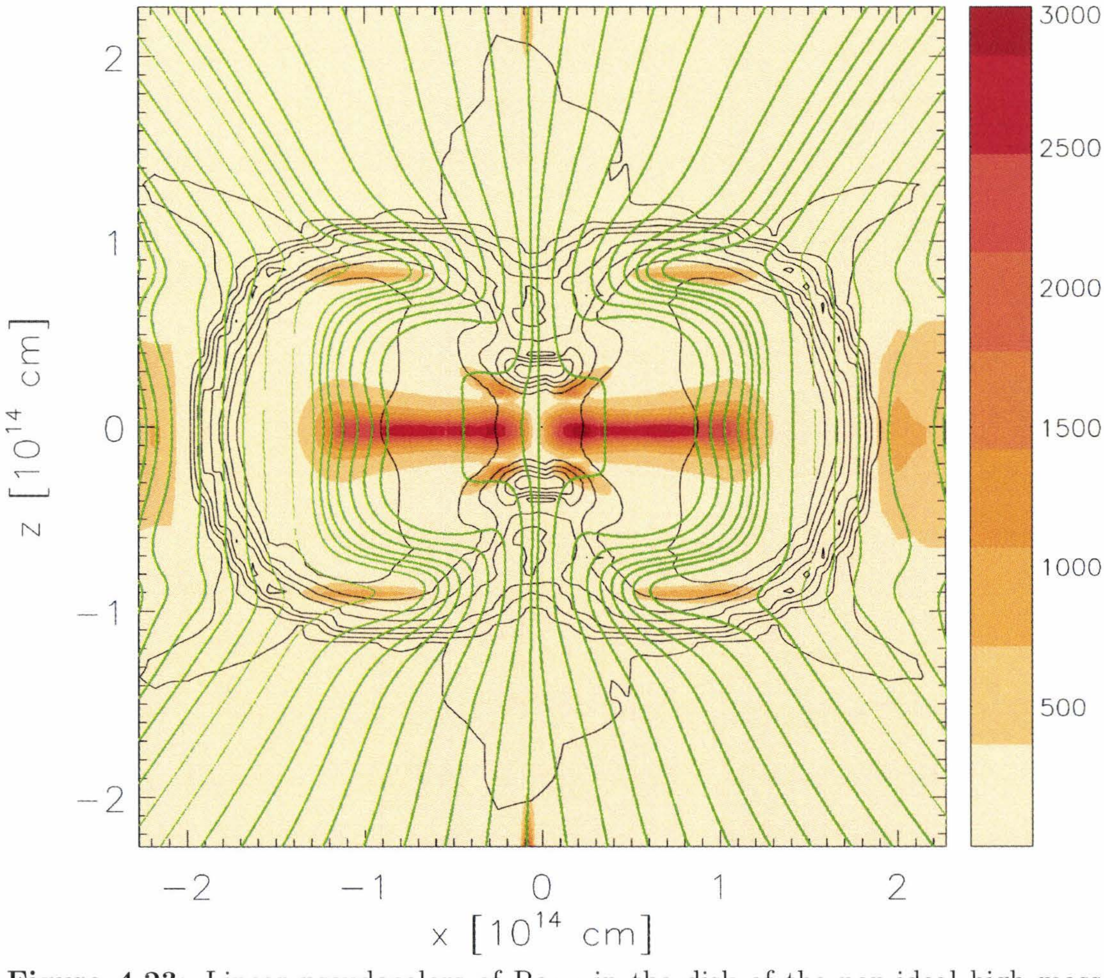

Figure 4.23: Linear pseudocolors of $\mathrm{Re_{AD}}$ in the disk of the non-ideal high mass model. Temperature contours are every 10 K and magnetic field lines are in green. This is also the same state as in the non-ideal run of Figure 4.15 . We see the opposite of a decoupling zone in the midplane and just under the coupled layers. This graph is telling us that diffusion in the disk midplane is orders of magnitude high than anywhere else in the cloud. This would mean that the cloud is most like the ideal simulation in the disk midplane, which it clearly isn't.

penetrate only to column densities of 96 g cm^{-2} (Umebayashi & Nakano, 1981)), the dead zone would have been formed. First, from Figure 4.4 we see that column densities of a few hundred g cm^{-2} are achieved by both runs of the high mass model. Dead zones with only ambipolar diffusion require $\Omega/\gamma_{\rm AD}\rho_i > 1$, which is very quickly achieved if ρ_i suddenly drops to very small values. In our case we have $\rho_i \propto \rho_n^{1/2}$, which makes dead zone creation quite difficult through chemistry alone. This will be an interesting avenue for future research, however we predict dead zones in Class 0 objects at column densities of about 100 g cm^{-2} and distances of (25-60) AU, by following the power-law evolution of our surface density profiles (Figure 4.4).

Despite the fact that our approximations do not really allow for the appearance of a dead zone, we still observe layered accretion and dragging of magnetic field lines by well-coupled disk layers. Clearly there is a central region of the accretion disk which is not well coupled to the accretion disk, starting at about 20 AU (as suggested by Desch & Mouschovias (2001)). The classical approach is to use a diffusive method. If the diffusion speed ($\eta_{\rm AD}/L$, for some scale length L) over the disk is faster than the dragging in of magnetic flux (say the flow velocity, $v_{\rm flow}$), but not faster we can explain the decoupling. We quantify this by defining a type of 'Reynolds number',

$$\mathrm{Re}_{\rm AD} = \frac{v_{\rm flow} L}{\eta_{\rm AD}},$$

which describes the coupling of the field to the gas. The typical length scale L is taken to be the radius of the disk, 2.0×10^{14} cm. For $\eta_{\rm AD} > v_{\rm flow}L$, diffusion is too quick for the gas to drag the field forward, and flux is left behind (at the cost of frictional heating). We provide a 2D plot of $\mathrm{Re}_{\rm AD}$ in the x-z plane (Figure 4.23), clearly showing the largest values in the midplane of the disk, with a height of about 2-3 AU and an extent of about 10 AU. This is opposite of what our intuition is telling us: *ambipolar diffusion is strongly damped in the disk midplane, more than anywhere* *else in the collapsing cloud.* But this cannot be true, as we clearly observe field lines in the disk being left behind[2]. What has gone wrong?

It is important to note that ambipolar diffusion is not a purely diffusive process. One can split Equation (4.6) up into diffusive and non-diffusive terms (Brandenburg & Zweibel, 1994),

$$\begin{aligned}\frac{\partial \boldsymbol{B}}{\partial t} &+ \boldsymbol{\nabla} \cdot (\boldsymbol{uB} - \boldsymbol{Bu}) + \boldsymbol{\nabla} \\ &- \boldsymbol{\nabla} \times (\eta_{AD} \boldsymbol{\nabla} \times \boldsymbol{B} - \mu_0 \beta_{\mathrm{AD}} (\boldsymbol{J} \cdot \boldsymbol{B}) \boldsymbol{B}),\end{aligned} \tag{4.10}$$

where the second last term on the right is the diffusive term and the last term is the non-diffusive term. The magnitudes of these two vectors are plotted in Figures 4.24 and 4.25 and it is evident that they are of equal importance inside the disk. It is also apparent that at disk layers influx of magnetic field is about 100 times as strong as in the midplane, which explains the lagging of field lines there as due to ambipolar diffusion.

In lieu of this, we require a non-diffusive, and more physical, argument in which to classify decoupling. We borrow an idea from C-shock theory which states that $v_s << v_{A_i} = B/(4\pi\rho_i)^{1/2}$ in order for a C-shock to form (Draine, 1980), where v_s is the shock velocity and v_{A_i} is the ion Alfvén speed. This would require the infall speed be much less than the speed in which compression information travels along the field lines. In our case we suggest decoupling occurs for:

$$v_{\text{flow}} < \alpha v_{A_i}, \tag{4.11}$$

where $\alpha = 10^{-4.5}$ from observing Figure 4.26. In the Figure 4.26 we can also observe the strongest 'lagging' of field lines corresponding directly with the lowest values of

[2]Note that we have tried a number of different combinations of possible parameters for $v_f low$ and L, each producing a similar conclusion: diffusion is severely damped in the disk midplane.

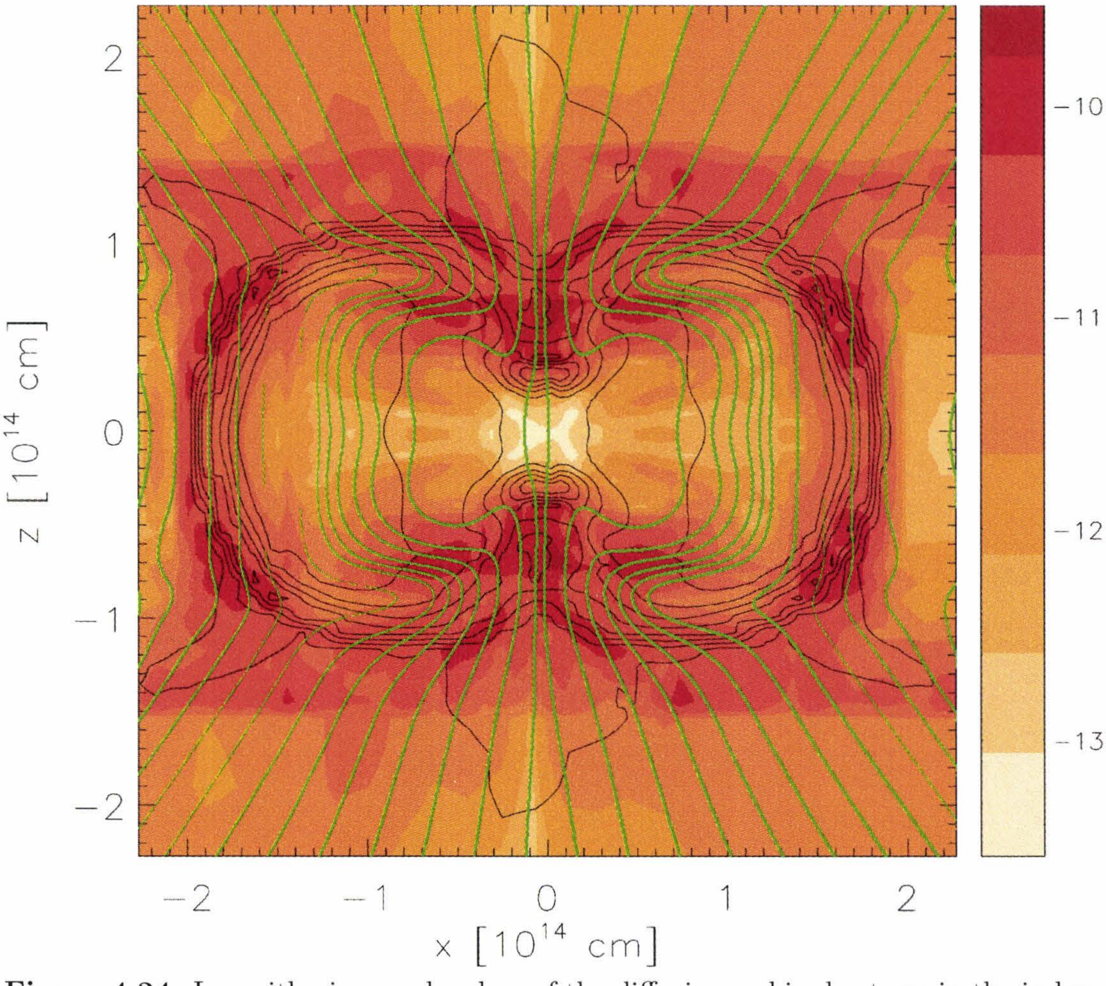

Figure 4.24: Logarithmic pseudocolors of the diffusive ambipolar term in the induction equation, $|\boldsymbol{\nabla} \times (\eta_{\mathrm{AD}}\boldsymbol{J}/\mu_0)|$ in the disk of the non-ideal high mass model. Note that $\boldsymbol{J} = \frac{1}{\mu_0}\boldsymbol{\nabla} \times \boldsymbol{B}$ and plotted units are logaritmic G s^{-1}. Temperature contours are every 10 K and magnetic field lines are in green for reference to Figure 4.15. Note maximal values of the logarithmic scale in comparison to Figure 4.25 and the high contrast between disk layer and midplane values.

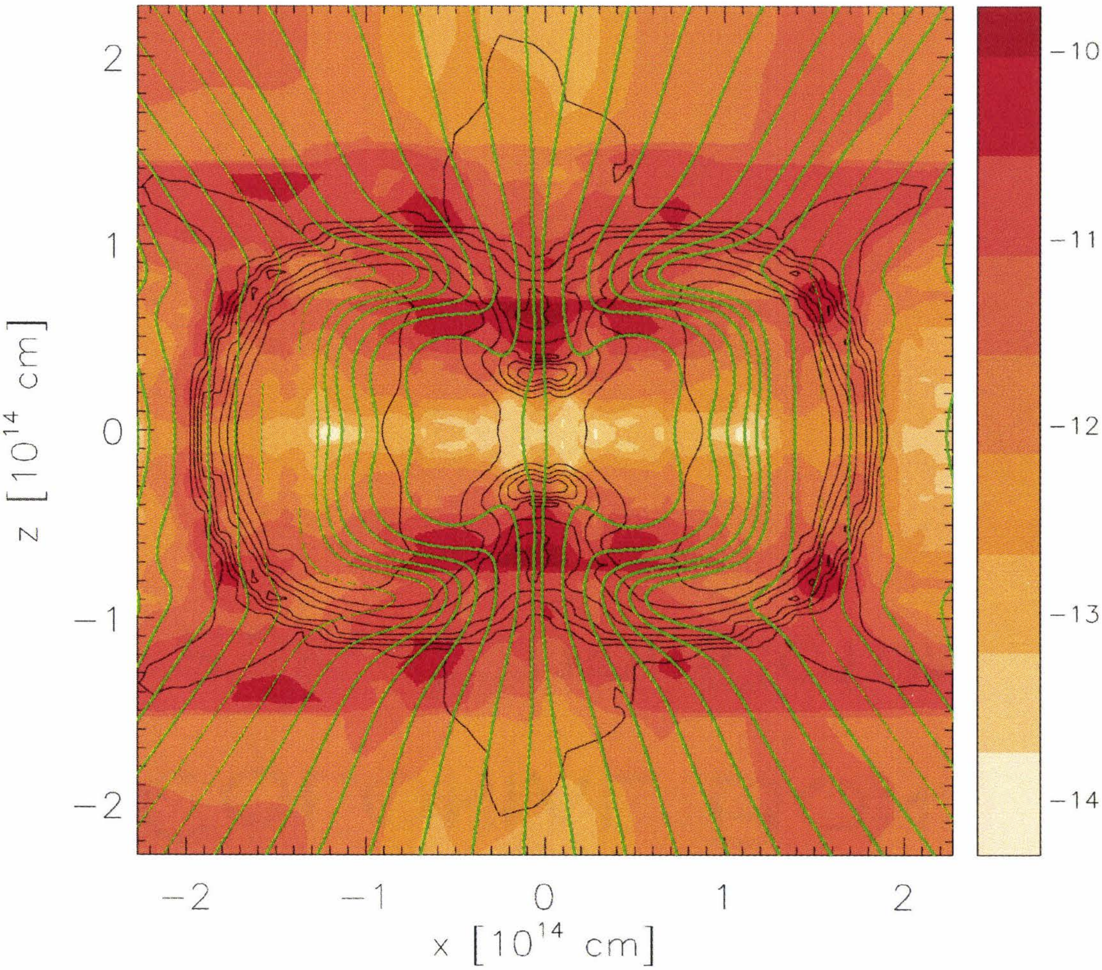

Figure 4.25: Logarithmic pseudocolors of the non-diffusive ambipolar term in the induction equation, $|\boldsymbol{\nabla} \times [\mu_0 \beta_{\mathrm{AD}}(\boldsymbol{J} \cdot \boldsymbol{B}) boldsymbol B]|$ in the disk of the non-ideal high mass model. Note that $\boldsymbol{J} = \frac{1}{\mu_0}\boldsymbol{\nabla} \times \boldsymbol{B}$ and plotted units are logarithmic G s^{-1}. Temperature contours are every 10 K and magnetic field lines are in green for reference to Figure 4.15. Note maximal values of the logarithmic scale in comparison to Figure 4.24 and the high contrast between disk layer and midplane values.

this ratio. Slight dragging of the field line in the midplane also corresponds with a slight local increase of this ratio. Physically, we can interpret this definition as saying that a certain inflow velocity is needed to sufficiently pull in field lines. Finally, we observe a *decoupled zone* which has a radial extent of about 10 AU and a height of 6 AU, in the disk.

This all fits very clearly into the picture we have of layered accretion along coupled layers where v_{flow}/v_{A_i} is orders of magnitude smaller than in the disk midplane.

4.4 Conclusions

We summarize the results we have presented in the previous sections:

- High mass accretion rates persist, on the order of $\dot{M}_{\text{max}} = 10^{-3}$ $M_\odot$ yr^{-1}. These rates are driven to higher values by effective drift heating evident at 100 AU.

- The extraction of angular momentum by magnetic torque is still efficient at extracting angular momentum from the non-ideal collapsing cloud, though it takes a little longer to carve out the same angular momentum distribution as seen in the ideal collapse. This aids in driving high accretion rates.

- The effects of drift heating are seen to make important contributions to the collapse on both large scale of 1000 AU(Figure 4.4) and small scales of 10's of AU (Figure 4.15). The effects are a large scale C-shock with temperatures that are nearly twice as high at 177 K as their ideal counterparts (Figure 4.9), and a puffy inner disk disk.

- Magnetic braking is seen to be 3/4 as effective at extracting rotational energy with ambipolar diffusion than without through the collapse of our B68 model.

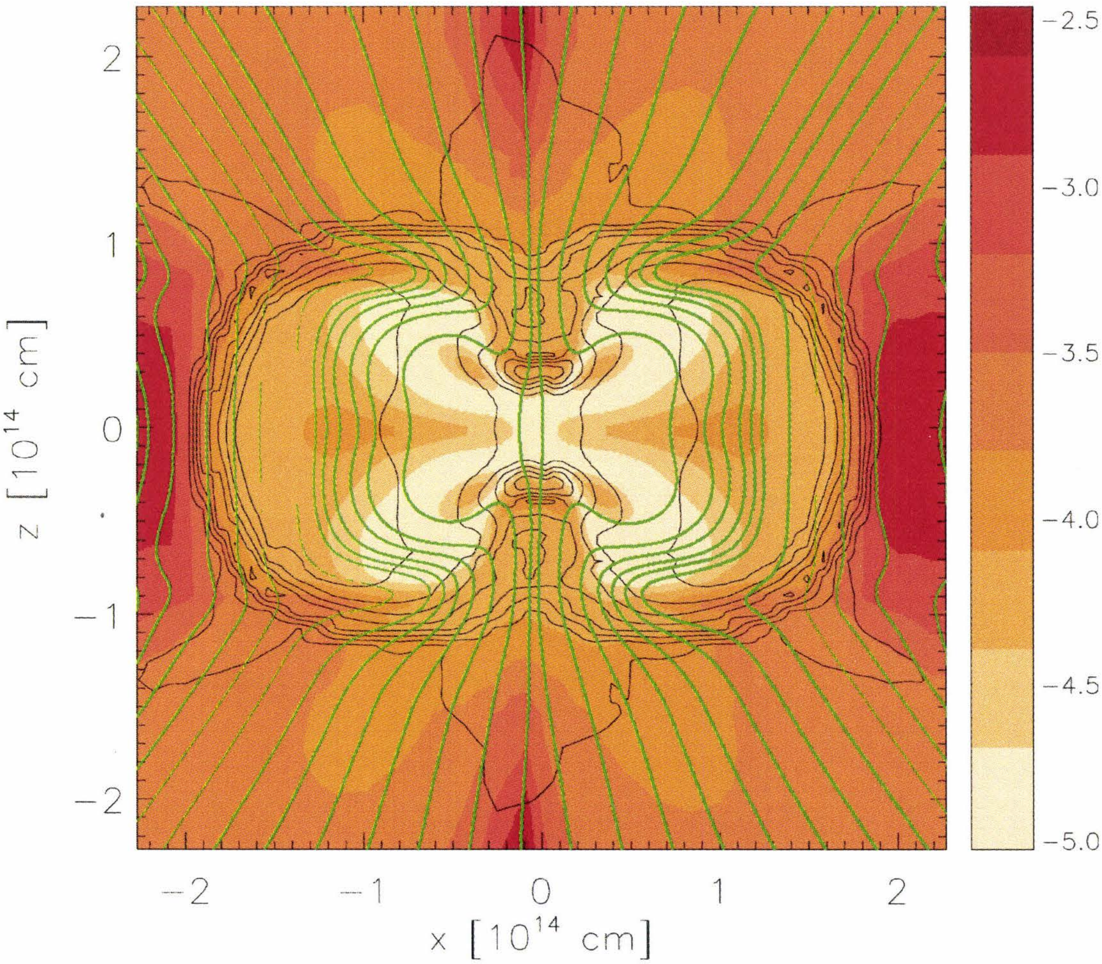

Figure 4.26: Linear pseudocolors of v_{flow}/v_{A_i} in the disk of the non-ideal high mass model. Temperature contours are every 10 K and magnetic field lines are in green. We see the decoupling zone in the midplane and just under the coupled layers such that the critical ratio for dragging is observed to be about $10^{-4.5}$. Note how well the lagging and dragging of field lines corresponds to low and high values of the pseudocolor respectively. Values lower than 10^{-5} are cut off.

- The rate of fragmentation in the disk is increased by ambipolar diffusion due to the reduced magnetic pressure support within it. It is seen to approach more hydrodynamic results (Banerjee et al., 2004).

- The build up of magnetic flux is only slightly weaker in the ambipolar collapse than in the ideal collapse, with field strengths of 0.032 G reached at the end of our simulation. These values are only half as strong as values reached in ideal simulation at similar central column densities (300 g cm^{-2}).

- Outflows begin earlier in the ambipolar diffusion collapse as ram pressure is less effective at trapping the wound up toroidal field in the disk. The mechanism for outflow generation is recognized as a magnetic tower, as in the ideal case. Outflow velocities of 0.26 km s^{-1} are seen in our ambipolar diffusion collapse in comparison to velocities of 0.4 km s^{-1} seen in the corresponding ideal outflow. These are early outflows, limited by the small diffusive timestep. As the potential well grows, outflows in the ideal case have been seen to rise to 4 km s^{-1} (Banerjee & Pudritz, 2007).

- A decoupled zone forms in the disk midplane which has a height of 6 AU and a radial extent of 10 AU and involves a equal contribution of diffusive and non-diffusive ambipolar diffusion. In this zone gas cannot effectively drag in magnetic flux, and field lines are seen to lag behind while actively coupled, ionized layers drag them in. We have shown the criterion for this zone to be formed is that $v_{\text{flow}} < 10^{-4.5} v_{A_i}$. This creates a strong pinching effect that is responsible for amplifying the magnetic and aiding the early outflows.

- The formation of an early dead zone mediated by ambipolar diffusion is possible in the early collapse phase, though dependent on shielding of cosmic rays by gas densities in excess of 96 g cm^{-2}. If we included this effect into our simulation, we predict we would obtain a dead zone with a radial extent of (20-60) AU.

We note that our results are limited by the chemistry that we have implemented. Our approximation is only accurate to densities of 10^{10} cm^{-3} while we reach maximum densities of 10^{12} cm^{-3}. In this region the charged grains have been predicted to be the principal charge carrier (Tassis & Mouschovias, 2007b; Nakano et al., 2002) and future work should include these effects. This may change how the field is built up through disk accretion. Also important is the inclusion of cosmic ray shielding for column densities that are greater than 96 g cm^{-2}. This is a vital ingredient for accurately capturing the early dead zone that should form in the collapse.

A final note for future work would be the inclusion of other resistive magnetic processes like Ohmic dissipation which has been shown to be important at similarly high densities (Desch & Mouschovias, 2001). Although we do not consider these effects, this work offers a good first step in that direction, offering key insight into the relevant problems at hand.

Chapter 5

Future Work

The main issues with any approximation of ambipolar diffusion lie in how the chemistry is treated. This is the case in our work, where we have used only the simplest approximation for the ionization (see §2.1.1). This $n_i \propto n_n^{1/2}$ law persists only up to total gas densities of about 10^{10} cm^{-3}, where charged grains become the principal charge carrier. A full treatment of this will be necessary in making more decisive statements on the results discussed in §4.4.

This may require a multi-fluid approach which conserves gas species mass individually through separate continuity equations. Frictional interaction forces are then added to the respective HD or MHD equations of motion for each species. To include a proper evolution of the charged species, one must include a separate set of equations which treat mass transfer and the chemistry. This is effectively accomplished by solving the equilibrium equations between known species, and can become quite complicated, depending on the detail that one wishes to achieve (e.g. Tassis & Mouschovias, 2007b; Nakano et al., 2002).

The benefit of the multi-fluid approach may also lie in increased timesteps, with the "heavy-ion approximation" of Li et al. (2006) claiming shorter timesteps by factors of 10-100. We note that this must be weighed against the deficit of including chemistry and in calculating effectively twice the number of dynamical equations per timestep (or more, depending on the number of species in the gas), in addition to added frictional terms. It may prove more efficient to simply approximate the in-depth evolution of chemical species in a collapsing cloud from previous work (mentioned above), and apply this to the single fluid approximation. This would offer a computationally quick and simple method in which the low ionization regime of molecular clouds can be treated, though remaining unable to independently track charged species' distributions.

Also important at these high densities are the effects of Ohmic dissipation (Desch & Mouschovias, 2001). Machida et al. (2007) has already begun to investigate this in pre-Class 0 collapse down to the formation of disk winds and jets, though we believe their model of ohmic diffusivity is greatly exaggerated (i.e. it stems from the numerical collapse of an ideally coupled cloud). Self-consistent treatments of ambipolar diffusion with ohmic dissipation show the latter effect is important only at densities higher than 10^{10} cm^{-3} (Desch & Mouschovias, 2001). A module in FLASH applying Ohmic dissipation in the single fluid approximation has already been written (§3.1; though may need to be tested). Although we are interested in the effects of Ohmic dissipation on outflows from the disk, it will also play an interesting role in mediating the proto-dead zone that will form due to cosmic ray shielding (§4.3.5).

The shielding of ionizing radiation such as cosmic rays by dense disk layers is a very interesting phenomenon to model, as it has been shown to be a necessary ingredient into the formation of early dead zones in protoplanetary accretion disks (§4.3.5). The ionizing radiation can be approximated as emanating from the z-direction, aligned with the global field of the molecular cloud (as cosmic rays are charged particles).

Later, more complicated ionizing sources can be applied. The hard part may come in determining the column density of a given cell in a numerically inexpensive manner. Once this is known the application to the single fluid chemistry approximation is not necessarily straightforward. We have an equation for $\zeta(\Sigma)$ (section §2.1.1), though no clear method on how to translate this to ion density. An effective step function of sort can be used here as the decrease in ion density is expected to be exponential after column densities reach 96 g cm^{-3}, where various continuous transitions between the steps in the step function can be approximated.

Extensive testing of code was done with the knowledge that, as a general sub-module in FLASH, our ambipolar diffusion module can be extended to a virtually limitless number of applications, much in the same way the ZEUS ambipolar diffusion module developed by Mac Low et al. (1995) was used. Examples extend to any multi-dimensional MHD simulation that would benefit from the addition of ambipolar diffusion. This includes but is not limited to: MHD compressable turbulence models which study the large scale evolution of molecular clouds, local simulations of MRI turbulence in accretion disks, magnetic jets simulations which study the launching of jets from protoplanetary disks or further applications to the pre-Class 0 collapse phase discussed in Chapter 4 (such as using turbulent filamentary initial conditions (Banerjee et al., 2006)). We note that for some applications, densities remain below 10^{10} cm^{-3} and even our simple chemical approximation can be carried over.

There are many interesting avenues now open due to the work presented in this thesis. We have used our numerical developments to investigate interesting avenues in the pre-Class 0 collapse of a Bonnor-Ebert sphere. We hope that many interesting physical discoveries are subsequently made from the work established herein.

Bibliography

Allen, L., Megeath, S. T., Gutermuth, R., Myers, P. C., Wolk, S., Adams, F. C., Muzerolle, J., Young, E., & Pipher, J. L. 2007, in Protostars and Planets V, ed. Reipurth, B. and Jewitt, D. and Keil, K., 361–376

Alves, J. F., Lada, C. J., & Lada, E. A. 2001, Nature, 409, 159

Balbus, S. A. 2003, ARA&A, 41, 555

Balbus, S. A. & Hawley, J. F. 1991, ApJ, 376, 214

—. 1998, Reviews of Modern Physics, 70, 1

Banerjee, R. & Pudritz, R. E. 2006, ApJ, 641, 949

—. 2007, ApJ, 660, 479

Banerjee, R., Pudritz, R. E., & Anderson, D. W. 2006, MNRAS, 373, 1091

Banerjee, R., Pudritz, R. E., & Holmes, L. 2004, MNRAS, 355, 248

Basu, S. & Mouschovias, T. C. 1994, ApJ, 432, 720

Bate, M. R., Bonnell, I. A., & Price, N. M. 1995, MNRAS, 277, 362

Bonnor, W. B. 1956, MNRAS, 116, 351

Brandenburg, A. & Zweibel, E. G. 1994, ApJ, 427, L91

Chini, R., Hoffmeister, V., Kimeswenger, S., Nielbock, M., Nürnberger, D., Schmidtobreick, L., & Sterzik, M. 2004, Nature, 429, 155

Ciolek, G. E. & Basu, S. 2006, ApJ, 652, 442

Dalgarno, A. 2006, Proceedings of the National Academy of Science, 103, 12269

Desch, S. J. & Mouschovias, T. C. 2001, ApJ, 550, 314

Donati, J.-F., Paletou, F., Bouvier, J., & Ferreira, J. 2005, Nature, 438, 466

Draine, B. T. 1980, ApJ, 241, 1021

—. 1986, MNRAS, 220, 133

Ebert, R. 1955, Zeitschrift fur Astrophysik, 37, 217

Elmegreen, B. G. 1979, ApJ, 232, 729

Elmegreen, B. G. & Scalo, J. 2004, ARA&A, 42, 211

Falle, S. A. E. G. 2003, MNRAS, 344, 1210

Fiedler, R. A. & Mouschovias, T. C. 1993, ApJ, 415, 680

Fleming, T. & Stone, J. M. 2003, ApJ, 585, 908

Fleming, T. P., Stone, J. M., & Hawley, J. F. 2000, ApJ, 530, 464

Foster, P. N. & Chevalier, R. A. 1993, ApJ, 416, 303

Fryxell, B., Olson, K., Ricker, P., Timmes, F. X., Zingale, M., Lamb, D. Q., MacNeice, P., Rosner, R., Truran, J. W., & Tufo, H. 2000, ApJS, 131, 273

Gammie, C. F. 1996, ApJ, 457, 355

Godunov, S. K. 1959, Math. Sbornik, 47, 271

Hillenbrand, L. A. 1997, AJ, 113, 1733

Hosking, J. G. & Whitworth, A. P. 2004a, MNRAS, 347, 1001

—. 2004b, MNRAS, 347, 994

Hunter, C. 1977, ApJ, 218, 834

Krasnopolsky, R. & Gammie, C. F. 2005, ApJ, 635, 1126

Krasnopolsky, R. & Königl, A. 2002, ApJ, 580, 987

Krumholz, M. R., Klein, R. I., & McKee, C. F. 2005, in IAU Symposium, Vol. 227, Massive Star Birth: A Crossroads of Astrophysics, ed. Cesaroni, R. and Felli, M. and Churchwell, E. and Walmsley, M. , 231–236

Kudoh, T., Basu, S., Ogata, Y., & Yabe, T. 2007, ArXiv e-prints, 706

Kunz, M. W. & Balbus, S. A. 2004, MNRAS, 348, 355

Larson, R. B. 1969, MNRAS, 145, 271

—. 1981, MNRAS, 194, 809

Lepp, S. & Shull, J. M. 1983, ApJ, 270, 578

Levy, E. H. & Sonett, C. P. 1978, in IAU Colloq. 52: Protostars and Planets, ed. T. Gehrels, 516–+

Li, P. S., McKee, C. F., & Klein, R. I. 2006, ApJ, 653, 1280

Li, Z.-Y. 1999, ApJ, 526, 806

Lynden-Bell, D. 2003, MNRAS, 341, 1360

Mac Low, M.-M. & Klessen, R. S. 2004, Reviews of Modern Physics, 76, 125

Mac Low, M.-M., Norman, M. L., Konigl, A., & Wardle, M. 1995, ApJ, 442, 726

Mac Low, M.-M. & Smith, M. D. 1997, ApJ, 491, 596

Machida, M. N., Inutsuka, S.-i., & Matsumoto, T. 2007, ArXiv e-prints, 705

Machida, M. N., Matsumoto, T., Hanawa, T., & Tomisaka, K. 2006, ApJ, 645, 1227

Matsumoto, T. & Hanawa, T. 2003, ApJ, 595, 913

Matsumura, S. & Pudritz, R. E. 2005, ApJ, 618, L137

Matsumura, S., Pudritz, R. E., & Thommes, E. W. 2007, ApJ, 660, 1609

McDaniel, E. W. & Mason, E. A. 1973, The mobility and diffusion of ions in gases (New York Wiley, 1973. 372 p.)

McKee, C. F. & Ostriker, E. C. 2007, ArXiv e-prints, 707

Mestel, L. & Spitzer, Jr., L. 1956, MNRAS, 116, 503

Mouschovias, T. C. & Paleologou, E. V. 1980, ApJ, 237, 877

—. 1986, ApJ, 308, 781

Nakano, T. 1979, PASJ, 31, 697

Nakano, T., Nishi, R., & Umebayashi, T. 2002, ApJ, 573, 199

Neufeld, D. A. & Kaufman, M. J. 1993, ApJ, 418, 263

Neufeld, D. A., Lepp, S., & Melnick, G. J. 1995, ApJS, 100, 132

O'Sullivan, S. & Downes, T. P. 2006, MNRAS, 366, 1329

Patel, K. & Pudritz, R. E. 1994, ApJ, 424, 688

Penston, M. V. 1969, MNRAS, 145, 457

Powell, K. G., Roe, P. L., Linde, T. J., Gombosi, T. I., & De Zeeuw, D. L. 1999, JCP, 154, 284

Price, D. J. & Bate, M. R. 2007, MNRAS, 377, 77

Safier, P. N., McKee, C. F., & Stahler, S. W. 1997, ApJ, 485, 660

Shu, F. H. 1977, ApJ, 214, 488

Smith, M. D. & Mac Low, M.-M. 1997, A&A, 326, 801

Spitzer, L. 1978, Physical processes in the interstellar medium (New York Wiley-Interscience, 1978. 333 p.)

Stone, J. M. & Gardiner, T. A. 2005, in American Institute of Physics Conference Series, Vol. 784, Magnetic Fields in the Universe: From Laboratory and Stars to Primordial Structures., ed. de Gouveia dal Pino, E. M. and Lugones, G. and Lazarian, A. , 16–26

Tassis, K. & Mouschovias, T. C. 2007a, ApJ, 660, 370

—. 2007b, ApJ, 660, 388

Tilley, D. A. & Pudritz, R. E. 2004, MNRAS, 353, 769

—. 2005, ArXiv Astrophysics e-prints

Tóth, G. 2000, JCP, 161, 605

Truelove, J. K., Klein, R. I., McKee, C. F., Holliman, II, J. H., Howell, L. H., & Greenough, J. A. 1997, ApJ, 489, L179+

Umebayashi, T. & Nakano, T. 1981, PASJ, 33, 617

Wardle, M. 1990, MNRAS, 246, 98

—. 1991a, MNRAS, 251, 119

—. 1991b, MNRAS, 250, 523

Yorke, H. W. & Sonnhalter, C. 2002, ApJ, 569, 846

Zweibel, E. G. 2002, ApJ, 567, 962